Experimental Characterisation of the

Low Temperature Properties of

$RE_{14}Ag_{51}$ Compounds

by

Sebastian Dressler

A Master's Thesis

Submitted in partial fulfilment of the requirements for the award of

Master of Philosophy of Loughborough University

September 28, 1999

Abstract

An experimental investigation of the low temperature properties of some $RE_{14}Ag_{51}$ compounds with RE= La, Gd, Tb, Dy, Ho, and Er is reported. The structure of the compounds has been characterised at room temperature using X-ray diffraction. All compounds crystallise within a single phase with the $Ag_{51}Gd_{14}$ structure type and space group P6/m

Magnetisation and specific heat measurements have been carried out All compounds reveal two magnetic phase transitions at low temperatures to an antiferromagnetically ordered state. A shift of these transition temperatures as a function of applied magnetic field is exhibited for all compounds. For $Tb_{14}Ag_{51}$ and $Dy_{14}Ag_{51}$ a triple point has been observed. With the exception of $Gd_{14}Ag_{51}$ magnetisation measurements at low temperatures indicate field induced changes of magnetic order. Phase diagrams have been constructed for all alloys In order to characterise lattice and electronic contributions the alloy $La_{14}Ag_{51}$ has been investigated as a non-magnetic reference compound.

An analysis of the systematics of the transition temperatures T_N yields a linear behaviour as a function of the de Gennes factor. Thus a scaling dependence of T_N (de Gennes scaling) has been identified for the $RE_{14}Ag_{51}$ series.

Contents

Chapter 1: Introduction

The investigation of the electronic and magnetic properties of materials is a well established branch of current solid state research within the field of condensed matter. The systematic investigation of particular classes of compounds has often proved an invaluable source of information. In recent years and due to their increased availability the properties and physics of the rare earth intermetallic compounds has attracted considerable attention.

In this thesis a systematic experimental study of some low temperature properties has been carried out on the rare earth series $RE_{14}Ag_{51}$ with the rare earth (RE) elements Gadolinium Gd, Terbium Tb, Dysprosium Dy, Holmium Ho, Erbium Er and Lanthanum La.

The rare earths comprise the elements from lanthanum to lutetium in the periodic table of elements. They are characterised by a partially filled $4f$-electron shell. Due to the small radius of the f-electron wavefunction the unfilled electron shell is well shielded from the local environment. Magnetic properties of intermetallic rare earth compounds are determined almost exclusively by the $4f$ electrons. The direct exchange interaction between two magnetic rare earth atoms is much to small to account for the magnetic properties due to the negligible overlap of $4f$-wavefunctions. It is the indirect exchange interaction via a polarisation of the conduction electrons which dominates the coupling between the $4f$-magnetic moments of neighbouring rare earth atoms. This indirect exchange interaction is known as the RKKY interaction and was first described by Ruderman and Kittel and further by Kasuya and Yosida. A variety of electronic and magnetic phenomena is observed experimentally. These properties have made rare earth systems a fruitful field for detailed study. Of particular importance are isostructural rare earth series, because it allows the investigation of systematics as a function of rare earth element. This arises due to the fact that the electronic

Chapter 2: Sample Preparation and Characterisation

Introduction

All $RE_{14}Ag_{51}$ alloys have been prepared in the Department of Physics at Loughborough University. A characterisation of the atomic structure and sample quality is necessary before starting a more detailed investigation. In this chapter the preparation and characterisation of the $RE_{14}Ag_{51}$ samples is illustrated. For the characterisation of the atomic structure X-ray diffraction measurements have been carried out using the Debye-Scherrer powder method. All alloys were found to crystallise in the $Ag_{51}Gd_{14}$ structure. For these measurements a calibration of the X-ray diffractometer was carried out by using pure Nickel powder. A value of the ratio between the intensities of the two $Cu-K_\alpha$ components to the radiation is obtained.

Materials

For the rare earth compounds $RE_{14}Ag_{51}$ the starting materials were Silver (Ag), Lanthanum (La), Gadolinium (Gd), Terbium (Tb), Dysprosium (Dy), Holmium (Ho) and Erbium (Er). All these materials had a high chemical purity of 3N. All materials were bought from Johnsen Matthey, Materials Technology U. K., Ochard Road, Royston, Herts., England and were stored in an evacuated glass container and mechanically cleaned before preparation

Preparation

The appropriate amounts of pure elements were repeatedly arc-melted in a furnace under a reduced atmosphere of argon (pressure ~0.3 bar). The argon-arc furnace was built in the Department and consists of a small chamber, a water cooled tungsten-electrode and a copper hearth in which cigar shaped troughs

3

were placed. Titanium as a getter material was used to remove any residual oxygen. Ingots weighting 12g were prepared with this arc-melting technique. To ensure homogeneity in the alloy the ingot was turned over and remelted several times. Afterwards, part of each ingot (2g-3g) was spark eroded and powdered with a hardened steel pestle and a mortar. The size of the grains of this powder was smaller than 250 µm.

The method of arc-melting by a hot electron arc is accompanied by very high temperature gradients across the ingot. This results in a small weight loss during the preparation process. All samples (powder and ingot) were annealed rapped in tantalum foil in an evacuated quartz tube and slowly cooled. Because of different melting points of the alloys the heat treatment was carried out at different temperatures. The important values of the treatment for all samples is listed in table 2.1

Sample	Weight lost after melting	Heating-Temperature	Heating-time	Cooling-range
$La_{14}Ag_{51}$	1 6 %	700 C°	60 hr	60 C°/hr
$Gd_{14}Ag_{51}$	0 05 %	900 C°	20 hr	60 C°/hr.
$Tb_{14}Ag_{51}$	0 11 %	900 C°	20 hr	60 C°/hr
$Dy_{14}Ag_{51}$	0 4 %	900 C°	60 hr	30 C°/hr
$Ho_{14}Ag_{51}$	0 41 %	850 C°	20 hr	60 C°/hr.
$Er_{14}Ag_{51}$	0 09 %	800 C°	60 hr.	30 C°/hr

Table 2.1. Details of the heat-treatment of the various $RE_{14}Ag_{51}$ compounds.

With the exception of the $La_{14}Ag_{51}$-compound the weight loss after heat-treatment was found to be within ~0.5 % on average.

For the preparation of samples with the appropriate shape the ingot was cut under oil with a spark eroder. For the specific heat measurement a sample of 1g – 1.5g was prepared with one polished surface. From the remaining material a small piece for the measurement of magnetic properties had been selected.

Finally, all prepared samples were cleaned with acetone and stored in small glass tubes.

Crystallographic structure

All samples crystalline in the hexagonal structure with the $Ag_{51}Gd_{14}$ type and space group P6/m [1], [2], [3], [4].The atomic structure is shown in the figure 2.1.

Steeb et al. [5] investigated this structure type. Their samples of composition Ag_3RE were found to crystalline in the structure type Ag_3Pu and the space group $P6_3/m$. Kiessler et al. [6] investigated the silver-gadolinium phase diagram and the Ag_3Pu structure type was identified. For the first time McMasters et al. [1] [2] discovered the correct structure of $Ag_{51}Gd_{14}$ in the silver rich rare earth-silver series. Later Bailey and Kline [3] investigated this series and obtained reliable data for the hexagonal $Ag_{51}Gd_{14}$ intermetallic compound. For the $Ag_{51}Gd_{14}$ structure type and space group P6/m atomic positions are shown in the table 2.2.
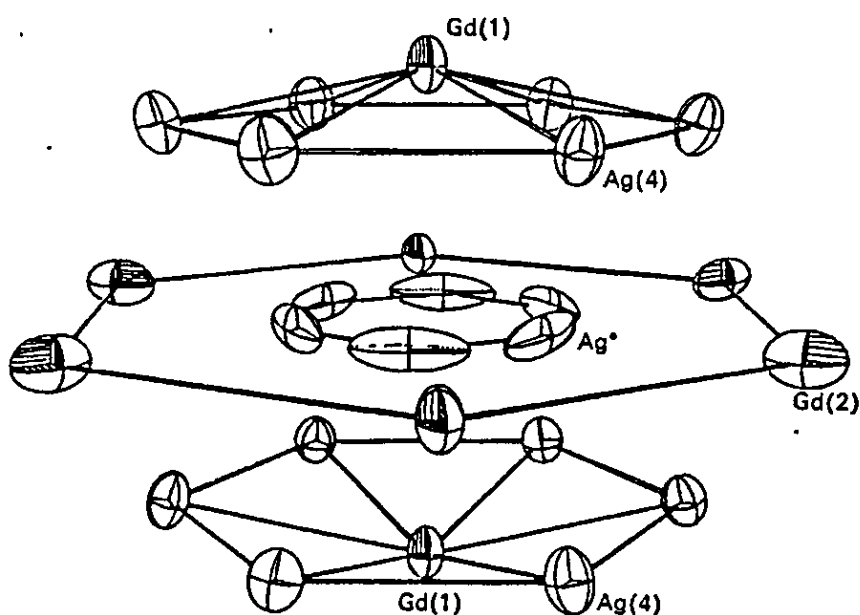
Figure 2 1. Atomic structure of $Ag_{51}Gd_{14}$ type reported (After Bailey et al. [3])

Atom	Wyckoff notation	Site Symmetry	x	y	z	Site Occupancy
$Ag^{(1)}$	2(c)	$\bar{6}$	0.3333	0 6667	0	1 00
$Ag^{(2)}$	4(h)	3	0 3333	0 6667	0 2987	1.00
$Ag^{(3)}$	6(k)	m	0 2383	0 0589	0 5000	0 47
$Ag^{(4)}$	12(l)	m	0 2662	0 1918	0 2370	1 00
$Ag^{(5)}$	12(l)	1	0.1155	0 4944	0 1526	1 00
$Ag^{(6)}$	12(l)	1	0 04390	0 1049	0 3305	1 00
$Ag^{(7)}$	6(j)	1	0 1131	0 1324	0	1 00
$Gd^{(1)}$	2(e)	6	0	0	0 3060	1 00
$Gd^{(2)}$	6(j)	m	0 3898	0 1138	0	1 00
$Gd^{(3)}$	6(k)	m	0 1394	0 4680	0 5000	1 00

Table 2 2 Crystallographic parameters for the $Ag_{51}Gd_{14}$ structure type and space group P6/m from Bailey et al [3]

X-ray diffraction (XRD)

X-ray diffraction was used to obtain the crystallographic structure of the samples In order to investigate the atomic structure of lattice with a lattice parameter of the order of Angstrom in a diffraction experiment, one needs to use radiation with a wavelength of the same order of magnitude. X-ray radiation provides such wavelengths.

For this investigation the Debye-Scherrer powder method was used at room temperature. The equipment was a X-ray generator PW 1130/90/96 (Philips) with a proportional detector probe PW 1965/20/30. The geometry of the diffractometer is schematically shown in figure 2.2. The anode in the X-ray generator consisted of copper (Cu). Therefore the characteristic X-ray radiation was the $K_{\alpha1\alpha2}$ doublet with the wavelengths $K_{\alpha1}$ = 1.540541 Å and $K_{\alpha2}$ = 1.54433 Å. To obtain monochromatic radiation, a nickel filter was used to filter one of these K_{β}-contribution.

With such a monochromatic radiation the Debye-Scherrer powder method can be used to investigate the crystallographic structure of an atomic lattice. A schematic diagram of diffraction of X-rays by a crystal is shown in figure 2.3. When X-rays of a wavelength λ are directed onto a crystal at an angle θ, diffraction will occur due to parallel atomic planes of separation d. The amplitude of the diffracted X-ray beam will be maximal when the path difference between rays reflected from successive planes is equal to a whole number of wavelengths ($n\lambda$). The relation which applies to this condition is called the Bragg law

$$n\lambda = 2d \sin\theta \,.$$

For the evaluation of the X-ray diffraction pattern the software program FullProf (version 3.5 Dez. 97-LIB-GRC written by Juan Rodriguez-Carvajal [7]) was used. This program refines a calculated diffraction spectrum and fits it to the observed spectrum. The refined parameters are:

- zero point (2θ off-set)
- overall scale factor
- lattice parameters
- atomic positions
- occupation numbers
- 3 peak shape parameters half width parameters of peak shape
- isotropic temperature factor

A statistical χ^2-test was applied to the fit, defined by

$$\chi^2 = \sum_{obs} \frac{(F_{obs} - F_{calc})^2}{(\sigma F_{obs})^2} \Big/ (N_{obs} - N_{par})$$

where N_{obs} is the number of observations and N_{par} is the number of parameters.
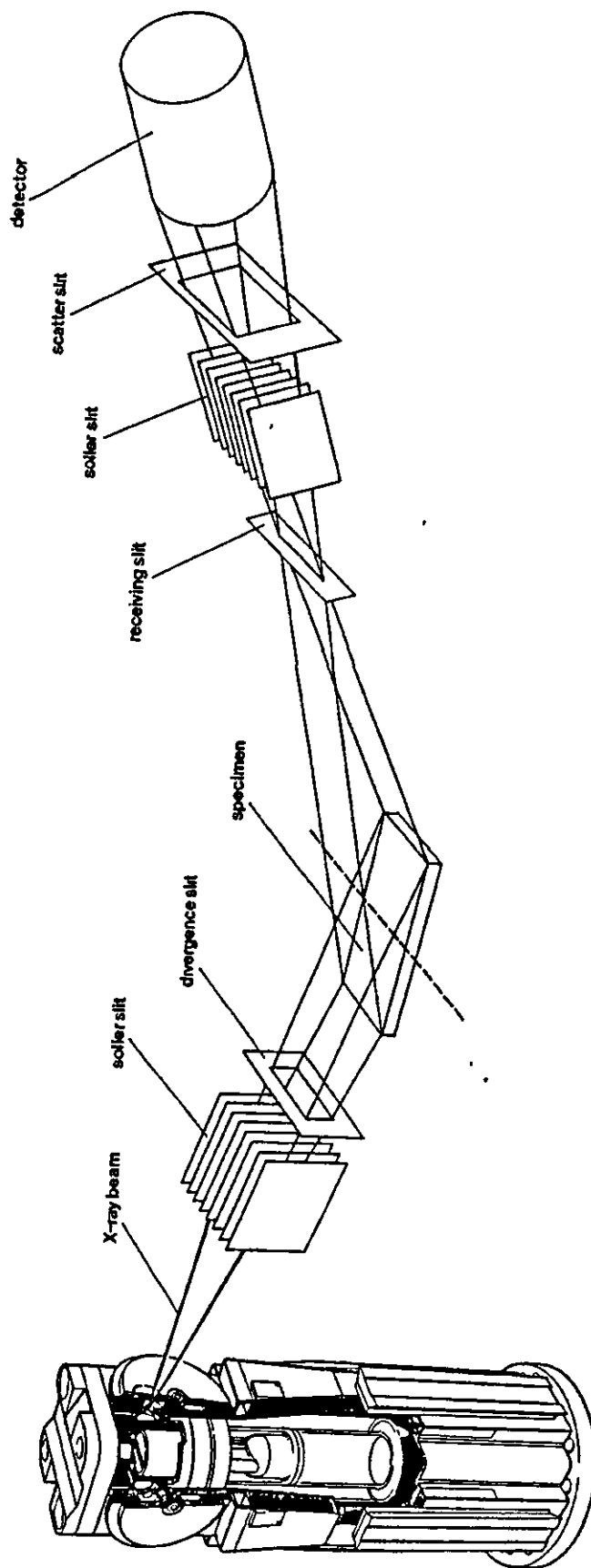
Figure 2 2   Illustration of the geometry of the diffractometer

8

Figure 2.2: Illustration of the geometry of the diffractometer

X-ray beam

soller slit

divergence slit

specimen

receiving slit

soller slit

scatter slit
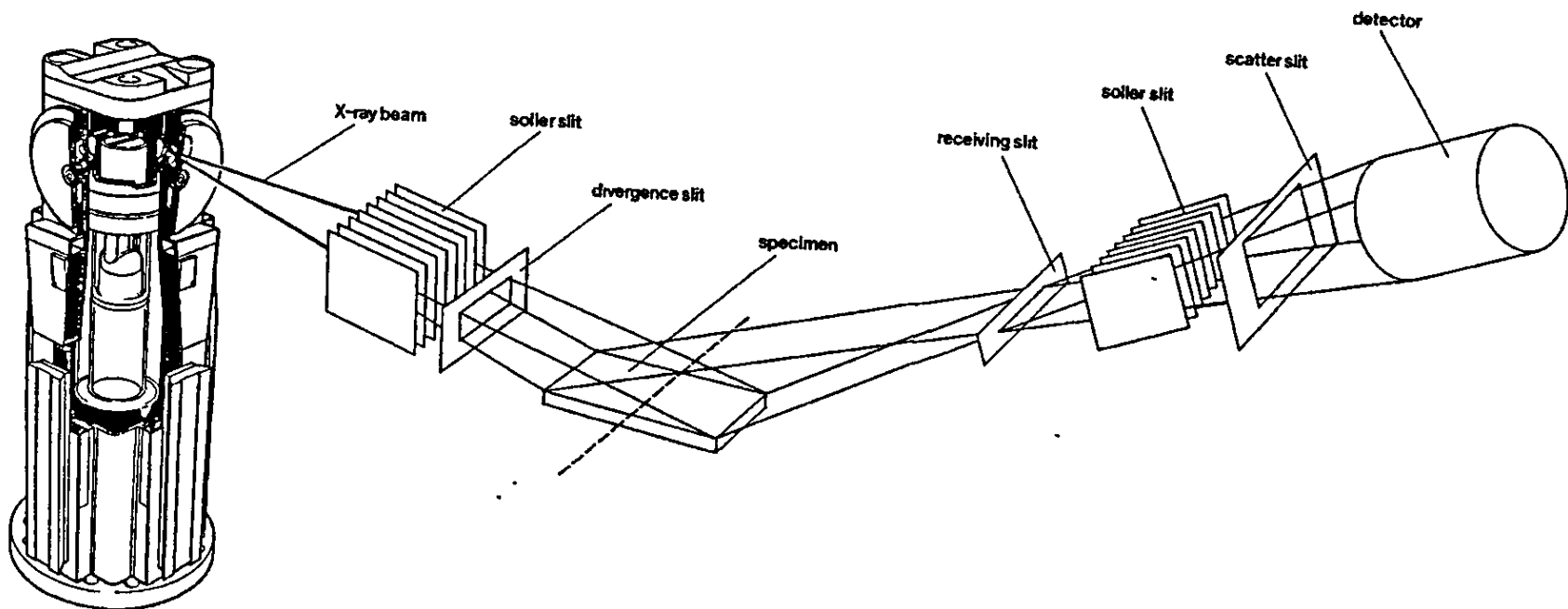
detector
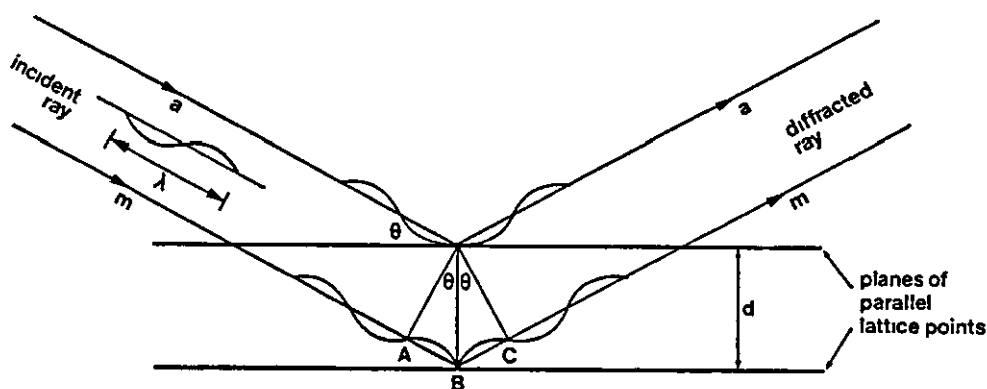
Figure 2 3· Illustration of Bragg's law

Calibration of the diffractometer

As described above the characteristic radiation $K_{\alpha 1} = 1.540541$ Å and $K_{\alpha 2} = 1.54433$ Å appear for a X-ray generator with a copper anode If two different wavelengths are directed onto a crystal, then there appear two diffraction patterns of the same structure which a shifted by a known amount. The shift can be determined with the aid of Bragg's law.

With the program FullProf it is possible to evaluate a diffraction spectrum with two shifted patterns. It is necessary to know both wavelengths and the ratio of their intensities. To determine the intensity ratio a measurement was carried out using pure nickel powder. The X-ray-diffraction pattern is shown in the figure 2.4.

Two patterns each with three peaks are shown, which belong to the Bragg-reflections of the three h, k, l planes (111), (200), (220) respectively and to the two different wavelengths. (h, k, l are the Miller indices.) With the program FullProf a pattern was refined using one wavelength and two different nickel lattice parameters. The measured and refined patterns and their difference are plotted in graph 2.5. For each of the nickel-patterns the program calculated the

9

following refined parameters: zero point off set, overall scale factor lattice parameters, peak shape parameters and overall isotropic temperature factor.

The overall scale factor is a parameter which normalises to the value of the intensity, thus the ratio of the overall scale parameter yields the intensity ratio of the two different nickel-lattices. This result is analogous to one nickel-lattice but two different wavelengths. This is the case for the actual measurement. Therefore, the ratio between both K_α-radiation is determinated as

$$I(K_{\alpha 1}) / I(K_{\alpha 2}) = 2.64 \pm 0.09$$

To verify this result the ratio of the cell parameters of both nickel-patterns was compared with the ratio of the different wavelengths of the $K_{\alpha 1}$-, and $K_{\alpha 2}$-radiation. The difference was founded to be just 1% which shows that such a comparison is possible.
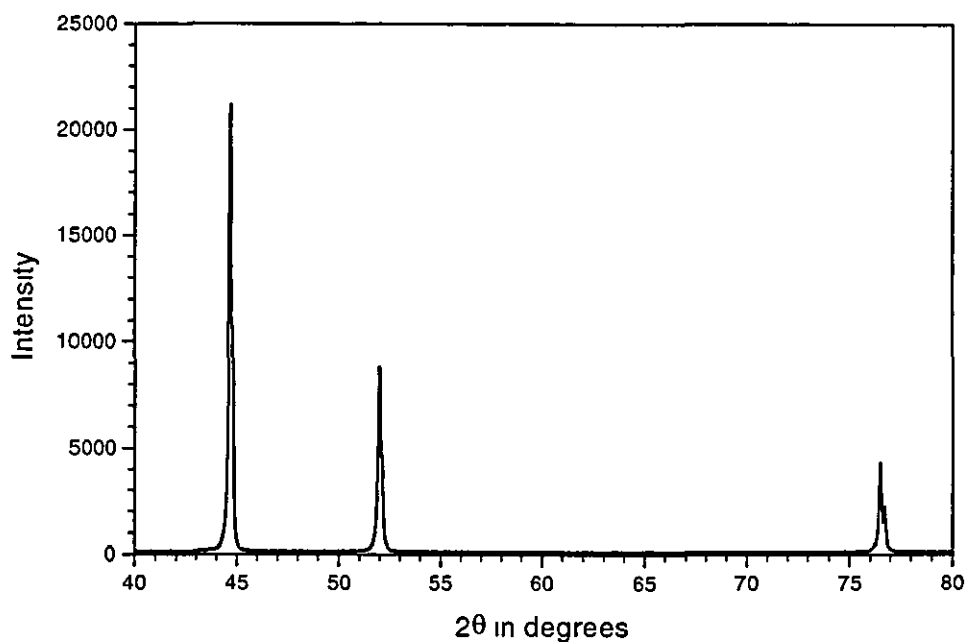
Figure 2.4· X-ray diffraction pattern of Nickel powder.

10
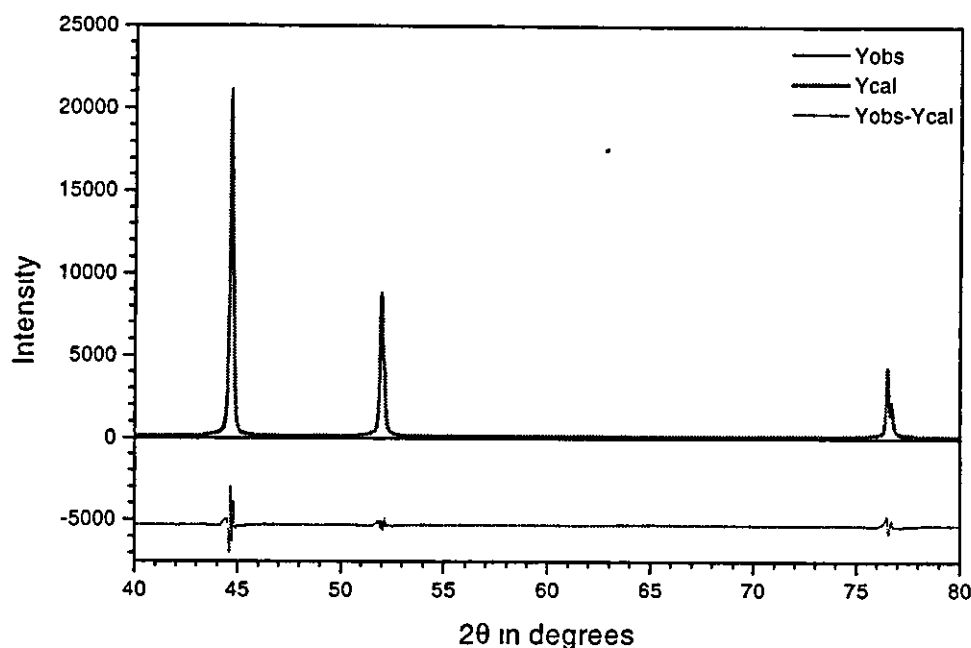
Figure 2 5. Experimental and refined X-ray diffraction pattern of Nickel powder

Characterisation

All powdered compounds were measured over the angular range $10° < 2\theta < 85°$ in steps of $0.05°$ and a time scale of 20 sec per step. The X-ray generator was operated with a current of 20 mA and a voltage of 40 kV. The diffraction pattern was evaluated with the software program FullProf as described above.

In the following figures 2.6, 2.7, 2.8, 2.9, 2.10, 2.11 are shown the observed X-ray diffraction spectra (Yobs), the calculated spectra (Ycal) and the difference between both spectra (Yobs-Ycal) for each compound.
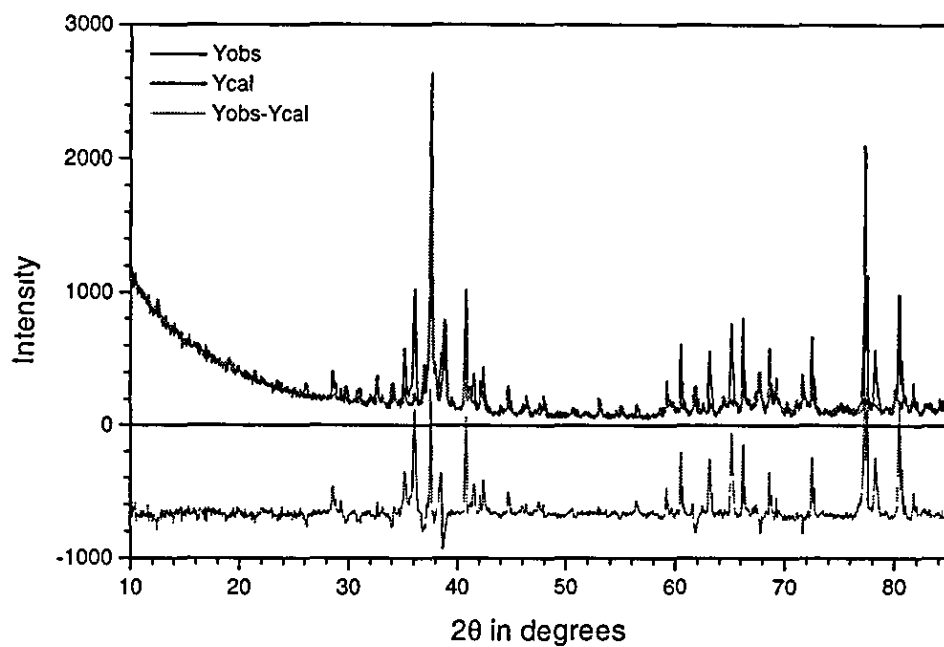
Figure 2 6   X-ray diffraction pattern of Gd$_{14}$Ag$_{51}$
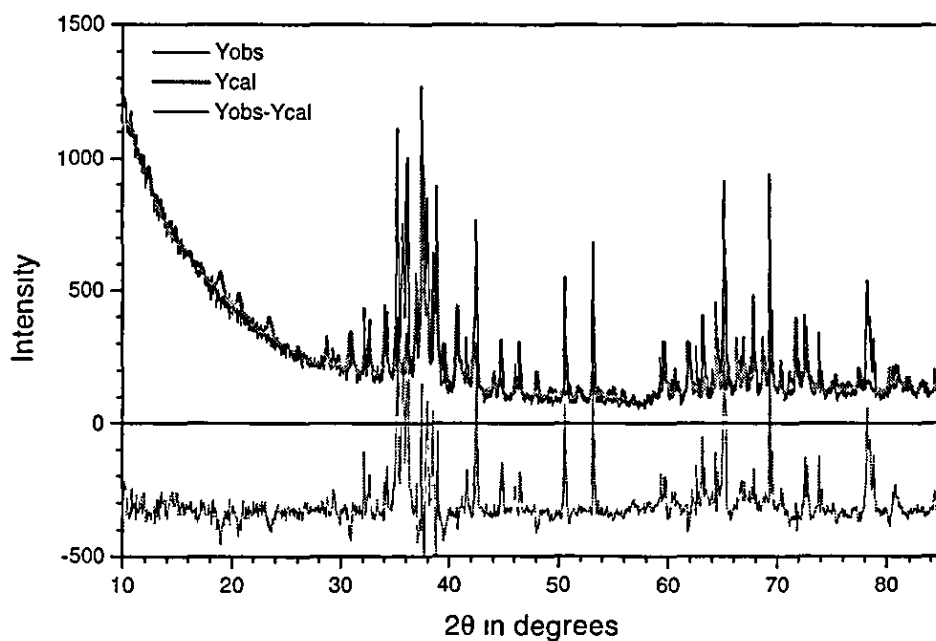
Figure 2 7· X-ray diffraction pattern of Tb$_{14}$Ag$_{51}$

12
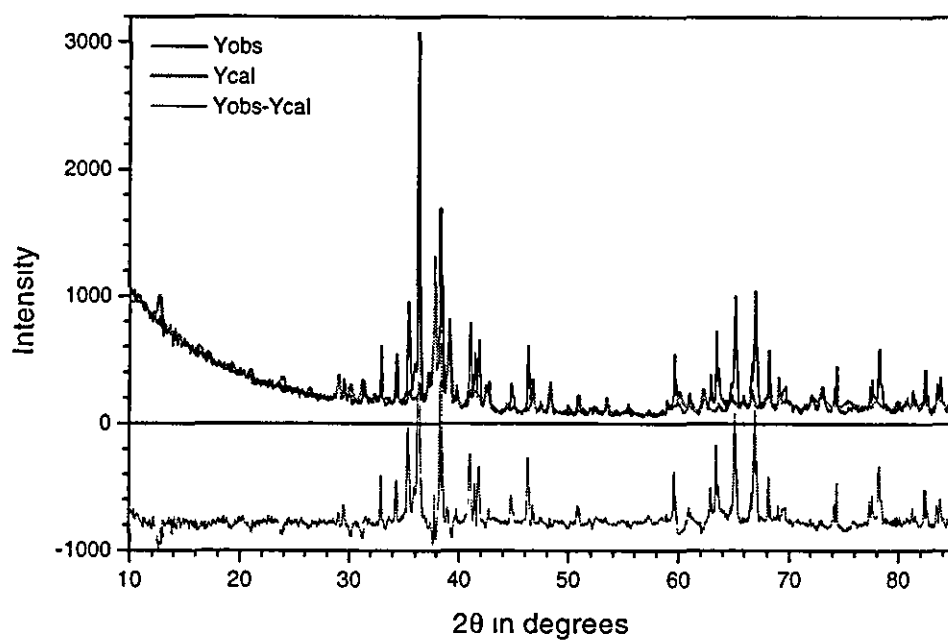
Figure 2 8 X-ray diffraction pattern of $Dy_{14}Ag_{51}$
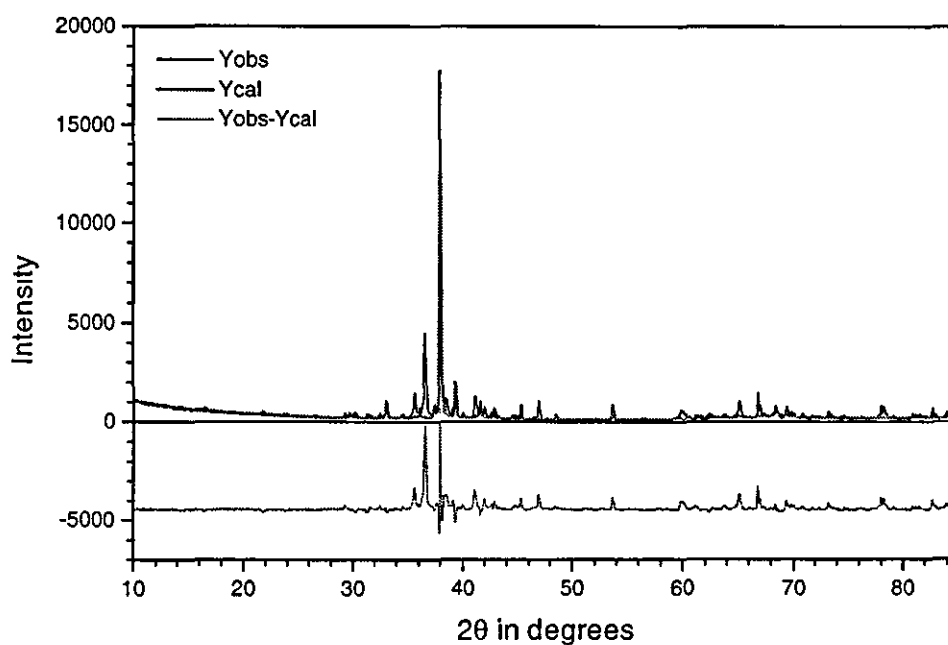
Figure 2 9: X-ray diffraction pattern of $Ho_{14}Ag_{51}$
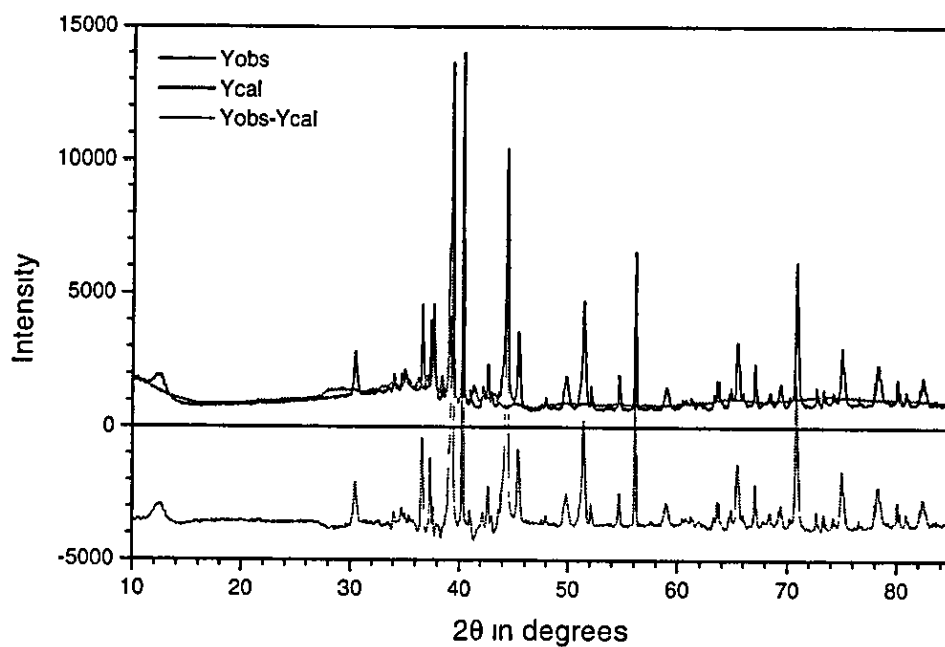
Figure 2 10· X-ray diffraction pattern of Er₁₄Ag₅₁
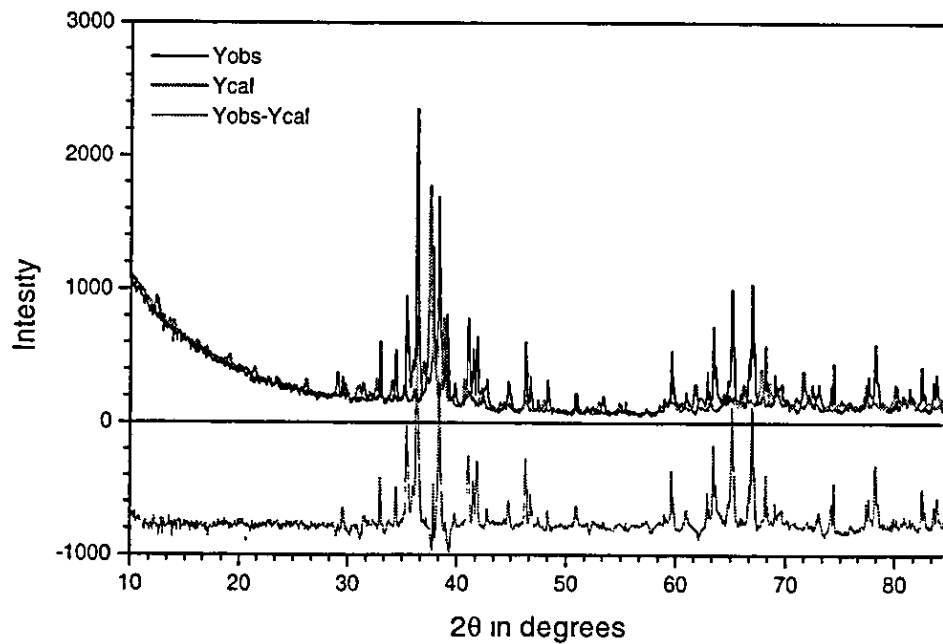
Figure 2.11: X-ray diffraction pattern of La₁₄Ag₅₁

14

Looking at the graphs it is possible to recognise that the structure of the alloys corresponds to the atomic structure type of $Ag_{51}Gd_{14}$ and the hexagonal space group P6/m, because the peaks of the calculated and refined spectrum fit on the same positions as the peaks of the obtained diffraction spectrum. Furthermore, the lattice parameters obtained are not so far off the lattice parameters that are given by McMaster et. al. [2]. However, the intensities of the calculated and observed peaks do not correspond to each other. The intensities of the observed peaks are greater than the calculated ones. Furthermore, the refined values of occupation numbers and atom positions differ from the values given in the literature [1], [2], [3], [4]. This discrepancy could be attributed to the fact that the powder grains were not sufficiently small and that a complete random orientation of all crystallites was probably not guaranted The program FullProf [7] allows to refine more than one phase. This was already used for the determination of the intensity ratio of the two K_{α}-contributions To confirm that the alloys are single phase and only consist of the $Ag_{51}Gd_{14}$ structure the structure types of adjacent phases in the phase diagram [6] were also refined such as Ag (Cu, Fm3m) and Ag_2RE (MoSi₂, I4/mmm) [2], [4]. This refinement did not change the calculated pattern of the $Ag_{51}RE_{14}$ phase The overall scale factors of the impurity phases were found to be converge to values close to zero. This verified that no other neighbouring RE-Ag phases are contained in these samples.

The refined and calculated parameters, lattice parameters and χ^2-values, are shown in table 2.3 and are compared to values found in the literature [1]. In table 2 4 the refined atom positions and occupation numbers are shown.

alloy	lattice parameters (Å) by McMasters et. al [1]		lattice parameters (Å) observed parameters		χ^2
	a_0	c_0	a_0	c_0	
$Ag_{51}La_{14}$	12 955 ± 0 005	9.525 ± 0 007	12 903 ± 0 003	9 601 ± 0 004	46 5
$Ag_{51}Gd_{14}$	12 681 ± 0 003	9 289 ± 0 004	12 669 ± 0 003	9 324 ± 0 004	23 7
$Ag_{51}Tb_{14}$	12 65 ± 0 005	9 28 ± 0 003	12 631 ± 0 003	9 296 ± 0 004	18.0
$Ag_{51}Dy_{14}$	12 635 ± 0 003	9 271 ± 0 002	12 614 ± 0 003	9 269 ± 0 004	30 1
$Ag_{51}Ho_{14}$	12 609 ± 0 006	9 257 ± 0 002	12.591 ± 0 003	9 260 ± 0 004	47 9
$Ag_{51}Er_{14}$	12 596 ± 0 002	9 236 ± 0 001	12 41 ± 0 01	9 30 ± 0 01	112

Table 2 4 *Lattice parameters*

15

Atom	Atom Pos	Ag$_{51}$Gd$_{14}$#	Ag$_{51}$La$_{14}$*	Ag$_{51}$Gd$_{14}$	Ag$_{51}$Tb$_{14}$	Ag$_{51}$Dy$_{14}$*	Ag$_{51}$Ho$_{14}$*	Ag$_{51}$Er$_{14}$*
Ag$^{(1)}$	x	0 3333	0 3333	0 3333	0 3333	0 3333	0 3333	0 3333
	y	0 6667	0 6667	0 6667	0 6667	0 6667	0 6667	0 6667
	z	0 0000	0 0000	0 0000	0 0000	0 0000	0 0000	0 0000
	occ.	2 0000	2 0000	4.9782	3 7821	2 0000	2 0000	2.0000
Ag$^{(2)}$	x	0 3333	0 3333	0 3333	0.3333	0 3333	0 3333	0 3333
	y	0 6667	0 6667	0 6667	0 6667	0 6667	0 6667	0 6667
	z	0 2370	0.2546	0.3062	0 3170	0 2370	0 1020	0 2468
	occ	4 0000	4 0000	4 0869	2 0429	4 0000	4 0000	4 0000
Ag$^{(3)}$	x	0.1131	0.1098	0 1040	0 1100	0.1131	0 2225	0.1168
	y	0 1324	0 1321	0 1315	0.1413	0 1324	0 0476	0 1127
	z	0 0000	0 0000	0 0000	0 0000	0 0000	0 0000	0 0000
	occ.	2 8200	2 8200	5 2432	8 8536	2 8200	2 8200	2.8200
Ag$^{(4)}$	x	0 2383	0.2235	0 2240	0 2152	0 2383	0 2285	0 2248
	y	0 0589	0 0524	0 0505	0 0468	0 0589	0 0566	0 0542
	z	0 5000	0 5000	0 5000	0 5000	0 5000	0 5000	0 5000
	occ	6 0000	6 0000	12 5505	12 0208	6 0000	6 0000	6 0000
Ag$^{(5)}$	x	0 2662	0 2662	0 2662	0 2662	0 2662	0 2662	0 2662
	y	0 1918	0 1918	0 1918	0 1918	0 1918	0.1918	0 1918
	z	0 2370	0 2370	0 2370	0 2370	0 2370	0 2370	0 2370
	occ.	12 0000	12 000	12.0994	12.7609	12 0000	12 0000	12 000
Ag$^{(6)}$	x	0 1155	0.1155	0 1155	0 1155	0 1155	0.1155	0 1155
	y	0 4944	0 4944	0 4944	0 4944	0.4944	0 4944	0 4944
	z	0 1526	0 1526	0 1526	0 1526	0 1526	0 1526	0 1526
	occ	12 0000	12 0000	11.9480	10.7059	12 0000	12.0000	12 0000
Ag$^{(7)}$	x	0 4390	0 4390	0 4390	0 4390	0 4390	0 4390	0 4390
	y	0 1049	0.1049	0 1049	0.1049	0 1049	0 1049	0 1049
	z	0.3305	0 3305	0 3305	0 3305	0.3305	0 3305	0 3305
	occ	12 0000	12 0000	11 2596	10 2672	12 0000	12 0000	12 0000
Gd$^{(1)}$	x	0 0000	0 0000	0 0000	0 0000	0 0000	0 0000	0 0000
	y	0 0000	0 0000	0 0000	0 0000	0 0000	0 0000	0 0000
	z	0 3060	0 3201	0 3199	0 3163	0.3060	0 3366	0 3085
	occ.	2 0000	2 0000	2 1533	2 9814	2.0000	2 0000	2 0000
Gd$^{(2)}$	x	0 3898	0 3898	0 3898	0 3898	0.3898	0 3898	0 3898
	y	0 1138	0 1138	0 1138	0 1138	0 1138	0 1138	0 1138
	z	0 0000	0 0000	0 0000	0 0000	0 0000	0 0000	0 0000
	occ	6 0000	6 0000	9 8100	11 6847	6 0000	6 0000	6.0000
Gd$^{(3)}$	x	0 1394	0 1394	0 1394	0 1394	0 1394	0 1394	0.1394
	y	0 4680	0 4680	0 4680	0 4680	0 4680	0 4680	0 4680
	z	0 5000	0 5000	0 5000	0 5000	0 5000	0 5000	0 5000
	occ.	6 0000	6 0000	6 1705	2.8046	6 0000	6 0000	6.0000

Table 2 5· Atom positions and occupation numbers
#In the first column the literature value are shown [1]
×For of these samples the occupation numbers have not been refined

In conclusion it can be stated that all samples are single phase and crystallise in the $Ag_{51}Gd_{14}$ structure type with space group P6/m. A schematic picture of the atom positions and the lattice sites is shown in figure 2.12. The rare earth atoms (RE) are located on three crystallographically distinct sites 2(e), 6(j), 6(k). The $RE^{(2)}$ {6(j)} and $RE^{(3)}$ {6(k)} atoms are located in two planes at z = 0 and z = 1/2. The $RE^{(1)}$ atoms are located along the c-axis. The silver atoms (Ag) fill the spaces between the RE layers. The two $RE^{(1)}$ atoms are located on the 2(e) lattice sites of the unit cell and form a pair. They are shielded from other RE atoms in the layers 6(j) and 6(k). This affects on the magnetic behaviour favouring magnetic order only for the 12 rare earth atoms which are located within the hexagonal planes at z = 0 and z = 1/2 in the unit cell. The same argument applies to the macroscopic magnetisation if a external magnetic field is applied. The fraction of the atoms carrying a magnetic moment is believed to be limited to only 12 rare earth atoms per unit cell [8]. This again will affect the magnetic entropy ΔS and its contribution to the specific heat. This will be discussed more fully in chapter 4.
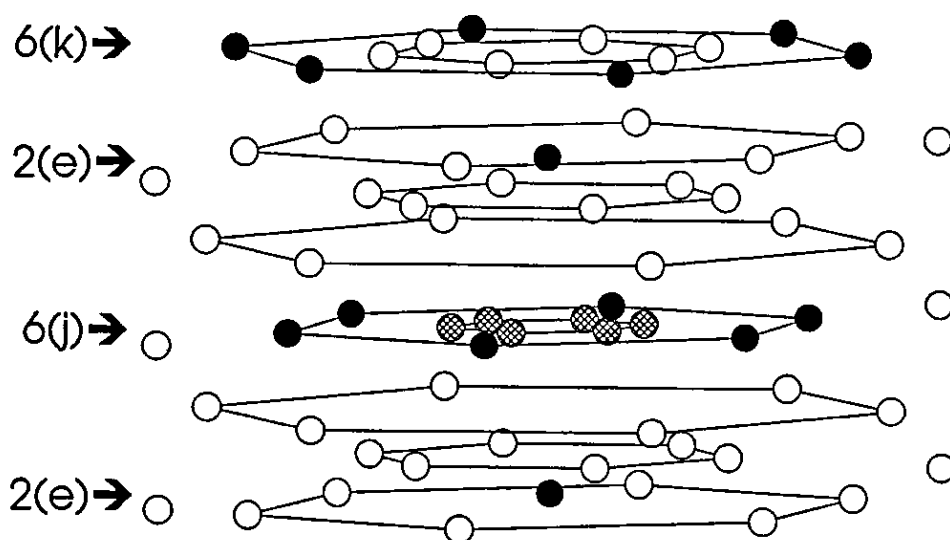

Figure 2 12· Crystallographic structure and atom positions (After Brown et al. [8]) The filled circles represent RE atoms and unfilled circles Ag atoms. The cross-hatched circles are Ag atoms sites but only half of the sites occupied

Chapter 3: Magnetic Properties of $RE_{14}Ag_{51}$

Introduction

The electronic and magnetic properties of rare earth alloys continue to provide a source of interesting phenomena for detailed study. At low temperatures it is observed that many materials possess a finite magnetisation in the absence of an applied field. This spontaneous magnetisation is due to the alignment of permanent magnetic dipole moments and indicates that each dipole is aware of the direction in which other dipoles are pointing. This awareness results from the interaction between the moments. The transition to a state for which the dipoles are aligned represents an increase in the degree of order within the solid and thus a decrease of entropy. The simplest type of magnetic order is ferromagnetism for which all moments are aligned parallel to one another and contribute equally to the spontaneous magnetisation. The ordering in antiferromagnets is such that half the dipoles are aligned in one direction and the other half in the opposite direction. For ferrimagnets there are oppositely directed moments of different magnitude such that a net macroscopic magnetic moment results.

In this chapter the experimental results are presented of the investigation of the $RE_{14}Ag_{51}$ alloy series (RE = Gd, Tb, Dy, Ho, Er and La) The magnetisation of these compounds has been measured as a function of temperature and magnetic field. The measurements have been carried out in the Department of Physics at Loughborough University using the SQUID system

In section 3 1 a more detailed description is given of the theory of magnetism. In order to be consistent with the definition of the formulae and units the description and symbols are based on the notation as given in the book by J Crangle. The SI-unit system is adopted throughout the thesis

In section 3.2 the used equipment, the SQUID system, is briefly described

The results of the magnetisation measurements are described in section 3.3. A final discussion of these results is presented in chapter 5 together with the results obtained by specific heat measurements.

3.1 Theory of Magnetism

Magnetic Dipoles

The concept of localised moment magnetism can be understood in simple terms as the motion of electric charges (electrons moving around a core on circular paths). According to Ampère's law the motion of these charges will cause a magnetic moment to occur. This magnetic moment is given by the vector product of the loop area of the orbit and the current around this loop. For an orbital with only one electron of charge e and mass m_e the dipole moment is

$$\mu = -\frac{1}{2}e\mathbf{r}\times\mathbf{v} = -e\left(\frac{\omega}{2\pi}\right)\pi r^2 = -\frac{1}{2}e\omega r^2, \qquad [3.1]$$

where r is the radius of the loop and ω is the angular velocity of the electron. The angular momentum is defined as

$$\mathbf{J} = m_e\,\mathbf{r}\times\mathbf{v} = m_e\,\omega r^2 \qquad [3.2]$$

and therefore,

$$\mu = -\left(\frac{e}{2m_e}\right)\mathbf{J} \qquad [3.3]$$

Because of the quantised nature of the motion of electrons the angular momentum is also quantised in units of $\hbar = h/2\pi$, where h is Planck's constant. In the lowest state the magnetic moment has the value

$$\mu_B = \frac{eh}{4\pi m_e} = \frac{e\hbar}{2m_e} = 9.2732\times10^{-24}\ JT^{-1} \qquad [3.4]$$

the Bohr magneton. In general the magnetic moment which is associated with the orbital motion must be a multiple of the Bohr magneton.

In addition each electron has an intrinsic angular momentum, a spin, which contributes to the total angular momentum. The spin of the electron is related to a spin quantum number $s = \pm 1/2$. Furthermore, a magnetic moment for this "spinning motion" can be defined as

$$\mu_s = g\,s\,\mu_B \qquad\qquad\qquad [3.5]$$

where g is the spectroscopic splitting factor (or just the g-factor) which has a value of $g = 2.0023$ for a free electron.

Magnetic moment of an atom

For an atom with more than one electron the total angular momentum is given by vector addition of the orbital and spin angular momenta. For this the following types of interactions have to be considered:

1. The spin-orbital interaction, either for the interaction between the orbital angular momentum of one electron and its own spin or for the same interaction between different electrons.
2. The orbit-orbit interaction between different electrons
3 The spin-spin interaction between different electrons

From experiments it is found that in most cases the spin-orbit interaction is very small in comparison to the orbit-orbit and spin-spin interactions. Therefore, it can be assumed that the vector combination proceeds in the manner described by Russell and Saunders (1925) In this coupling scheme the individual orbital and spin quantum numbers combine to give a total angular momentum. This implies that all spins form a resultant vector $\mathbf{S}$ and all orbital angular momenta form a resultant vector $\mathbf{L}$. The total angular momentum $\mathbf{J}$ is then given by

$$\mathbf{J} = \mathbf{L} + \mathbf{S} \qquad\qquad\qquad [3.6]$$

and the corresponding quantum number J can take the values

$$J = |L - S|, |L - S + 1|, ... |L + S|.$$ [3.7]

The projection M_J of J onto the quantisation axis has the values

$$M_J = -J, -J + 1, ..., J - 1, J,$$ [3.8]

which can only be integer or half integer. So for each value of J there is a multiplet with $2J + 1$ levels each of which corresponds to a value of M_J

In order to obtain the values of L and S of an atom it is assumed that the electrons (fermions) fill the quantised energy levels respecting both the Pauli-exclusion principle and Hund's rules.

Pauli-exclusion principle·

> Two fermions cannot be in the same state, where each state is defined by a complete set of quantum numbers n, l, m_l, m_s.

Hund's rules:

> For a free atom the electron shells are filled such that
> 1. the value of the total spin S for each sub-shell is maximal.
> 2. the value of the orbital momentum L is a maximum consistent with the value of S.
> 3. the value of the total angular momentum J is $J = |L + S|$ for a shell (corresponding to the quantum number n) which is more then half filled and $J = |L - S|$ for a shell which is less than half full.

For a completely filled sub-shell the values of L, S and J are zero. Therefore, it can be seen that a magnetic moment only occurs when a shell is not completely filled.

As described above for each possible value of J there occurs a multiplet of energy states with $2J + 1$ levels each corresponding to one value of M_J For a

22

free atom and zero external magnetic field all levels in a multiplet have the same energy. If a magnetic field is applied, then these levels will split into separate energy levels. (Crystal fields in solids are also able to lift degeneracies.)

For given values of the quantum numbers L, S and J the angular momentum vectors $\mathbf{L}$, $\mathbf{S}$ and $\mathbf{J}$ can be written for the general case as

$$\mathbf{L}^2 = \left(\frac{h}{2\pi}\right)^2 L(L+1), \qquad\qquad\qquad [3.9]$$

$$\mathbf{S}^2 = \left(\frac{h}{2\pi}\right)^2 S(S+1), \qquad\qquad\qquad [3.10]$$

$$\mathbf{J}^2 = \left(\frac{h}{2\pi}\right)^2 J(J+1). \qquad\qquad\qquad [3.11]$$

So it is possible to define the corresponding vectors of magnetic moments:

$$\mu_L = \mu_B \sqrt{L(L+1)}, \qquad\qquad\qquad [3.12]$$

$$\mu_S = 2\mu_B \sqrt{S(S+1)}, \qquad\qquad\qquad [3.13]$$

$$\mu_J = g\mu_B \sqrt{J(J+1)}, \qquad\qquad\qquad [3.14]$$

where g is the Landé factor

$$g = 1 + \frac{J(J+1)+S(S+1)-L(L+1)}{2J(J+1)}. \qquad\qquad\qquad [3.15]$$

Thus the magnetic moment of a single atom is defined. In the absence of an external magnetic field all atoms have the same magnetic moment with the same energy. In an applied field the energy levels of a multiplet are lifted and the energy

$$E_{mag} = -\mu_J \mathbf{B}_0 = -g\mu_B M_J B_0 \qquad\qquad\qquad [3.16]$$

depends on the value of M_J.

23

Magnetic moment of a solid

The total magnetic moment of a solid can be obtained by addition of all atomic moments But the population of the electrons in each multiplet has to be known. With the assumption that the energy differences between multiplets are very large compared to the energy differences within a multiplet the population probability of a sub-level is given by

$$P(M_J) = \frac{\exp\left[-\beta E_{mag}(M_J)\right]}{\sum \exp\left[-\beta E_{mag}(M_J)\right]},$$ [3.17]

where $\beta = (k_B T)^{-1}$ and $k_B = 1.38062 \ 10^{-23} \ J \ K^{-1}$ the Boltzmann constant.

For a single magnetic moment in an applied magnetic field the total magnetic moment in the direction of the magnetic field is then

$$\langle \mu_{J\uparrow} \rangle = \sum_{M_J} g \, \mu_B \, M_J \, P(M_J)$$ [3.18]

or

$$\langle \mu_{J\uparrow} \rangle = g \, \mu_B \frac{\sum_{M_J} M_J \exp\left[g \, \mu_B \, \beta M_J \, B_0\right]}{\sum_{M_J} \exp\left[g \, \mu_B \, \beta M_J \, B_0\right]}.$$ [3.19]

With the use of the Brillouin function

$$F(J, y) = \left(1 + \frac{1}{2J}\right) \coth\left[\left(1 + \frac{1}{2J}\right) y\right] - \frac{1}{2J} \coth\left[\frac{y}{2J}\right],$$ [3 20]

where

$$y = g \, \mu_B \, \beta \, J \, B_0,$$ [3.21]

the expression for $\langle \mu_{J\uparrow} \rangle$ can be written as

$$\langle \mu_{J\uparrow} \rangle = g\, \mu_B\, J\, F(J, y) \qquad \text{[3.22]}$$

For a system with N magnetic moments the magnetisation M is simply the sum of all moments $\langle \mu_{J\uparrow} \rangle$. The magnetic susceptibility is then defined as

$$\chi = \frac{\mu_0 M}{B}, \qquad \text{[3 23]}$$

where B is the applied magnetic field intensity and $\mu_0 = 4\pi\ 10^{-7}\ H\,m^{-1}$ is the permeability of free space. The molar susceptibility is written as χ_M and has the unit $\left[J\,T^{-2}\,mol^{-1} \right]$

Magnetic moment of the atomic nucleus

In the same way as described above for electrons, a very small magnetic moment occurs for an atomic nucleus associated with the spin angular momentum of the nucleus. The basic unit of magnetic moment in this case is the nuclear magneton μ_n

$$\mu_n = \frac{\hbar e}{2M_p} = 5\ 051\ 10^{-27}\ J\,T^{-1}, \qquad \text{[3.24]}$$

where M_p is the proton mass

This nuclear magneton is smaller than the Bohr magneton by m_e / M_p the ratio of the electron mass to the proton mass. Therefore, when discussing static magnetisation the magnetic nuclear moments can almost always be neglected compared to the electronic contributions.

25

Diamagnetism

Diamagnetism is associated with the tendency of electrical charges to partially shield the interior of a body from an applied magnetic field. This shielding is due to molecular currents induced by an external magnetic field such that, by Lenz's law, the induced magnetic moment is oriented in the opposite direction to the applied field. Clearly, a diamagnetic effect must always occur when any material is placed into a magnetic field and is therefore present in paramagnetic, ferromagnetic and antiferromagnetic materials.

The magnetic force, according to the Lorentz term $F = e \, \mathbf{v} \times \mathbf{B}$, rebalances the centrifugal and centripetal forces acting on the electrons so that the orbital frequency of an electron with its orbital magnetic moment parallel to the magnetic field is slowed down and the orbital frequency of an electron with its orbital magnetic moment antiparallel to the field is speeded up. The difference between both of these frequencies is the Larmor precession frequency

$$\Delta \omega = \frac{e \, B}{2 \, m_e}.$$
[3 25]

If the average electron current around the nucleus is initially zero an applied magnetic field will cause a current around the nucleus. The Larmor precession of Z electrons is then an electric current of magnitude

$$I = \left(\frac{-Z e \Delta \omega}{2 \pi} \right) = \left(\frac{-Z e^2 B}{4 \pi \, m_e} \right)$$
[3.26]

According to Ampère's law the induced current I must induce a magnetic dipole moment of magnitude

$$\mu = -\frac{Z e^2 B}{6 \, m_e} \left\langle r^2 \right\rangle,$$
[3.27]

where $\left\langle r^2 \right\rangle$ is the mean square distance of electrons from the nucleus of this atom

26

For a material with N similar atoms per unit volume the susceptibility is then

$$\chi = \frac{N \mu_0 \mu}{B} = -\frac{N \mu_0 Z e^2}{6 m_e} \langle r^2 \rangle$$

[3 28]

This is the classical result obtained by Langevin. It agrees with the result of quantum mechanical calculations. The value of the susceptibility is always negative.

Paramagnetism

As discussed above magnetic moments may occur in materials when the energy levels are not completely filled with electrons. In a solid containing N magnetic atoms per mole the magnetic moment μ_J for each atom is given by equation [3.14] The lowest energy state of a paramagnet and in the absence of a magnetic field is assumed by randomly oriented moments. So on average the magnetisation of a paramagnet is zero if no external field is applied. When a magnetic field is applied the energy of a dipole is given by equation [3.16] and the magnetic field causes a preferential orientation of the dipole moments Thus with increasing external field the magnetisation increases.

To discuss the paramagnetic behaviour in a solid the magnetic moment of an assembly of atoms or even of a whole solid has to be considered. For this the Brillouin function [3.20] is found to characterise the magnetic behaviour which is described by equation [3 22]. In many cases paramagnetic materials are observed and investigated under "weak conditions", that is the value of y can be assumed to be very small.

$$y = g \mu_B \beta J B_0 \ll 1$$

[3.29]

Therefore, for small values of y a series expansion for coth [y] can be used and the Brillouin function becomes, for $y \ll 1$

$$F(J, y) \approx \frac{y(J+1)}{3J}.$$ [3.30]

The mean total magnetic moment [3.22] is then

$$\langle \mu_{J\uparrow} \rangle = g \mu_B J F(J, y) = \frac{1}{3} g^2 \mu_B^2 \beta B_0 J (J+1)$$ [3.31]

The total magnetic moment, on the magnetisation per mole with N magnetic atoms in one mole and the molar susceptibility can be defined as

$$M_{mol} = N \langle \mu_{B\uparrow} \rangle$$ [3.32]

$$\chi_{mol} = \frac{M_{mol}}{B_0} = \frac{1}{3} N g^2 \mu_B^2 \beta J (J+1) = \frac{1}{3} N \mu_B^2 \beta p_{eff}^2,$$ [3.33]

where p_{eff} is the paramagnetic number of the Bohr magneton [1]

$$p_{eff} = g \sqrt{J(J+1)}.$$ [3.34]

Substituting $\beta = (k_B T)^{-1}$ yields

$$\chi_{mol} = \frac{N \mu_B^2 p_{eff}^2}{3 k_B T} = \frac{C_{mol}}{T}.$$ [3.35]

This is the Curie law with C_{mol} as the molar Curie constant.

Therefore the paramagnetic number of the Bohr magneton p_{eff} can be obtained by magnetisation measurements as

$$p_{eff}^2 = \frac{3 k_B}{N \mu_B^2} C_{mol}$$ [3.36]

---

[1] Note that p_{eff} is different to μ_{eff} by the Bohr magneton μ_B such as $\mu_{eff} = p_{eff} \mu_B$

28

Ferromagnetism

In the absence of an applied magnetic field a ferromagnet has a permanent magnetisation The origin of this magnetisation lies in the parallel alignment of magnetic moments in domains which the ferromagnetic material is divided into. Therefore, each domain is spontaneously magnetised almost to saturation. Usually the domains are randomly orientated and thus the average magnetisation of the whole material is very small in comparison to the intrinsic magnetisation within the domains.

An applied field changes the distribution of magnetisation domains in a manner so as to align the domains with the field. This results in the familiar behaviour known as hysteresis in ferromagnets.

Now the magnetisation can be derived in the same way as discussed for paramagnetic materials [3.22]. But in this case the intrinsic magnetisation has to be taken into consideration. If there are N magnetic atoms per molar unit the intrinsic magnetisation is

$$M_{int} = N \langle \mu_{J\uparrow} \rangle.$$ [3.37]

Further, the superposition of the applied field B_0 and the internal field B_{int} created by the intrinsic magnetisation has also to be considered

$$B = B_0 + B_{int} = B_0 + \gamma_{mol} M_{int} = B_0 + \gamma_{mol} N \langle \mu_{J\uparrow} \rangle,$$ [3.38]

where γ_{mol} a constant of proportionality called the molecular field coefficient. So the magnetisation is given by equation [3.22] after replacing the external field B_0 with B

$$\langle \mu_{J\uparrow} \rangle = g \, \mu_B \, J \, F(J, y_{ferro}),$$ [3.39]

where $F(J, y_{ferro})$ is the Brillouin function [3.20] with

$$y_{ferro} = g\,\mu_B\,\beta\,J\left(B_0 + \gamma_{mol}\,N\langle\mu_{J\uparrow}\rangle\right)$$ [3.40]

Now y_{ferro} depends on the total magnetic moment and thus the term $\langle\mu_{J\uparrow}\rangle$ appears on both sides of equation [3.39]. If only the spontaneous magnetisation is considered, for which the applied field is zero, then the value for B_0 in [3.40] disappears and y_{ferro} becomes

$$y_{ferro} = g\,\mu_B\,\beta\,J\,\gamma_{mol}\,N\langle\mu_{J\uparrow}\rangle$$ [3.41]

and so a second equation can be derived for the total magnetic moment.

$$\langle\mu_{J\uparrow}\rangle = \frac{1}{g\,\mu_B\,\beta\,J\,\gamma_{mol}\,N}\,y_{ferro},$$ [3 42]

where $\beta = (k_B T)^{-1}$.

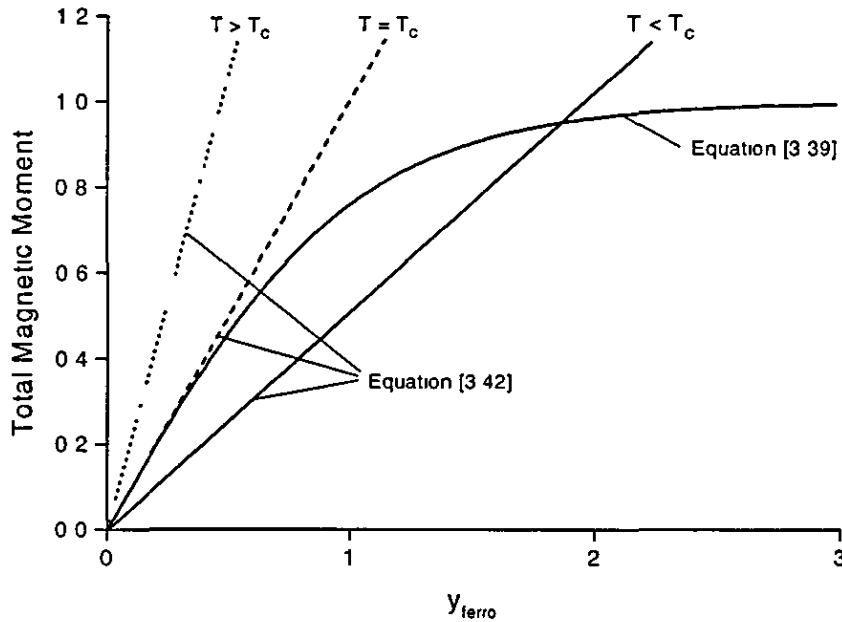In figure 3.1.1 curves of both equations [3.39] and [3.42] are shown.

Figure 3.1 1· Graphical solution of equation [3 39] and [3 42] for the total mean magnetic moment $\langle\mu_{J\uparrow}\rangle$ as a function of y_{ferro} for various temperatures

In figure 3.1 it is seen that for T < T_C the graphs have two intersections. The non-zero intersection can be seen as a point for which the spontaneous magnetisation is equal to the intrinsic magnetisation. This non-zero intersection will change as a function of temperature. With increasing temperature the graph of equation [3.39] will be unchanged, but the slope of the graph of equation [3.42] will increase. At the transition temperature, the ferromagnetic Curie temperature T_c, the slope of graph Eq.[3.42] will exceed the initial slope of the graph of Eq.[3.39] and the ferromagnetic material becomes paramagnetic.

In figure 3.1 2 the calculated variation is shown of the reduced spontaneous magnetisation M/M_0 against the reduced temperature T/T_C.
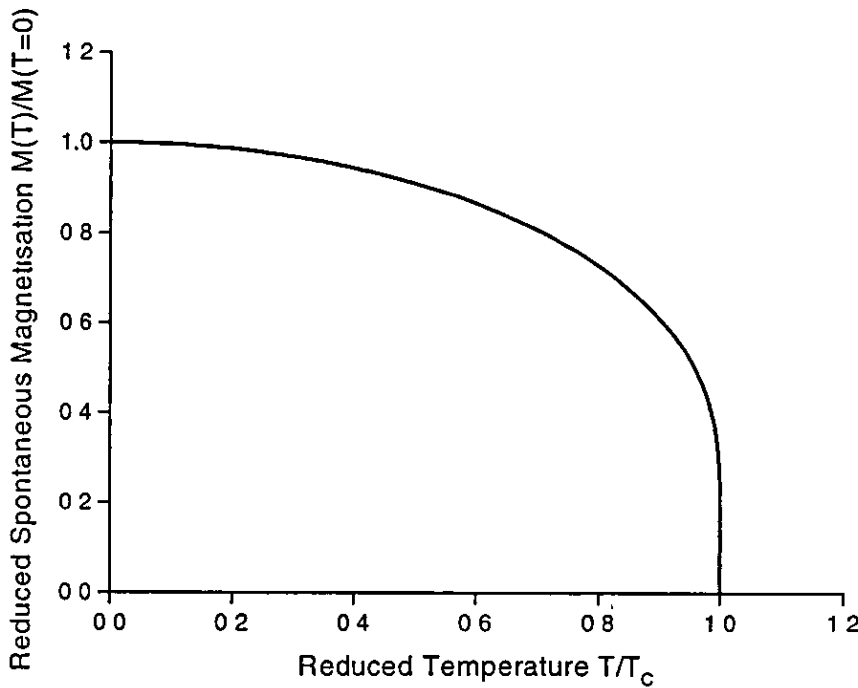

Figure 3 1 2· Spontaneous magnetisation as a function of temperature for J = 1/2

At temperatures above the Curie temperature the ferromagnet shows paramagnetic behaviour. Again it can be assumed that y_{ferro} is small and thus

31

$$F(J, y_{ferro}) \approx \frac{y_{ferro}(J+1)}{3J}.$$ [3.43]

The mean total magnetic moment is then

$$\langle \mu_{J\uparrow} \rangle = g\,\mu_B\,J\,F(J, y_{ferro}) = \frac{1}{3}g^2\,\mu_B^2\,\beta\left(B_0 + \gamma_{mol}\,N\langle \mu_{J\uparrow}\rangle\right)J(J+1)$$ [3.44]

$$\langle \mu_{J\uparrow}\rangle = \frac{1}{3}g^2\,\mu_B^2\,\beta\,J(J+1)B_0 + \frac{1}{3}g^2\,\mu_B^2\,\beta\,J(J+1)\gamma_{mol}\,N\langle \mu_{J\uparrow}\rangle$$ [3.45]

$$\langle \mu_{J\uparrow}\rangle = \frac{\frac{1}{3}g^2\,\mu_B^2\,\beta\,J(J+1)B_0}{1 - \frac{1}{3}g^2\,\mu_B^2\,\beta\,J(J+1)\gamma_{mol}\,N}$$ [3.46]

$$\langle \mu_{J\uparrow}\rangle = \frac{\frac{1}{3k_B}g^2\,\mu_B^2\,J(J+1)B_0}{T - \frac{1}{3k_B}g^2\,\mu_B^2\,J(J+1)\gamma_{mol}\,N} = \frac{\frac{1}{3k_B}g^2\,\mu_B^2\,J(J+1)B_0}{T - \theta_C}.$$ [3.47]

In this case the susceptibility is given by

$$\chi_{mol} = \frac{N\langle \mu_{J\uparrow}\rangle}{B_0} = \frac{\frac{1}{3k_B}N\,g^2\,\mu_B^2\,J(J+1)}{T - \theta_C} = \frac{C_{mol}}{T - \theta_C},$$ [3.48]

where N is the number of magnetic atoms, C_{mol} the molar Curie constant and θ_C the paramagnetic Curie temperature

$$C_{mol} = \frac{N\,\mu_B^2\,p_{eff}^2}{3k_B}$$ [3.49]

$$\theta_C = \frac{\mu_B^2\,\gamma_{mol}\,N\,p_{eff}^2}{3k_B}$$ [3 50]

Equation [3.48] is the Curie-Weiss law. Again the effective paramagnetic number of the Bohr magneton p_{eff} is obtained as

$$p_{eff}^2 = \frac{3 k_B}{N \mu_B^2} C_{mol}$$ [3.51]

and

$$p_{eff} = g \sqrt{J(J+1)}.$$ [3.52]

According to the above analysis θ_c and the Curie temperature T_c are identical. However, experiments show that θ_c is often larger than T_c. Howevei, the difference is usually small.

Antiferromagnetism

Antiferromagnetic order constitutes an ordered state for which some magnetic moments aie aligned antiparallel to one another. No net macroscopic magnetic moment occurs Above the transition temperature (Néel temperature T_N) the alignment of the magnetic moments disappears and the antiferromagnetic material exhibits paramagnetic behaviour

The simplest way to describe antiferiomagnetism is to divide the whole solid into two sublattices so that each sublattices forms a ferromagnet in which the magnetic moments aie aligned in the same direction. Both sublattices are orientated so that if the magnetic moments of one sublattice point in one direction, those of the others sublattice point in the opposite direction Furthermore, the sublattices are ordered so that the moments of nearest neighbour atoms are antiparallel. The simple cubic and body-centred-cubic lattice are examples of lattices which satisfy this condition Hence two intiinsic magnetic fields may be taken into consideration for both sublattices concerned and so the magnetisation of an antiferromagnetic material can be derived.

The intrinsic magnetisation of each sublattice A and B can be written as

$$M_{\text{int } i} = \frac{1}{2} N \langle \mu_{J\uparrow} \rangle_i , \quad i = A, B \tag{3.53}$$

for N magnetic atoms. Considering only the first nearest and second nearest neighbour interactions the internal magnetic fields are given by

$$B_{\text{int } A} = \gamma_{AA} M_{\text{int } A} + \gamma_{AB} M_{\text{int } B} \tag{3.54}$$

and

$$B_{\text{int } B} = \gamma_{BA} M_{\text{int } A} + \gamma_{BB} M_{\text{int } B} , \tag{3 55}$$

where the γ's are different field coefficients.

In simple cubic and body-centred-cubic lattice type the sublattices are equivalent and thus

$$\gamma_{AB} = \gamma_{BA} = -\gamma_1 \quad \text{and} \quad \gamma_{AA} = \gamma_{BB} = -\gamma_2 ,$$

where

$$\gamma_1 - \gamma_2 = \gamma . ^{\text{I}} \tag{3.56}$$

The mean magnetic moment for each sublattices can be calculated in the same way as before for ferromagnets. (see equation [3.39])

$$\langle \mu_{J\uparrow} \rangle_A = g \mu_B J F(J, y_A), \tag{3.57}$$

with

$$y_A = g \mu_B \beta J (B_0 + B_{\text{int } A}) = g \mu_B \beta J (B_0 - \gamma_2 M_{\text{int } A} - \gamma_1 M_{\text{int } B}) \tag{3.58}$$

and

$$\langle \mu_{J\uparrow} \rangle_B = g \mu_B J F(J, y_B), \tag{3.59}$$

[I] Note that here γ is equivalent to γ_{mol}

with

$$y_B = g\,\mu_B\,\beta\,J\left(B_0 + B_{int\,B}\right) = g\,\mu_B\,\beta\,J\left(B_0 - \gamma_1\,M_{int\,A} - \gamma_2\,M_{int\,B}\right) \qquad [3\,60]$$

For a perfect antiferromagnet the number of magnetic atoms in lattice A is equal to the number of magnetic atoms in lattice B. Also the magnitude of the magnetisation is the same for both sublattices. Therefore it can be assumed that

$$M_{int\,A} = -M_{int\,B} \qquad [3.61]$$

and y_A, y_B become

$$y_A = g\,\mu_B\,\beta\,J\left(B_0 + \gamma\,M_{int\,A}\right) \qquad [3.62]$$

$$y_B = g\,\mu_B\,\beta\,J\left(B_0 - \gamma\,M_{int\,A}\right) \qquad [3.63]$$

In the absence of an external magnetic field the value for B_0 disappears. In figure 3.1.3 the reduced spontaneous magnetisations for both sublattices are shown respectively.

In order to study the susceptibility in an external magnetic field the superposition of the external field and both intrinsic fields has to be considered.

$$B = B_0 + B_{int\,A} + B_{int\,B} = B_0 - \gamma_2 M_{int\,A} - \gamma_1 M_{int\,B} - \gamma_1 M_{int\,A} - \gamma_2 M_{int\,B} \qquad [3.64]$$

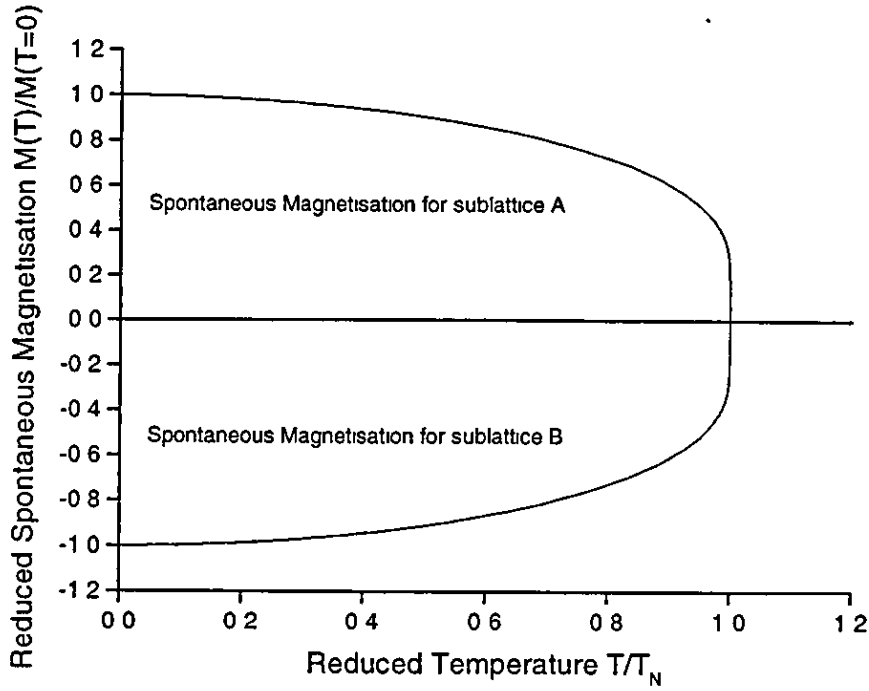$$B = B_0 - \gamma\left(M_{int\,A} + M_{int\,B}\right) \qquad [3.65]$$

Figure 3 1 3· Plot of the spontaneous magnetisation versus temperature of the sublattices A and B in a simple antiferromagnet

Furthermore, it can be assumed that the magnetisation is small and the approximation [3.30] can be used for the Brillouin function. So the total mean magnetic moment is

$$\left\langle \mu_{J\uparrow} \right\rangle_A + \left\langle \mu_{J\uparrow} \right\rangle_B = \frac{1}{3} g^2 \mu_B^2 \beta J (J+1) \left(B_0 - \gamma \frac{1}{2} N \left(\left\langle \mu_{J\uparrow} \right\rangle_A + \left\langle \mu_{J\uparrow} \right\rangle_B \right) \right)$$

[3.66]

$$\left\langle \mu_{J\uparrow} \right\rangle_A + \left\langle \mu_{J\uparrow} \right\rangle_B = \frac{\frac{1}{3} g^2 \mu_B^2 \beta J (J+1) B_0}{1 + \frac{1}{3} g^2 \mu_B^2 \beta J (J+1) \gamma \frac{1}{2} N}$$

[3.67]

$$\left\langle \mu_{J\uparrow} \right\rangle_A + \left\langle \mu_{J\uparrow} \right\rangle_B = \frac{\frac{1}{3k_B} g^2 \mu_B^2 J (J+1) B_0}{T + \frac{1}{3k_B} g^2 \mu_B^2 J (J+1) \gamma \frac{1}{2} N} = \frac{\frac{1}{3k_B} g^2 \mu_B^2 J (J+1) B_0}{T - \theta_N}$$

[3.68]

36

The susceptibility is then given by

$$\chi_{mol} = \frac{N\left(\langle\mu_{J\uparrow}\rangle_A + \langle\mu_{J\uparrow}\rangle_B\right)}{B_0} = \frac{\frac{1}{3k_B}N g^2 \mu_B^2 J(J+1)}{T-\theta_N} = \frac{C_{mol}}{T-\theta_N},$$ [3 69]

with

$$C_{mol} = \frac{N \mu_B^2 p_{eff}^2}{3 k_B}$$ [3.70]

and

$$\theta_N = -\frac{1}{2}\frac{\mu_B^2 \gamma N p_{eff}^2}{3 k_B}$$ [3 71]

A paramagnetic behaviour described by the Curie-Weiss law is found for an antiferromagnet above the transition temperature T_N. However, a negative value is obtained for the temperature θ_N. Thus the Néel temperature T_N and θ_N have opposite signs and the relationship between them depends on the structure of the sublattices

Below the transition temperature T_N the susceptibility has to be discussed for two different situations depending on whether the field is applied parallel or perpendicular to the orientation of the magnetic moments

If the field B_0 is applied perpendicular to the moments then the moments are slightly deflected out of the intrinsic field directions by an angle φ and a torque $B_0 \cos\varphi$ acts on one sublattice. As this deflection arises in both sublattices, the intrinsic field of the second sublattice $B_{int A}$ also exerts a torque of $\gamma_1 M_{int A} \sin 2\varphi$ on the first lattice. In equilibrium both of the exerted torques are equal.

$$B_0 \cos\varphi = \gamma_1 M_{int A} \sin 2\varphi$$ [3.72]

As already described the deflection angle φ is small and the small angle approximations may be used so that $\cos\varphi \approx 1$ and $\sin\varphi \approx \varphi$. With these equation [3.72] becomes

$$B_0 = \gamma_1 M_{int\,A} 2\varphi.$$ [3.73]

Assuming that $M_{int} = M_{int\,A} + M_{int\,B} = 2 M_{int\,A}$ the perpendicular susceptibility is given by

$$\chi_\perp = \frac{M_{int}\,\varphi}{B_0} = \frac{M_{int}\,\varphi}{\gamma_1 M_{int\,A} 2\varphi} = \frac{1}{\gamma_1},$$ [3.74]

where $M_{int}\,\varphi$ is the induced magnetisation in the direction of the applied field The perpendicular susceptibility is temperature independent (as long as the coefficient γ_1 does not depend on temperature) and so up to the transition temperature T_N has an almost constant contribution.

If the field is applied parallel to the direction of the magnetic moments the intrinsic magnetisations $M_{int\,A}, M_{int\,B}$ will be different in each sublattice, because the magnetic moments which are aligned parallel to the field will be less affected than the moments which are antiparallel. In calculating the parallel susceptibility

$$\chi_\| = \frac{\Delta M_{int\,A} + \Delta M_{int\,B}}{B_0}$$ [3.75]

the change in each magnetisation $\Delta M_{int\,A}, \Delta M_{int\,B}$ has to be known when the field is increased from zero to value B_0.

To obtain these changes it is convenient to use the same derivation for both magnetisations $M_{int\,A}$ and $M_{int\,B}$ as discussed above (equation [3.53]) Assuming that the field is parallel to $M_{int\,A}$ and antiparallel to $M_{int\,B}$, $M_{int\,A}$ and $M_{int\,B}$ are obtained as

$$M_{\text{int }A} = \frac{1}{2} N g \mu_B J F(J, y_A),$$ [3.76]

with

$$y_A = g \mu_B \beta J \left(\gamma M_{\text{int }A} + B_0 \right)$$ [3.77]

and

$$M_{\text{int }B} = \frac{1}{2} N g \mu_B J F(J, y_B),$$ [3 78]

with

$$y_B = g \mu_B \beta J \left(\gamma M_{\text{int }B} - B_0 \right).$$ [3.79]

From equation [3.77] and [3 79] linear functions in y_A and y_B can be obtained

$$M_{\text{int }A} = \frac{k_B T}{g \mu_B J \gamma} y_A - \frac{B_0}{\gamma} = mT \, y_A - b$$ [3.80]

$$M_{\text{int }B} = \frac{k_B T}{g \mu_B J \gamma} y_B + \frac{B_0}{\gamma} = mT \, y_B + b,$$ [3.81]

where $m = \dfrac{k_B}{g \mu_B J \gamma}$ and $b = \dfrac{B_0}{\gamma}$.

In zero magnetic field both equations become

$$M_{\text{int }A\,B} = \frac{k_B T}{g \mu_B J \gamma} y_{A\,B} = mT \, y_{A\,B},$$ [3.82]

which is qualitatively the same equation as obtained for a ferromagnet (equation [3 42]). Therefore, the change in each magnetisation may be obtained by the change in the values of the intersection points from equations [3 80] and [3.82] with equation [3 76] for $\Delta M_{\text{int }A}$ and from the equations [3.81] and [3 82] with equation [3.78] for $\Delta M_{\text{int }B}$. Figure 3.1 4 shows a sketch of these equations.
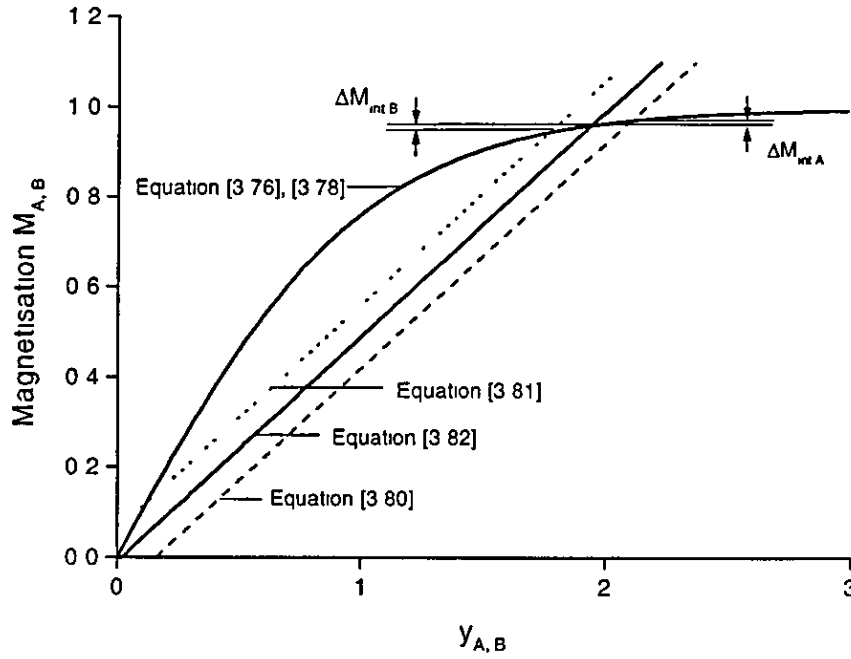
Figure 3 1 4   Graphic solution of equations [3 80],[3 81], [3 82] and [3 76], [3 78] for the magnetisation as a function of temperature and for the changes in the magnetisation of $M_{int A}$ and $M_{int B}$

It can be seen that the changes in the magnetisation are given by the product of $\pm g\,\mu_B\,\beta\,J\,B_0$ with the gradients of equation [3.76] or [3.78], respectively, at the intersection point if the applied field has a constant value.

Furthermore, both values for $\Delta M_{int A}$ and $\Delta M_{int B}$ are the same as long as the intrinsic magnetic fields have the same magnitude in zero field. Thus, the susceptibility is approximately proportional to the gradient of the plot of the Brillouin function against $y_{A\,B}$ evaluated for zero applied field. The parallel susceptibility is zero at zero temperature and has the same value as the perpendicular susceptibility at the transition temperature T_N. For a randomly oriented polycrystalline antiferromagnet the parallel susceptibility increases with increasing temperature according to the gradient of the Brillouin function in a way such that the overall susceptibility is always

40

$$\chi_{antiferro} = \frac{2}{3}\chi_\perp + \frac{1}{3}\chi_\parallel.$$ [3.83]

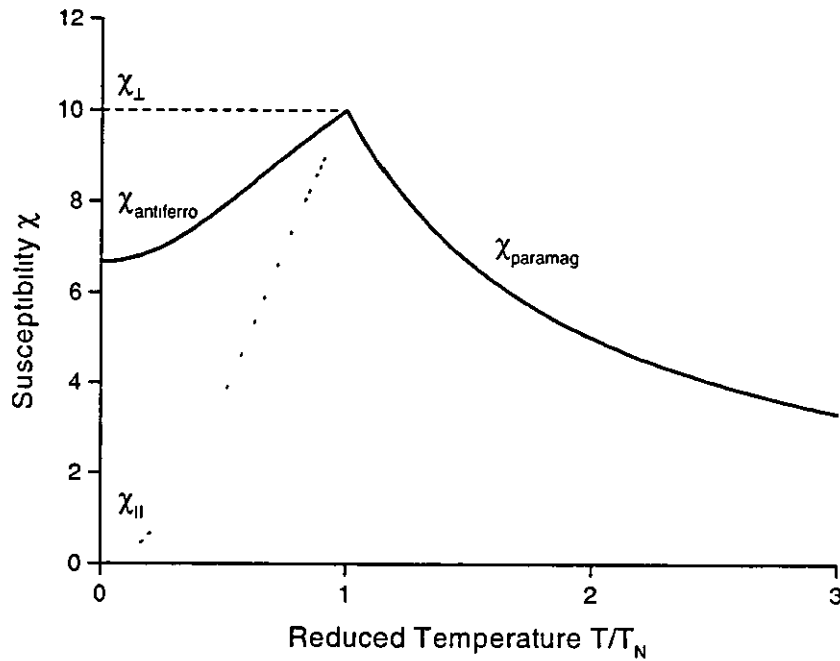In figure 3.1 5 the susceptibility below and above the transition temperature is shown.

Figure 3 1 5· Calculated magnetic susceptibilities as a function of temperature of a simple antiferromagnet The parallel $\chi_\parallel$, perpendicular $\chi_\perp$ and the powder averaged susceptibility $\chi_{antiferro}$ are shown

Arrott plots

The analysis of magnetic properties is a field in which Landau theory has proved particularly useful It is the notion of an order parameter and the fact that the symmetry of the system can be treated exactly that makes this approach particularly attractive [9]. The basis of Arrott plots is a Landau description of the magnetisation using an expansion of the free energy in powers of the magnetic order parameter, the ferromagnetic moment for a ferromagnet and the staggered magnetisation for an antiferromagnet. The magnetic behaviour may be described

41

using a small number of possible temperature dependent coefficients. In order to obtain the free energy expansion the partition function Z_0 for a magnetic system has to be considered. The partition function is

$$Z_0 = \sum_{m=-J}^{J} \exp[-\beta \varepsilon(m)]$$ [3.84]

with the energy eigenvalues

$$\varepsilon(m) = g \mu_B m B$$ [3.85]

where B is the superposition of the external and internal magnetic fields

$$B = B_0 + B_{int}.$$ [3.86]

The knowledge of the partition function suffices for the modelling of the thermodynamic behaviour of the system of non-interacting magnetic moments in an effective field which contains the interaction between the magnetic moments. In the high temperature limit, $\beta \varepsilon(m) \ll 1$, the partition function can be expanded into a powers series in β and it takes the form

$$\frac{Z_0}{(2J+1)} = 1 + \frac{\beta^2}{6} J(J+1) g^2 \mu_B^2 B^2$$
$$+ \beta^4 J(J+1)(2J-1)(3J^2 + 3J - 1)\frac{g^4 \mu_B^4}{360} B^4 + \ldots$$ [3.87]

From this expansion an approximate form of the free energy is obtained by

$$F_0 = -\frac{N}{\beta} \ln[Z_0],$$ [3.88]

from which in turn the average magnetic moment per magnetic atom is calculated using

$$M = -\frac{1}{N}\frac{\partial F_0(M)}{\partial B} = \frac{1}{\beta Z_0}\frac{\partial Z_0}{\partial B}.$$ [3.89]

Thus,

$$M = \beta J (J+1)\frac{g^2 \mu_B^2}{3} B - \frac{\beta^3}{90} J (J+1)(2J^2 + 2J + 1)g^4 \mu_B^4 B^3 + \ldots$$

$$M = \chi B + \chi^{(3)} B^3 . \tag{3.90}$$

The free energy as a function of the order parameter M and normalised to one magnetic atom is given by

$$\frac{F_0}{N} = \frac{F_0^*}{N} + \frac{1}{2}AM^2 + \frac{1}{4}CM^4 - BM . \tag{3.91}$$

Here A and C are expansion coefficients. All contributions which do not depend on the magnetisation are contained in the term F_0^* which will be omitted from all further formulae.

The magnetic moment obtained by minimisation of the free energy expansion with respect to M

$$0 = \frac{\partial F_0}{\partial M} = AM + CM^3 - B. \tag{3.92}$$

For small magnetic fields B the magnetisation increases linearly with increasing field. The coefficient A is assumed to be temperature dependent according to

$$A = \frac{1}{\chi} = 3\frac{k_B T}{J(J+1)} . \tag{3.93}$$

The coefficient C is taken to be temperature independent. It is related to the third order susceptibility.

Equation [3.92] can be written in the form

$$M^2 = \frac{1}{C}\frac{B}{M} - \frac{A}{C} = \frac{1}{C}\frac{B_0}{M} - \frac{A^*}{C} \tag{3.94}$$

where A* is the coefficient which appropriate for an interacting system.

$$A^* = 3\frac{k_B}{J(J+1)}(T - \theta_c)$$ [3.95]

and θ_c is the paramagnetic Curie temperature.

The equation [3 94] resembles the equation of a straight line. Plotting the magnetisation for a given temperature as a function of field and using units of the ratio of applied field divided by the observed magnetisation on the x-axis and the square of the magnetisation on the y-axis will yields straight lines with $\frac{1}{C}$ as the slope and $-\frac{A^*}{C}$ as the intersection point with the M^2 axis. The intersection point with the x-axis is given by the coefficient A* and is directly related to the inverse susceptibility in zero field (see equation [3 93]) As discussed above the coefficient A* is proportional to the temperature and C is temperature independent. As temperature is varied the lines of the Arrott plots are displaced parallel to each other. The temperature of the isotherm which intersects the origin of the Arrott plot is the ferromagnetic transition temperature $T_C = \theta_c$. For temperatures which are smaller than T_C the straight lines cut the M^2 axis at positive values and give the value of the spontaneous magnetisation in the absence of a magnetic field. Thus Arrott plots are a more physically transparent and useful tool for the analysis and description of magnetic materials.

Temperature shift of an antiferromagnetic phase transition

In the subsection "Arrott plots" the Landau description of the magnetisation is discussed using an expansion of the free energy F in powers of the magnetic order parameter M. Consider the same expansion of the free energy with two magnetic order parameters M and L where M is the ferromagnetic and L the antiferromagnetic order parameter. The free energy can then formulated as

44

$$F = F_0 + \frac{a}{2}M^2 + \frac{b}{2}L^2 + \frac{c}{4}L^4 + \frac{d}{2}L^2 M^2 - BM \; , \qquad\qquad [3.96]$$

where the coefficients a and b are temperature dependent and c and d are taken to be independent of temperature.

The model is designed to describe the influence of an external magnetic field on an antiferromagnetic phase transition. The minimisation of the free energy with respect to both order parameters yields

$$0 = \frac{\partial F}{\partial M} = aM + d \cdot L^2 M - B \qquad\qquad [3\,97]$$

$$0 = \frac{\partial F}{\partial L} = bL + c\,L^3 + d \cdot LM^2 \qquad\qquad [3.98]$$

Therefore M can expressed by

$$M = \frac{1}{a + d \cdot L^2} B = \chi\,B \, . \qquad\qquad [3\,99]$$

In the paramagnetic region the antiferromagnetic order parameter L is zero resulting in

$$M = \frac{B}{a} \qquad\qquad [3.100]$$

The temperature dependence of the coefficient a is taken as

$$a = \frac{T - \theta_p}{C} \, . \qquad\qquad [3.101]$$

According to equation [3 99] the resulting susceptibility has a Curie-Weiss behaviour.

$$\chi = \frac{M}{B} = \frac{C}{T - \theta_N} \, , \qquad\qquad [3.102]$$

where θ_N is the paramagnetic Curie temperature and C the Curie constant.

45

Below the antiferromagnetic transition the magnetic behaviour is altered due to a non-zero antiferromagnetic order parameter L. Thus the inverse susceptibility increases below the phase transition according to

$$\frac{1}{\chi} = \frac{B}{M} = \frac{T - \theta_P}{C} + d \cdot L^2.$$ [3.103]

Minimisation of the free energy with respect to L (equation [3.98]) yields the following equation for L

$$0 = L(b + d \cdot M^2) + c L^3$$ [3.104]

and thus three solutions are obtained

$$L = 0$$ [3 105]

or

$$L^2 = -\frac{(b + d \cdot M^2)}{c}$$ [3 106]

In the absence of a field the ferromagnetic component M for an antiferromagnet is zero. Below the antiferromagnetic phase transition the order parameter L takes the value

$$L^2 = -\frac{b}{c}$$ [3.107]

This equation has only a physical solution if b is negative. The temperature dependent coefficient b can be taken as

$$b = \frac{T - T_N}{\beta},$$ [3.108]

where β is a temperature independent constant, and thus

$$L^2 = -\frac{T - T_N}{\beta\, c}.$$

[3.109]

T_N is the antiferromagnetic transition temperature, the Néel temperature. Above the Néel temperature the term on the right hand side in [3.109] is negative and the solution which minimises the free energy is equation [3.105] $L = 0$ is. For temperatures below T_N equation [3.106] yields a non-zero L-value.

$$L^2 = -\frac{T - T_N}{\beta\, c} - \frac{d \cdot M^2}{c}$$

[3.110]

For a non-zero external magnetic field the field dependent transition temperature $\tilde{T}_N = T_N(B)$ is determined by

$$L^2 = -\frac{\tilde{T}_N - T_N(B = 0)}{\beta\, c} - \frac{d \cdot M^2}{c} = 0$$

[3 111]

and

$$\tilde{T}_N = T_N(B = 0) - \beta\, d \cdot M^2$$

[3.112]

The constants β and d are positive numbers and thus the antiferromagnetic transition is expected to be shifted to lower temperatures if an external magnetic field is applied As $M \sim B$ the shift in the transition temperature is a linear function of the square of the applied field.

3.2 Description of Magnetisation Measurements Apparatus

The Superconducting Quantum Interference Device (SQUID)

A Superconducting Quantum Interface Device, SQUID for short, was used to measure the magnetic properties of the rare earth-silver alloys This device is widely accepted as the most accurate method of measuring magnetic moments. The resolution of 10^{-8} e.m u (10^{-11} JT^{-1}) allows accurate measurements of samples with small magnetic moments. This highly sensitive method was sufficient to investigate the magnetic properties of the rare-earth samples. Even for the $La_{14}Ag_{51}$ sample, the non-magnetic reference compound, this method was very useful

The SQUID is a sophisticated analytical instrument configured specifically for the investigation of the magnetic properties of small experimental samples over a broad range of temperatures and magnetic fields. The magnetometer consists of a superconducting solenoid, a SQUID detector system, a sample transport mechanism, a liquid helium dewar, a temperature control module and an electronic control console which is connected to a HP computer with installed Control System software [10]. The superconducting solenoid includes a superconducting magnet, which consists of a multifilament superconducting wire. This magnet provides a reversible field operation to plus or minus 5 5 Tesla using an oscillatory technique to minimise magnet drift immediately following field changes. Together with the temperature control system the whole device provides an actively regulated, precision thermal environment over a temperature range of 1 7K to 400K

Sensing pick-up loops, also consisting of a superconducting wire, are mounted in the solenoid and connected to a signal coil in the SQUID detector system below the solenoid Furthermore, the detector system contains RF bias, which is connected to the amplifier and the SQUID ring between the signal coil and the

48

RF bias. This SQUID ring is a superconducting wire with a small insulating layer, the "weak link". The flux induced in the signal coil and passing through the ring is quantised once the ring has gone superconducting but the "weak link" forces the flux trapped in the ring to change only by discrete amounts. Quantised changes in flux occur as a result of tunnelling by electrons through a Josephson junction in the SQUID ring. These quantised changes are used by the instrument to calculate the magnetic moment of the sample. In figure 3.2.1 a schematic view is shown of the SQUID.
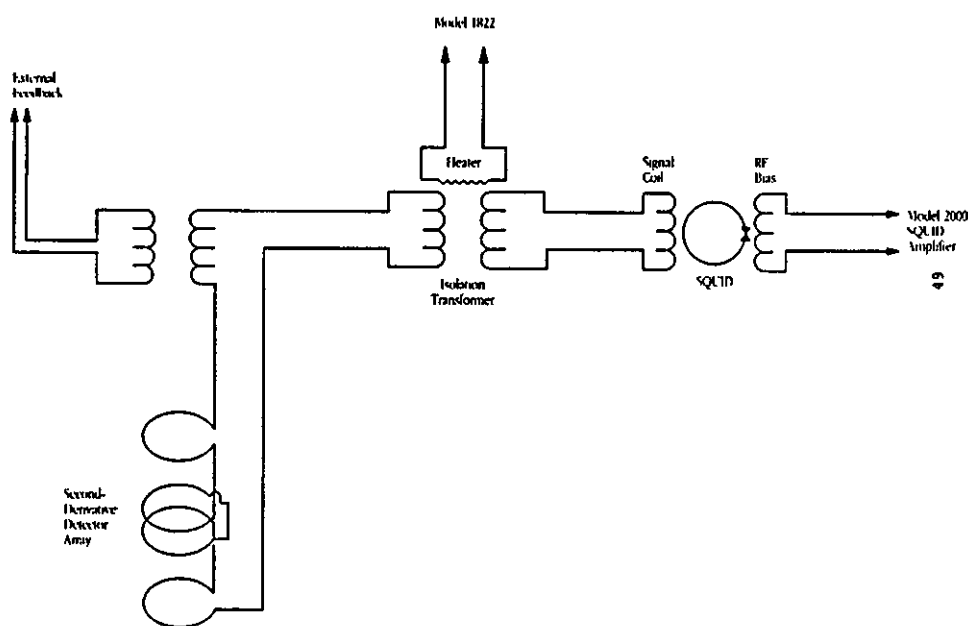
Figure 3 2 1. Schematic view of the SQUID

For measurements of the magnetic moment the sample was placed below the detection loops with the transport set at its lower limit of travel The sample was then raised through the sensing loops while measuring the output of the SQIUD detector. The moment was then measured by repeatedly moving the sample upwards in small steps and reading the voltage from the SQUID detector at each position. The SQUID voltage for these measurements was read as a number of 64 points over a scale of 6cm and with 100 readings at each sample position. This procedure was performed three times. The final average voltage data is plotted as a function of the sample position as shown in figure 3.2.2 and is referred to as a scan

49

3.3 Experimental Results

Experimental work

A small piece of the rare-earth compound (see table 3 3.1) was placed inside a plastic capsule with a very small amount of grease and cotton wool. This capsule was placed in a plastic tube and connected to the sample transport mechanism All samples were cooled down to 5 K in zero field.

Sample	Weight [g]	Relative atomic mass [g/mol]	Number of mole [mol]
$La_{14}Ag_{51}$	0 4399 ± 0 0001	7445 945	$(5\ 908 \pm 0\ 001)\ 10^{-5}$
$Gd_{14}Ag_{51}$	0 0127 ± 0 0001	7702 87	$(1\ 65 \pm 0\ 01)\ 10^{-6}$
$Tb_{14}Ag_{51}$	0 0229 ± 0 0001	7726 32	$(2\ 96 \pm 0\ 01)\ 10^{-6}$
$Dy_{14}Ag_{51}$	0 0253 ± 0 0001	7776 37	$(3\ 25 \pm 0\ 01)\ 10^{-6}$
$Ho_{14}Ag_{51}$	0 0247 ± 0 0001	7810 39	$(3\ 16 \pm 0\ 01)\ 10^{-6}$
$Er_{14}Ag_{51}$	0 0213 ± 0 0001	7843 01	$(2\ 72 \pm 0\ 01)\ 10^{-6}$

Table 3 3 1 Weight, relative atomic mass and number of mole of samples used

The magnetisation measurements for the polycrystalline samples were carried out in two different ways. First of all the magnetisation was measured as a function of temperature in various constant external magnetic fields. Secondly the magnetisation was measured as a function of applied field at constant temperature. From the latter measurements Arrott Plots were created for different temperatures. The MPMS-SQUID system created a data file including temperature in Kelvin, applied fields in gauss, magnetic moment in e m u. and magnetic susceptibility in e.m u./gauss. This data was converted into SI-units and normalised to the molar weight of one unit cell for each alloy.

The alloy Gd$_{14}$Ag$_{51}$

Magnetic measurements in various constant applied magnetic fields (0.01, 0 05, 0 09, 0 25, 0 5, 0.75, 1, 2, 3, 4 and 5.5 Tesla) have been carried out over the temperature range from 1 8 to 300 K. The results are shown in figures 3.3.1 – 3.3.4
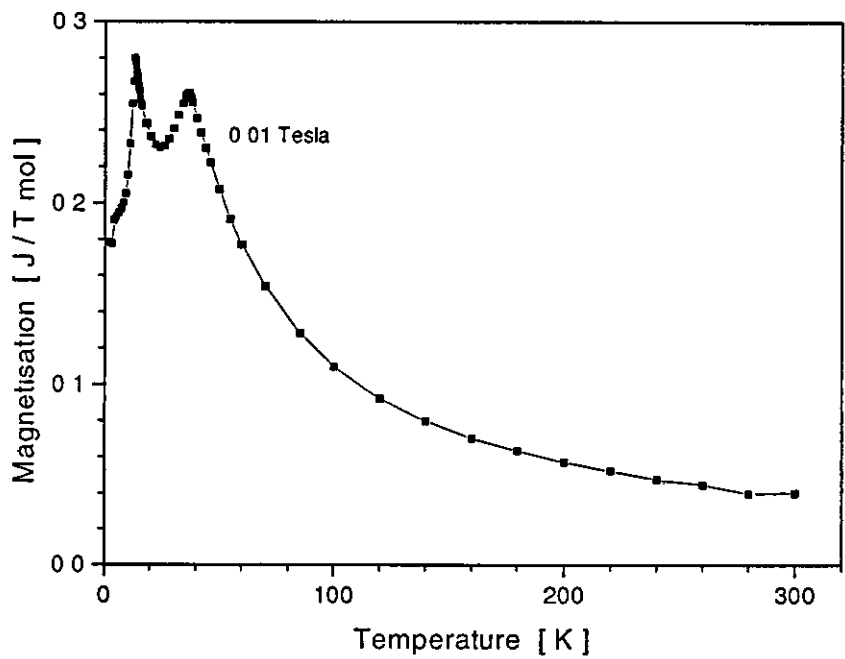
Figure 3 3 1   Molar magnetisation of Gd$_{14}$Ag$_{51}$ as a function of temperature at an applied magnetic field of 0 01 Tesla
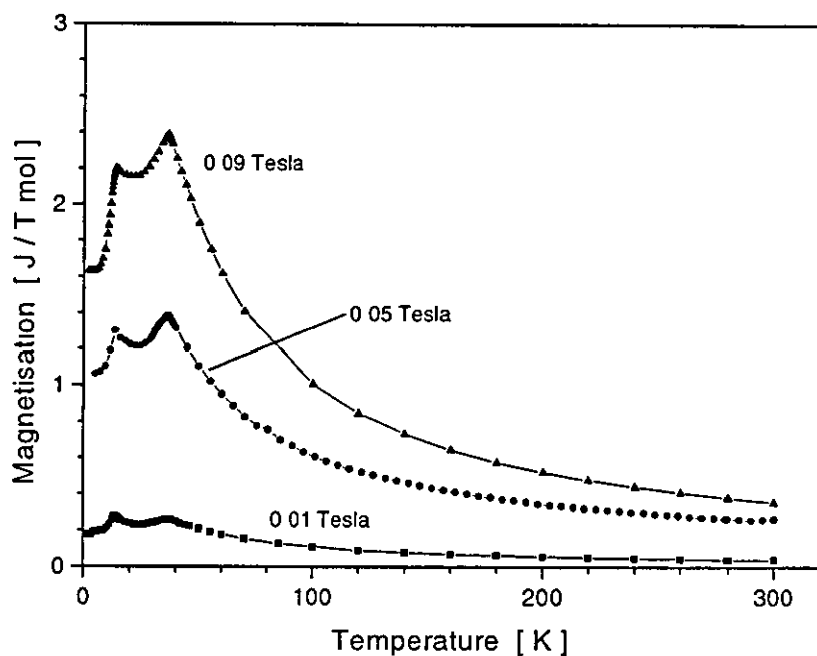
Figure 3 3 2 Molar magnetisation of Gd₁₄Ag₅₁ as a function of temperature at applied magnetic fields of 0 01, 0 05 and 0 09 Tesla
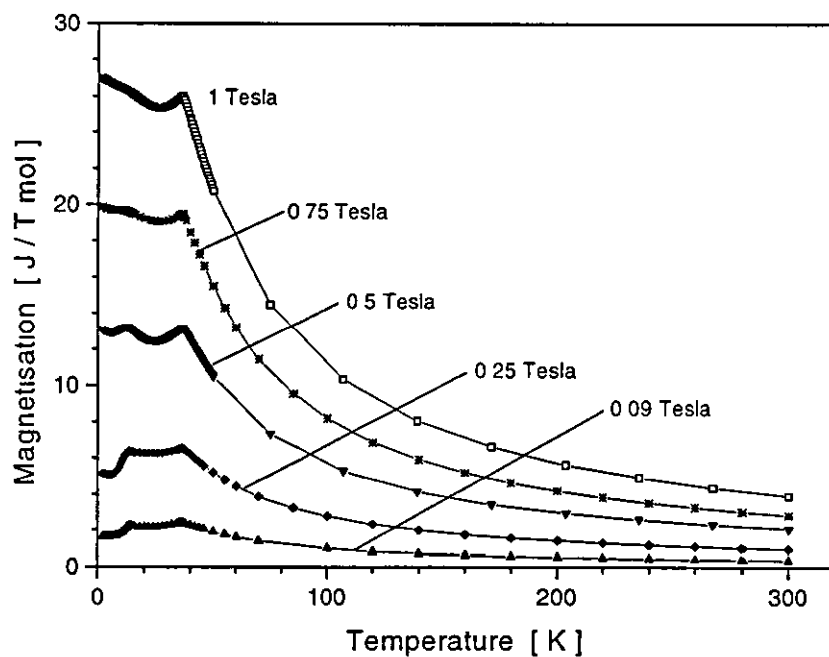
Figure 3 3 3. Molar magnetisation as a function of temperature at applied magnetic fields of 0 09, 0 25, 0 5, 0 75 and 1 Tesla for Gd₁₄Ag₅₁

53
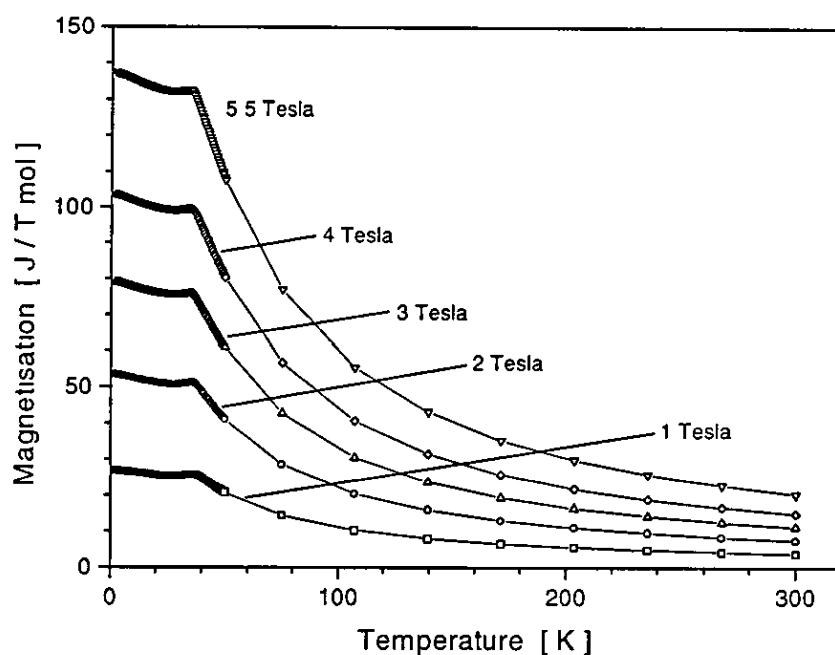
Figure 3 3 4 Molar magnetisation as a function of temperature at applied magnetic fields of 1, 2, 3, 4 and 5 5 Tesla for Gd₁₄Ag₅₁

These measurements reveal that $Gd_{14}Ag_{51}$ orders antiferromagnetically The figures clearly identify two phase transitions at 13 and 36 Kelvin in low applied fields. The first transition at 13 Kelvin disappears above an applied field of 1 Tesla and only the phase transition at 36 Kelvin remains. Also at approximately 1 Tesla the value of the measured magnetisation at zero temperature exceeds the value of the magnetisation at the phase transition In general the magnetisation increases with increasing magnetic field. However the magnetisation within the temperature interval of zero temperature to the second phase transition increases faster than the measured magnetisation above 36 Kelvin. In low applied fields (0 01 – 0.1 Tesla) the value of the zero temperature magnetisation is of the order of 2/3 of the maximum of the magnetisation as a function of temperature. This is expected for a simple model of an antiferromagnet as gives in section 3 1, equation [3 83] For higher magnetic fields the ratio of 2/3 is not obtained Further, the shape of the second phase transition changes and smoothes out with increasing field. This behaviour differs from the behaviour predicted for a simple antiferromagnet.

54

A further observation can be drawn from the figures. Changing the applied magnetic field both transition points are shifted in temperature. In figure 3.3.5 the transition temperatures are shown as a function of magnetic field
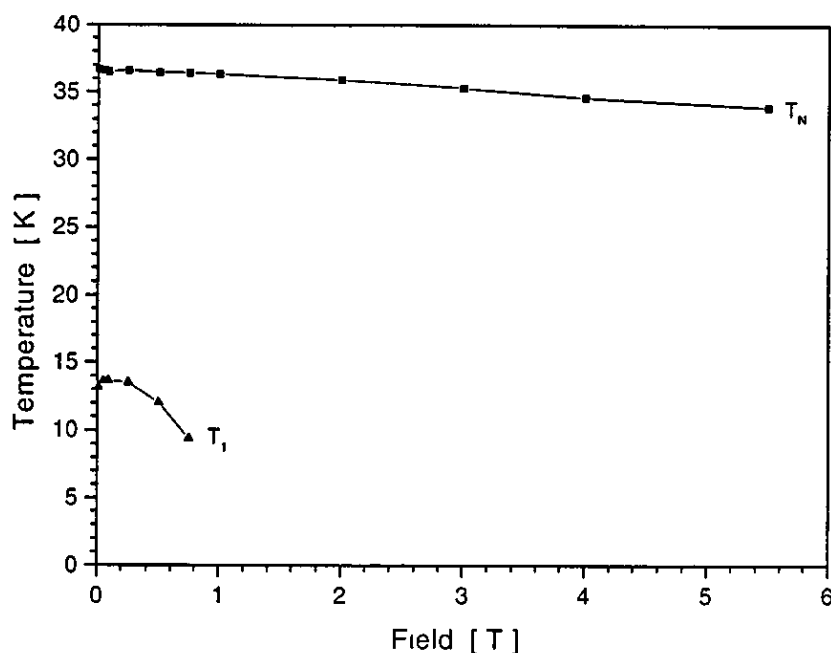
Figure 3 3 5 Transition temperatures as a function of magnetic field for Gd₁₄Ag₅₁ Tₙ is the Neél temperature at ~36 Kelvin in the absence of a field, Tᵢ is the temperature of the first transition at around 14 Kelvin for B = 0

From figure 3.3.5 it can be seen that the transition temperature T_N decreases with increasing field. The shift of the temperature T_1 with applied field is first of all upwards and then at higher values of B downwards. A more detailed analysis reveals (see figure 3.3 6) that the direction of the temperature shift of T_1 changes at a field of approximately 0 09 Tesla Also the field dependence of T_N changes slope at a field of ~0.09 Tesla.
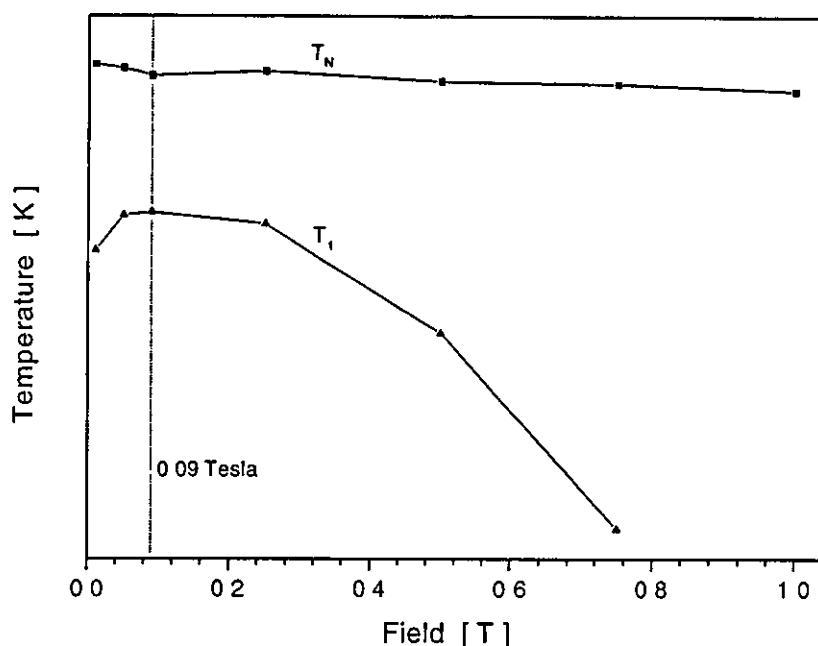
Figure 3 3 6   Transition temperatures as a function of magnetic field for $Gd_{14}Ag_{51}$ at low fields   The temperature axis of this plot is in arbitrary units

On symmetry grounds it is expected that the shift in the temperature of the antiferromagnetic phase transition is a function of the square of the applied magnetic field (see equation [3.112]). However, a linear dependence as a function of B^2 was not obtained. Assuming the dependence of the shift in the transition temperature T_{trans} as

$$T_{trans}(B) = T_0 - \alpha B^\beta, \qquad\qquad\qquad [3.113]$$

where T_0 is the transition temperature in the absence of an applied field and α, β are constants, a plot of $\ln(T_0 - T_{trans})$ versus $\ln(B)$ is expected to result in a straight line. The slope of these plots yields the exponent β and the intersection with the $\ln(T_0 - T_{trans})$ axis yields the value for $\ln(\alpha)$ The value for T_0 has been obtained by extrapolating the temperature shift of the transition temperature to zero-field. In figure 3.3.7 the plots are shown of the transition temperatures T_N and T_1. Only data points above 0 09 Tesla are considered for these two plots, because at this field the temperature shift changes and has a bend   Thus a

56

dependence of the transition temperatures as reported in equation [3.113] is only reasonable for fields higher than 0.09 Tesla.
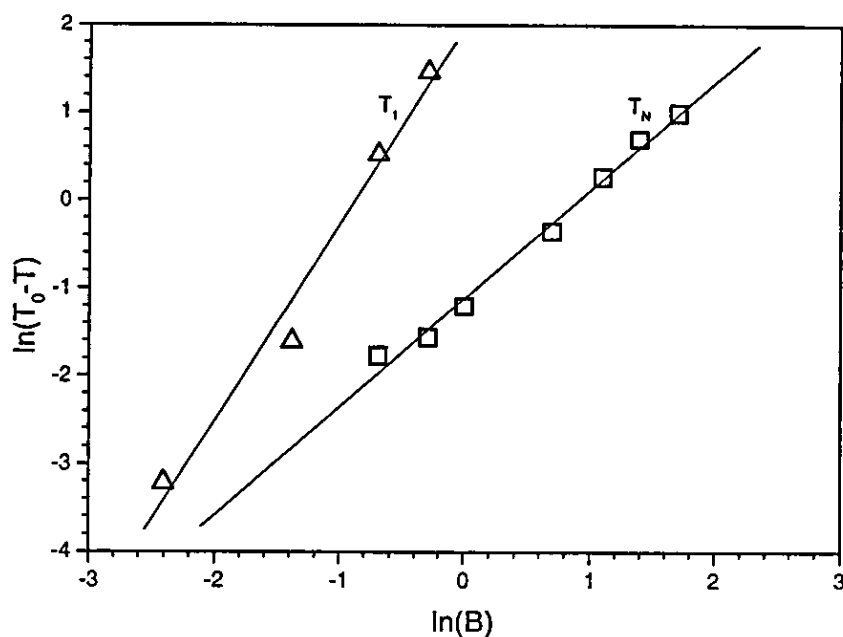
Figure 3 3 7   The temperature shift of T_N and T_1 plotted in a graph of $\ln(T_0 - T_{trans})$ *versus* $\ln(B)$ *for $Gd_{14}Ag_{51}$*

In figure 3.3.7 the plots of T_N and T_1 show acceptable straight lines. The values for β, α and T_0 have been obtained as

T_N : $\beta = 1.22 \pm 0\ 06$ $\alpha = 0.33 \pm 0.02$ $T_0 = 36.6 \pm 0.1$

T_1 : $\beta = 2.2 \pm 0.2$ $\alpha = 7 \pm 1$ $T_0 = 13.7 \pm 0\ 1$

The value for the exponent β of T_N is significantly different from 2 and the temperature shift in T_N is not a function of B^2. An exponent of 2 is found for T_1. This result is not expected, as the linear behaviour in B^2 was derived using only one antiferromagnetic and a field induced ferromagnetic phase. In order to account for this unusual result it is argued here that the expression for the free energy F (equation [3.96]) may have to be modified by the inclusion of a term $L \circ M$.

$$F = \frac{a}{2}M^2 + \frac{b}{2}L^2 + \frac{c}{4}L^4 + \frac{d}{2}L^2M^2 + e\,\mathbf{L}\circ\mathbf{M} - BM \qquad [3.114]$$

Such a term arises only if severe symmetry restrictions are satisfied. Unlike the contribution $\frac{d}{2}L^2M^2$ (which always occurs) the term $\mathbf{L}\circ\mathbf{M}$ is only possible for some cases. For the $RE_{14}Ag_{51}$ compounds such a term is possible and the solutions of the minimisation process acquire a more complicated form. The discussion of these symmetries and the free energy would exceed the framework of this thesis. However, it may be argued that because of $M \approx \chi B$ the order parameter M in the term $\mathbf{L}\circ\mathbf{M}$ is linearly coupled to the external field, and therefore an interaction term arises for which the order parameter L is proportional to the B field. Thus the antiferromagnetic component L and the shift in the transition temperature may acquire a contribution with a linear dependence on the field B.

With the values of β and α a phase diagram can be obtained for both transition temperatures. These diagrams are plotted in figure 3.3.8 and 3 3 9. Furthermore, using the parameter β and α the intersection point with the B axis in the phase diagram has been derived. At zero temperature the transitions should occur for applied fields of (46 ± 5) Tesla for T_N and $(1.3 \pm 0\ 2)$ Tesla for T_1

58
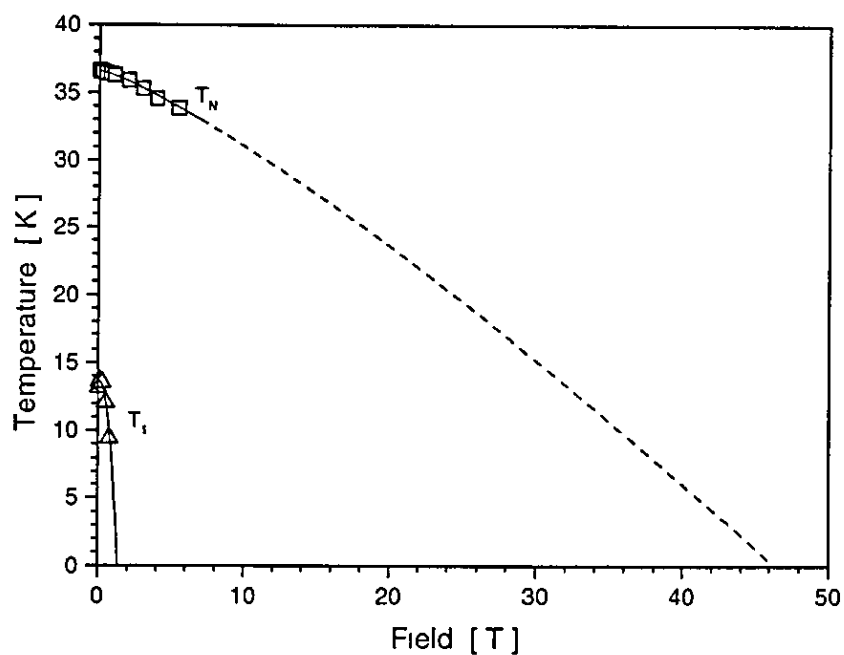
Figure 3 3 8 $Gd_{14}Ag_{51}$ phase diagram for the transition temperatures T_N and T_1 as a function of applied magnetic field The lines are obtained by a linear fit of $ln(T_0-T)$ versus $ln(B)$ and extrapolated to the intersections with the field axis
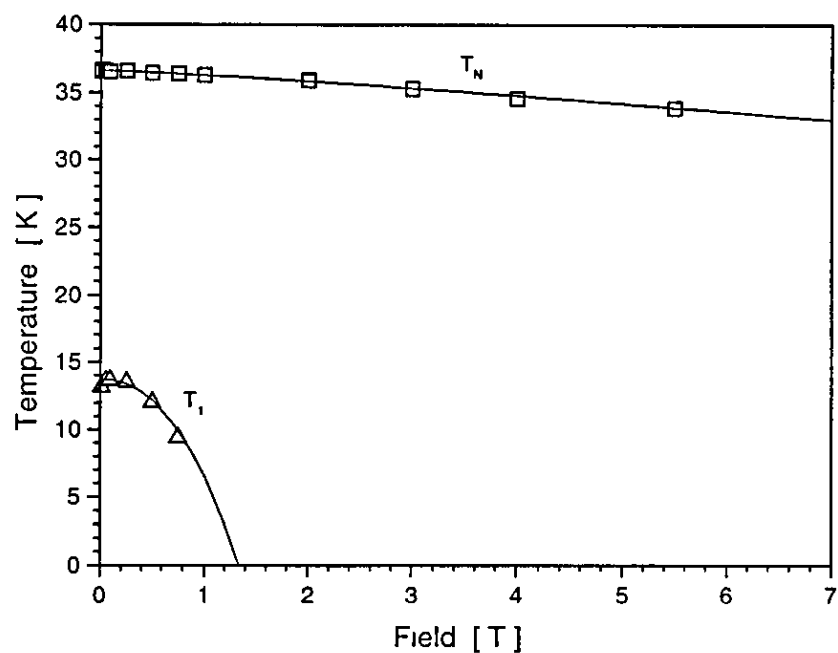
Figure 3 3 9 $Gd_{14}Ag_{51}$ phase diagram for the transition temperatures T_N and T_1 as a function of applied magnetic field

For temperatures above the second transition point of ~36 Kelvin the magnetisation versus temperature is in excellent agreement with the Curie Weiss law as shown in figure 3.3.10.
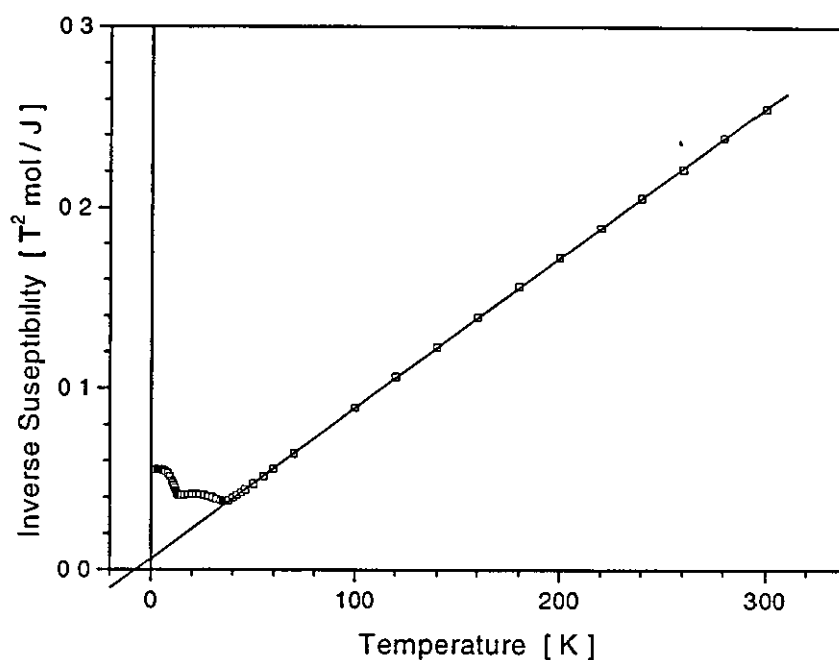
Figure 3 3 10 Inverse molar susceptibility as a function of temperature of Gg₁₄Ag₅₁
This graph is obtained from a data set where the magnetisation was measured as a
function of temperature in a field of 0 09 Tesla

Extrapolating the linear section above 36 Kelvin to its intersection point with the temperature axis yields a negative value for θ_N. A more detailed investigation of the paramagnetic phase will be discussed later with the help of Arrott plots

The magnetisation of the $Gd_{14}Ag_{51}$ was measured for various temperatures Some of the graphs are shown in figure 3.3.11. All the graphs indicate a linear dependence of the magnetisation on the applied magnetic field

60
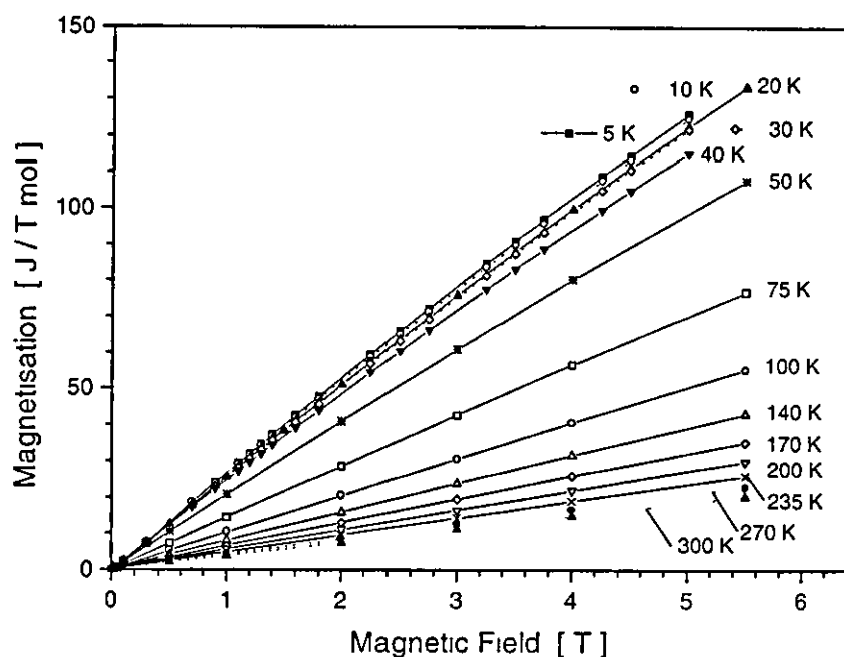
Figure 3 3 11   Molar magnetisation of Gd$_{14}$Ag$_{51}$ as a function of applied magnetic field at various temperatures

Arrott plots are more useful for investigating magnetic properties Using the data of the magnetisation measurements Arrott plots have been worked out for various isothermal measurements and the results are shown in figures 3 3 12 and 3 3.13.
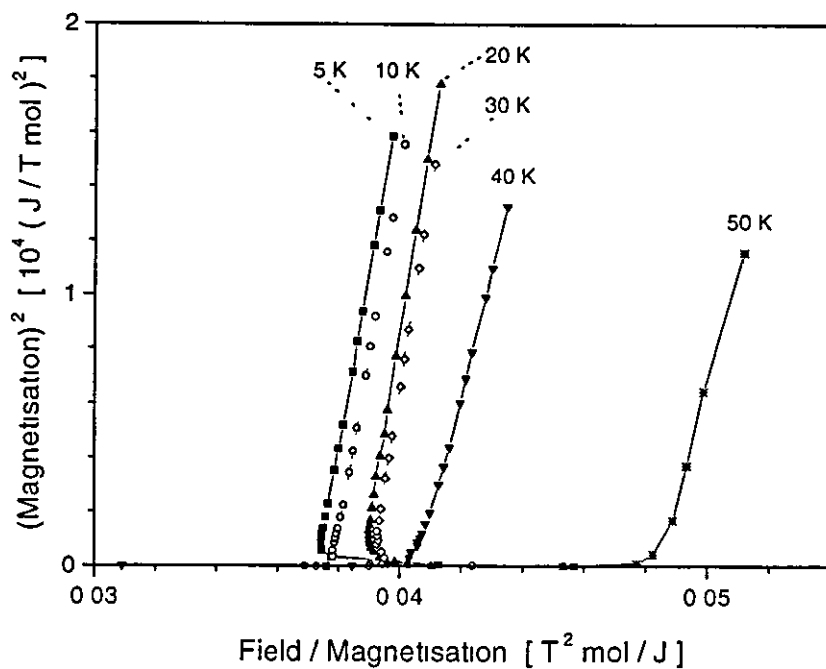
Figure 3 3 12. Arrott plots for $Gd_{14}Ag_{51}$
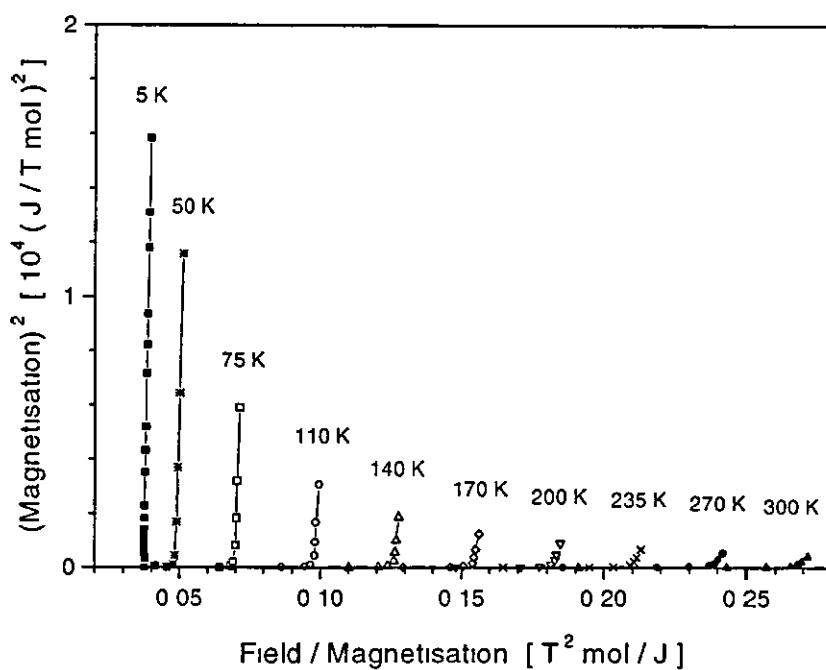
Figure 3 3 13 Arrott plots for $Gd_{14}Ag_{51}$

In figures 3.3.12 and 3.313 straight line sections can be clearly seen. For small values of the magnetisation the Arrott plots exhibit unusual curves which may be attributed to a small amount of an additional phase.

At temperatures above the transition temperature all Airott plots show the same linear behaviour. Linear lines have been fitted to these Arrott plots. The intersections with the x-axis (B/M-axis) yield values of the inverse susceptibility extrapolated to zero magnetic field. In figure 3 3.14 the inverse susceptibility is shown as a function of temperatuie.
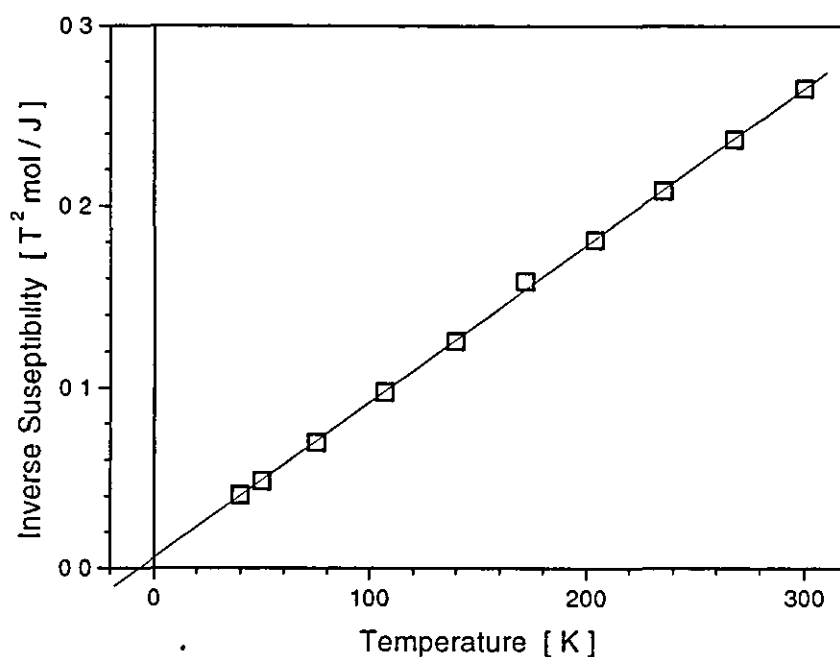
Figuie 3 3 14. Inverse Susceptibility of $Gd_{14}Ag_{51}$ as a function of temperatuie obtained from Airott plots The size of the data points indicate the error bar

In figure 3.3.14 the data points lie on a straight line. However, compared to figure 3.3.10 heie the values of the inverse susceptibility are obtained for zero field. An analysis of this plot has been carried out using a linear regression and a value for the molar Curie constant C_{mol} and the inteisection with the temperature axis was obtained. Further calculation yielded a value for the paramagnetic number of the Bohr magneton p_{eff} of 8.1 ± 0.1 and a paramagnetic Curie

temperature θ_N of $\theta_N = (-7 \pm 1)$ K. The theoretical value for p_{eff} (obtained by equation [3.34] using g = 2 and J = S = 7/2 for Gadolinium) is $p_{eff} = 7.94$ Experimental and theoretical values of p_{eff} are consistent.

The alloy $Tb_{14}Ag_{51}$

For the $Tb_{14}Ag_{51}$ sample magnetisation measurements have been carried out as a function of temperature over a range of 1.8 to 300 K. The curves obtained are shown in figures 3.3.15 to 3.3.19.
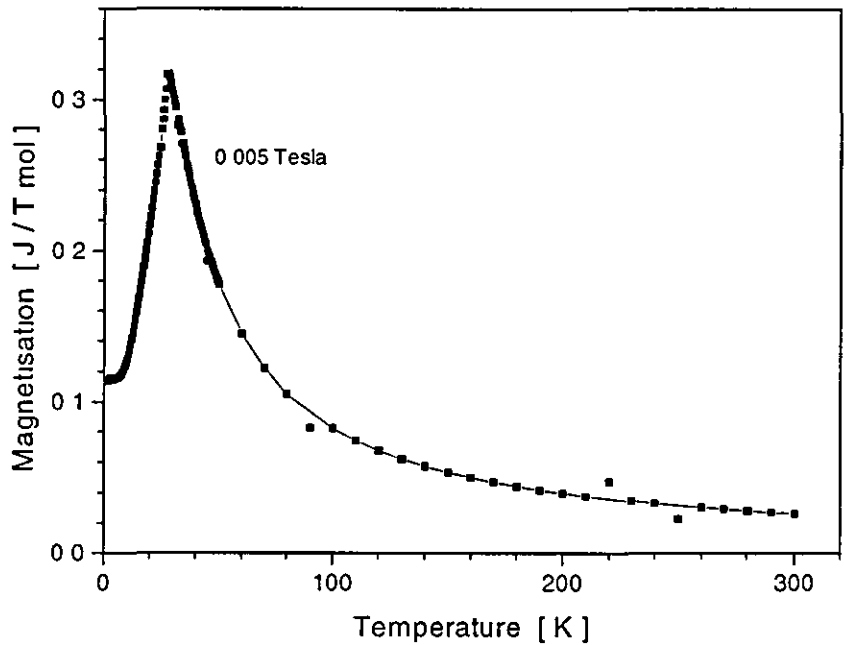
Figure 3 3 15 Molar magnetisation as a function of temperature at an applied magnetic field of 0 005 Tesla for $Tb_{14}Ag_{51}$

64
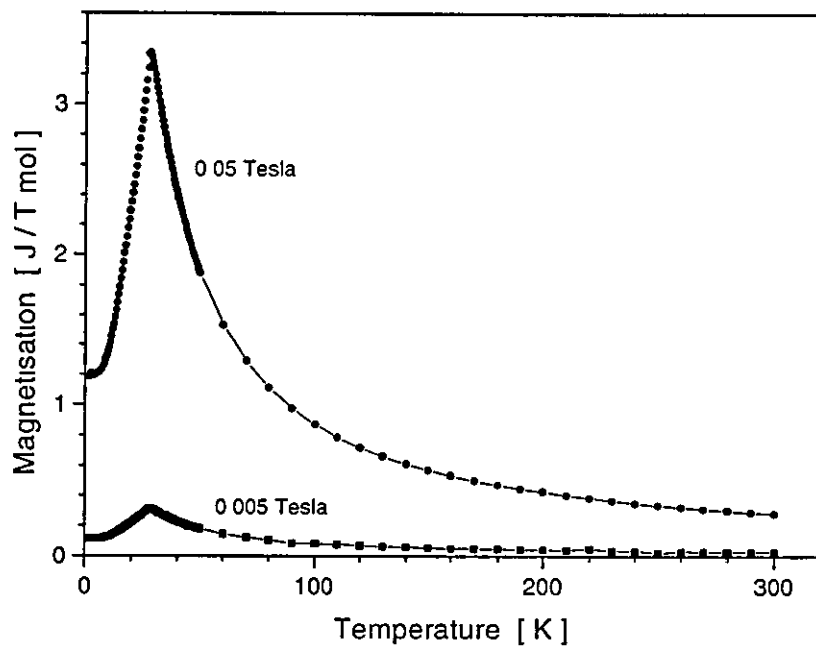
Figure 3 3 16 Molar magnetisation as a function of temperature an applied magnetic
fields of 0 005 and 0 05 Tesla for $Tb_{14}Ag_{51}$
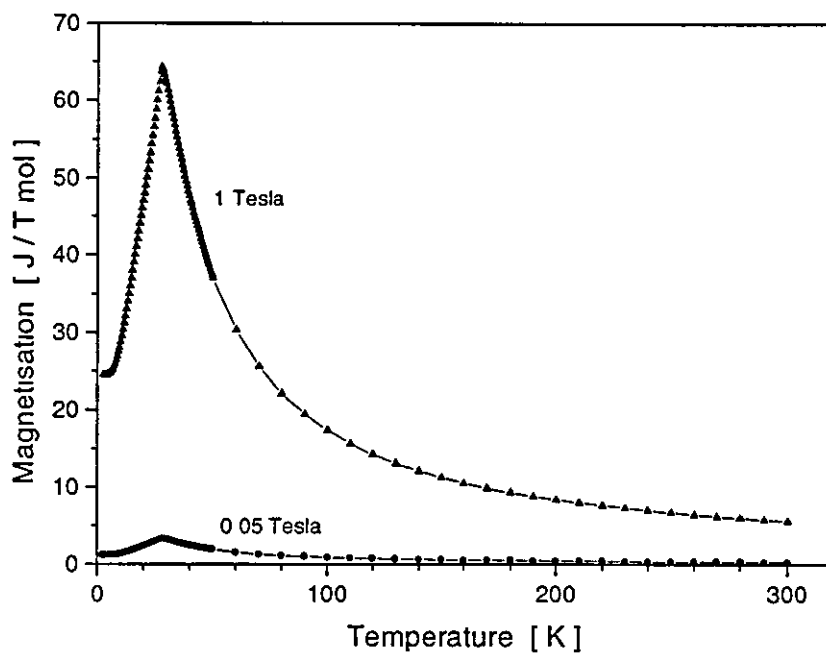
Figure 3 3 17 Molar magnetisation as a function of temperature an applied magnetic
fields of 0 05 and 1 Tesla for $Tb_{14}Ag_{51}$
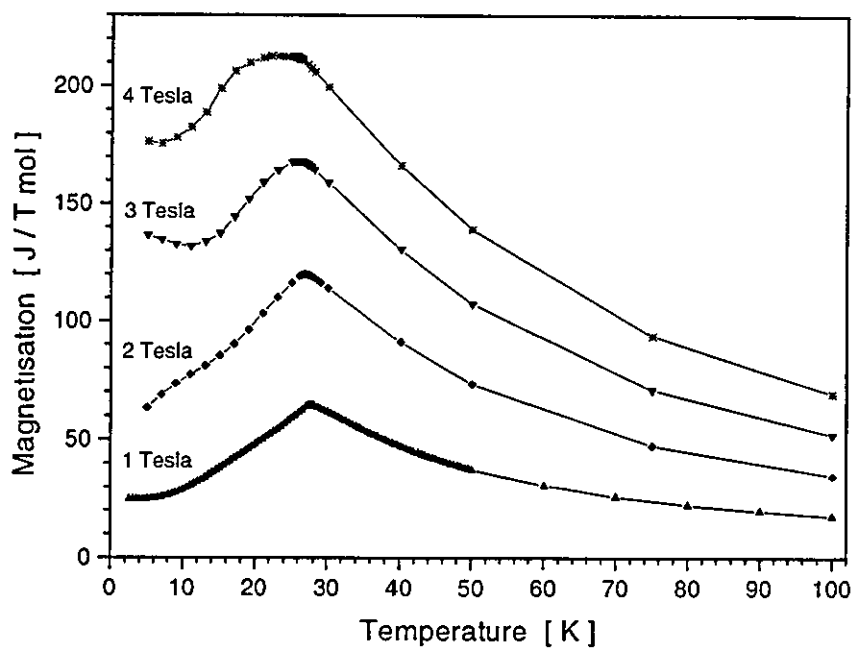
Figure 3 3 18 Molar magnetisation as a function of temperature an applied magnetic fields of 1, 2, 3 and 4 Tesla for $Tb_{14}Ag_{51}$
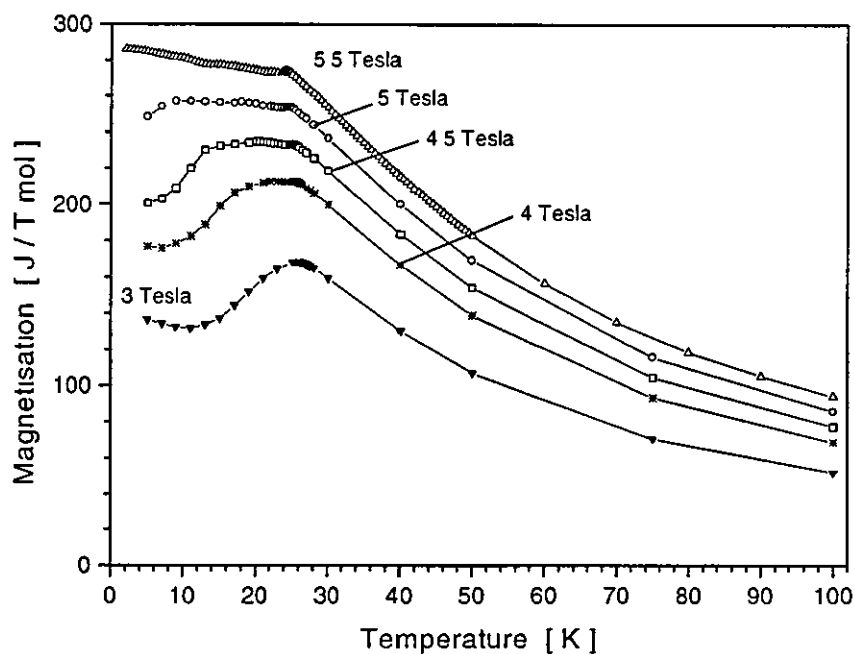
Figure 3 3 19 Molar magnetisation as a function of temperature at applied magnetic fields of 3, 4, 4 5, 5 and 5 5 Tesla for $Tb_{14}Ag_{51}$

All figures indicate an antiferromagnetically ordered phase with a transition at $T_N \approx 27$ K. Low field measurements qualitatively show the typical antiferromagnetic behaviour of a polycrystalline sample, as sketched in figure 3.1.5 in section 3.1. However the magnetisation at "zero temperature" is not equal to of 2/3 of the maximal magnetisation at the phase transition (see equation [3.83]). The value obtained is approximately 1/3 of the magnetisation at T_N and becomes larger with increasing fields. Above fields of 4 Tesla a second phase transition occurs at low temperatures. The temperature T_1 of this transition decreases strongly with increasing field from 23 to 15 Kelvin. By increasing the field from 0 005 to 5 5 Tesla the temperature T_N shifts from 28 down to 24 Kelvin. Both temperature shifts are shown in figure 3.3.20.
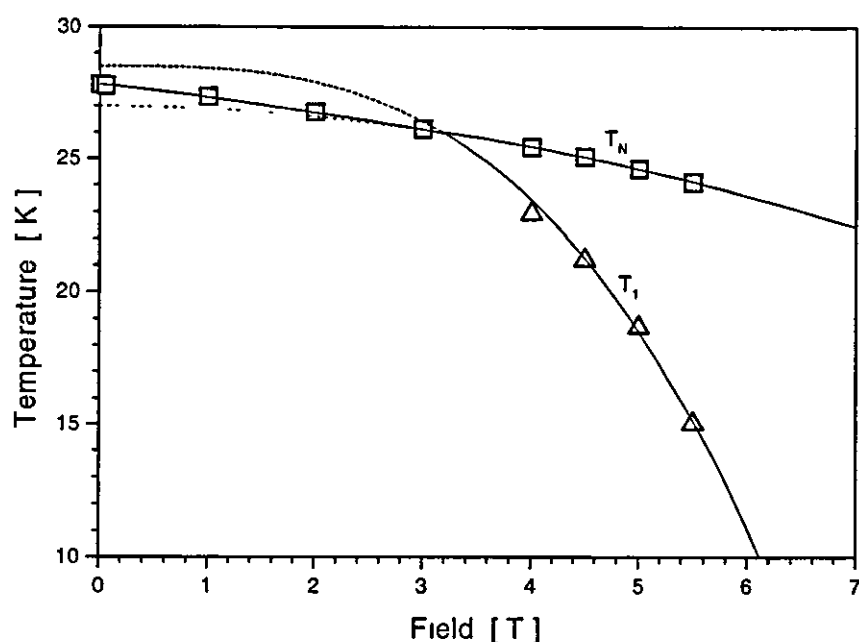
Figure 3.3 20· Phase diagram for the maximum temperatures of T_N and T_1 as a function of applied magnetic field for $Tb_{14}Ag_{51}$. The lines are obtained by a linear fit of $ln(T_0-T)$ versus $ln(B)$ and extrapolated to their intersections with the field axis The errors are represented by the size of the data points

At high fields both transitions are separated and the transition temperatures shift downwards with increasing field. At approximately 3 Tesla both transitions are merged together and only one transition remains. Below 3 Tesla the shape of the

transition is rather sharp. At 3 Tesla itself the shape becomes more smooth and at 4 Tesla both transitions are separated. In order to obtain the field dependence of each transition temperature $\ln(T_0 - T)$ was plotted against $\ln(B)$, where T_0 is the phase transition temperature in the absence of a field. The plots are shown in figure 3.3.21.
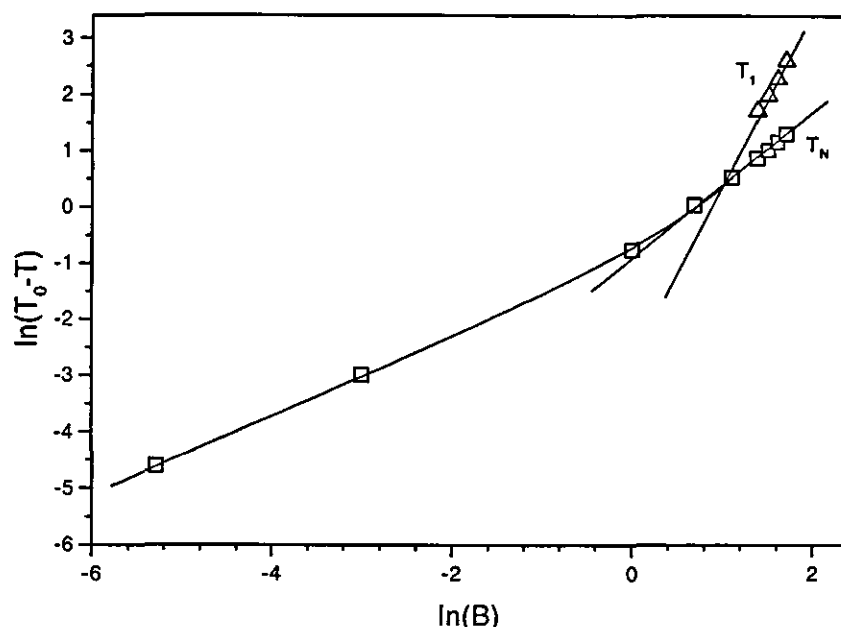

Figure 3 3 21 · Temperature shift of T_N and T_I plotted in a graph of $\ln(T_0 - T_{trans})$ versus $\ln(B)$ for $Tb_{14}Ag_{51}$

In figure 3.3.21 a linear behaviour for T_N and T_I above 3 Tesla can be seen. Below the intersection of T_N with T_I the data obtained does not exactly lie on a straight line. A linear fit on the obtained line above 3 Tesla was carried out and fit parameters β and α have been determined. (see equation [3.113]).

T_N : $\beta = 1.94 \pm 0.04$ $\alpha = 0\ 100 \pm 0\ 002$ $T_0 = 27.1 \pm 0.4$

T_I : $\beta = 3.1 \pm 0.2$ $\alpha = 0.070 \pm 0.007$ $T_0 = 28.5 \pm 0.2$

For T_N a β value close to 2 is obtained. This result reveals that for the $Tb_{14}Ag_{51}$ compound the Néel temperature is a function of B^2. This is in excellent

68

agreement with theory as predicted by equation [3.112] in section 3.1. The field induced shift of the transition temperature T_1 has a B^3 behaviour. Below 3 Tesla the transition temperature decreases approximately linearly with field. Using the parameter β and α a phase diagram has been constructed and it is shown in figure 3.3.20 Finally for both transitions the critical fields at zero temperature were determined as 17.5 ± 0 4 for the T_N and 7.0 ± 0.1 for T_1.

Above T_N $Tb_{14}Ag_{51}$ shows paramagnetic behaviour and the magnetisation decreases with increasing applied field. In order to analyse the paramagnetic phase magnetisation measurements have been carried out as a function of applied field and at various temperatures in a range of 1 8 K to 300 K Arrott plots have been constructed. In figures 3.3.22 and 3.3.23 some measurements of magnetisation against field are shown
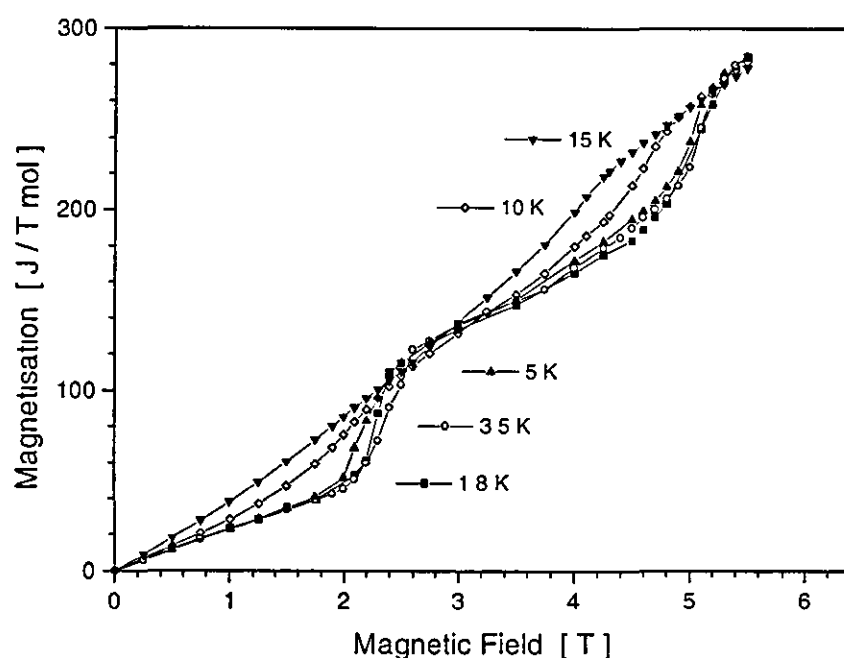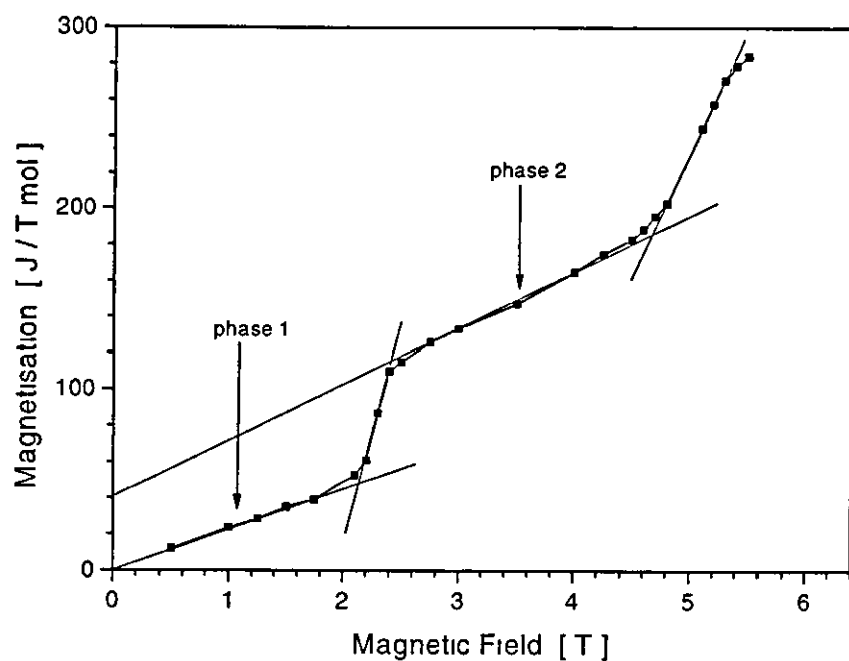

Figure 3 3 22: Molar magnetisation as a function of magnetic field for $Tb_{14}Ag_{51}$
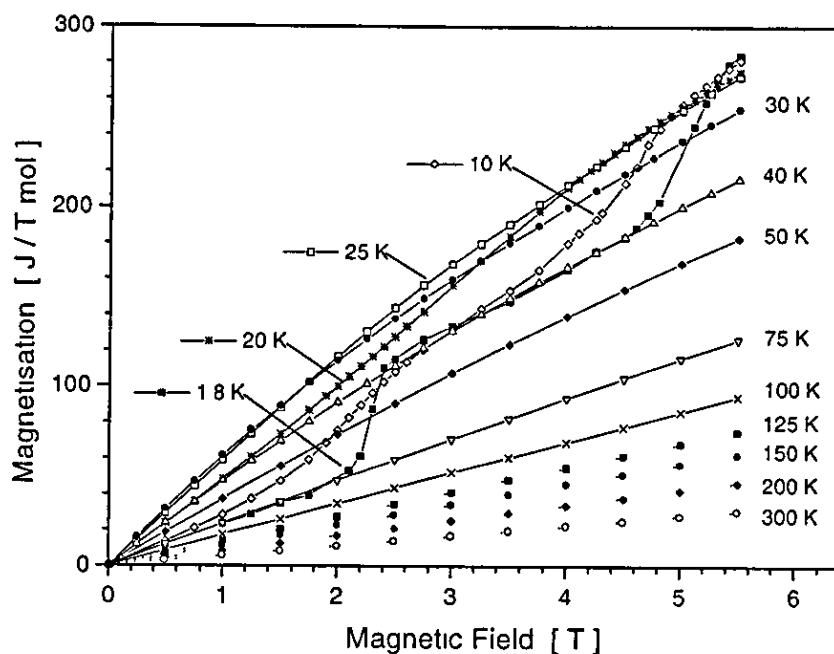
Figure 3 3 23   Molar magnetisation as a function of magnetic field for Tb₁₄Ag₅₁

Above 15 Kelvin the isotherms are smooth curves and at higher temperatures the graphs become straight lines. Below 15 Kelvin the graphs have a step structure. In figure 3 2.24 the measurement at 1.8 Kelvin is plotted to show this "step-behaviour" more clearly. At zero field the magnetisation is zero, as expected for an antiferromagnet. The magnetisation increases linearly with field up to fields of approximately 2 Tesla. Then the magnetisation increases more rapidly and above 2.4 Tesla it reaches another linear regime   Above 4 6 Tesla the magnetisation increases more rapidly indicating the onset of another step at 5.5 Tesla. At 3 5 Kelvin a magnetisation measurement was carried out for which the magnetic field was increased from –5 5 to 5.5 Tesla and thereafter again decreased to –5.5 Tesla. The magnetisation is plotted in figure 3 3.25.

Figure 3 3 24· Molar magnetisation as a function of magnetic field at 1 8 Kelvin for
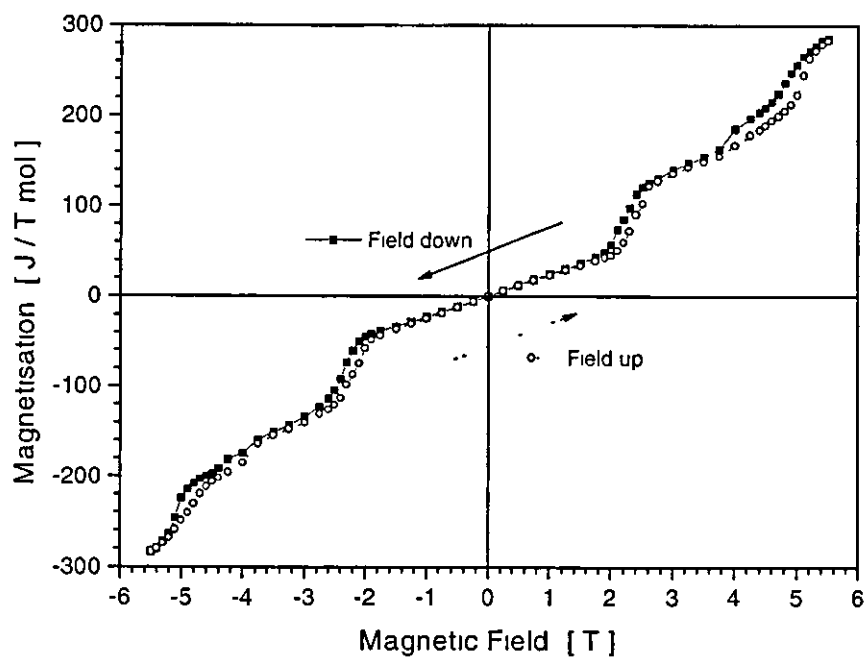*Tb₁₄Ag₅₁*

Figure 3 3 25 Molar magnetisation as a function of magnetic field up and down at 3 5
Kelvin for Tb₁₄Ag₅₁

71

As pointed out above from figure 3.3.25 it can be seen that small hysteresis loops appear at the transition between the linear levels and that the same step behaviour occurs at negative magnetic fields. Therefore, it can be inferred that with increasing magnetic field $Tb_{14}Ag_{51}$ switches between different antiferromagnetic phases. The various phases differ by a shift in the linear levels of the magnetisation as obtained by extrapolating the linear part back to the y-axis.

In order to identify the microscopic origin of this behaviour neutron scattering experiments will be required. At present these are not available It therefore only remains to point out that an increase in the external magnetic field stabilises different magnetic structures at low temperatures.

From the magnetisation measurements it can be seen that in the absence of a field the magnetisation is zero. That indicates antiferromanetically ordered magnetic moment. After the first field induced phase transition the magnetisation has a linear field dependence, which can be extrapolated to an intersection with the magnetisation axis as plotted in figure 3.3.24. This intersection point yields a moment of approximately 40 J/Tmol. One unit cell of the rare earth compounds contains 14 rare earth atoms, all of which have a magnetic moment. If some of these moments were to be fully align by an external field the total magnetic moment per aligned rare-earth atom of one unit cell is then given by $g J \mu_B N_A$, where g is the Landé factor, J the total angular momentum, μ_B the Bohr magneton, and N_A Avogadro's constant. For Terbium the molar magnetic moment is 50.26 J/Tmol. Considering that other influences may reduce the size of the magnetic moment (for example crystal field effects) the experimentally observed value of 40 J/Tmol is in fair agreement with the theoretical value of one aligned moment per unit cell. Thus it may be argued that the first field induced phase corresponds to an antiferromagnetic state where one magnetic moment (Tb-atom) is fully align by the applied field. From figure 3.3.22 it can be inferred that the phase transitions have only a weak temperature dependence and disappear above 10 Kelvin. The disappearance may be attributed to the fact that the energy difference $\Delta M B$ between the magnetic states is of the same
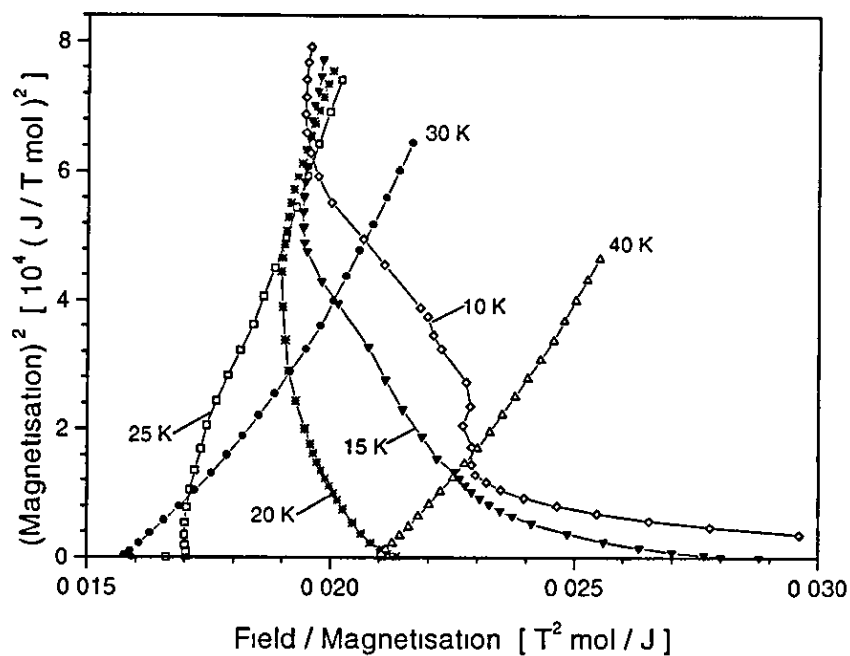
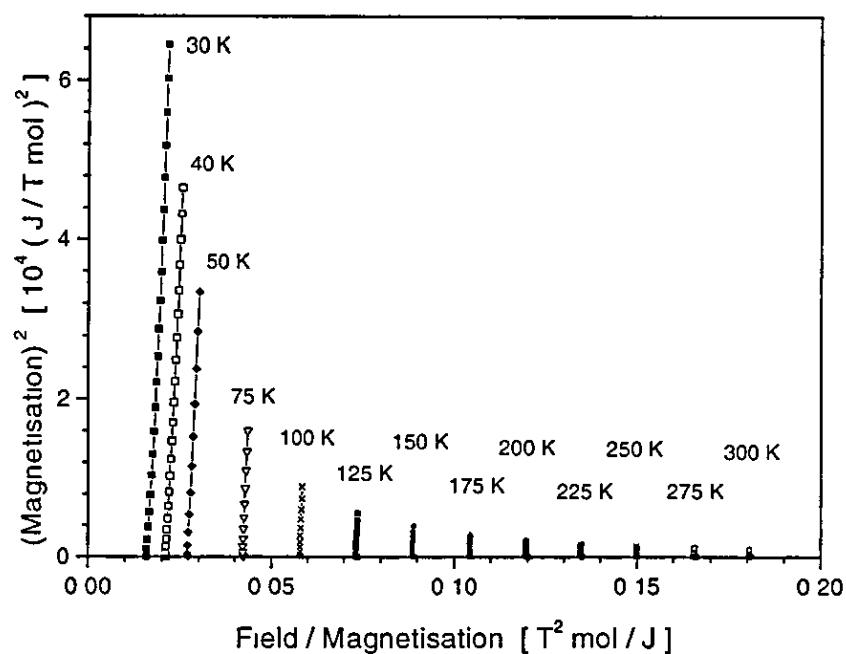*Figure 3 3 27 Arrott plots of Tb₁₄Ag₅₁ for low temperatures*

Figure 3 3 28 Arrott plots of Tb₁₄Ag₅₁ for high temperatures

Above the Néel temperature the isotherms are smooth graphs and nearly linear.
Below 27 K the Arrott plots show a more varied behaviour.

74

As discussed in connection with the analysis of $Gd_{14}Ag_{51}$, Arrott plots are used to obtain values for the magnetic susceptibility by fitting linear lines to the isotherms. The temperature dependence of the inverse susceptibility is plotted in figure 3.3 29.
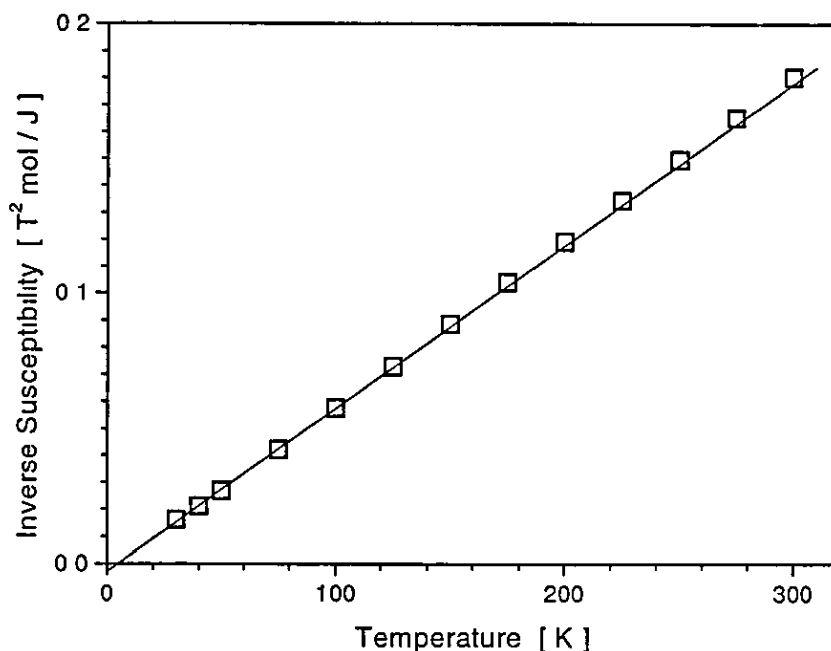
Figure 3 3 29 Inverse susceptibility as a function of temperature for $Tb_{14}Ag_{51}$ obtained by using Arrott plots The size of the data points indicates the error bar

The data in figure 3.3.29 is in good agreement with the model of a Curie–Weiss law. A linear fit, indicated by a straight line, yields a Curie constant C_{mol} [3.69] and a paramagnetic Curie temperature θ_N [3 71] Using equation [3.70] the effective paramagnetic Bohr magneton number p_{eff} can be calculated from C_{mol}

For $Tb_{14}Ag_{51}$ a value of 9 9 ± 0.3 for p_{eff} and (1.2 ± 1) K for θ_N is obtained

The theoretical value for p_{eff} is 9.7. Both values agree to within the error bar. However the experimental value is found to be slightly larger (0.02) than the theoretical one. This is similar to the $Gd_{14}Ag_{51}$ alloy. The value for the paramagnetic Curie temperature θ_N is obtained as a small positive number.

The alloy $Dy_{14}Ag_{51}$ *

A small piece of $Dy_{14}Ag_{51}$ has been measured using the SQUID magnetometer The magnetisation as a function of temperature is plotted in the figures 3.3 30 – 3 3 33 for various strengths of the applied magnetic field The measurements have been carried out within a temperature range of 1.8 to 300 K and for fields between 0 and 5.5 Tesla To enable the regions of interest to be seen more clearly at low temperatures the data in figure 3 3 32 and 3 3 33 are shown only in the range of 1.8 to 100 K
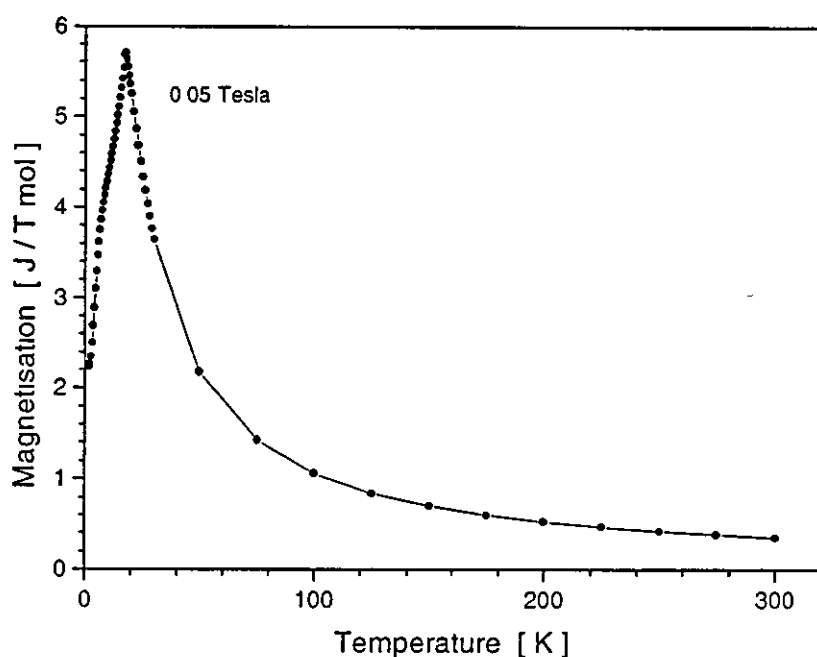
Figure 3 3 30 Magnetisation for $Dy_{14}Ag_{51}$ as a function of temperature for an applied field of 0 05 Tesla
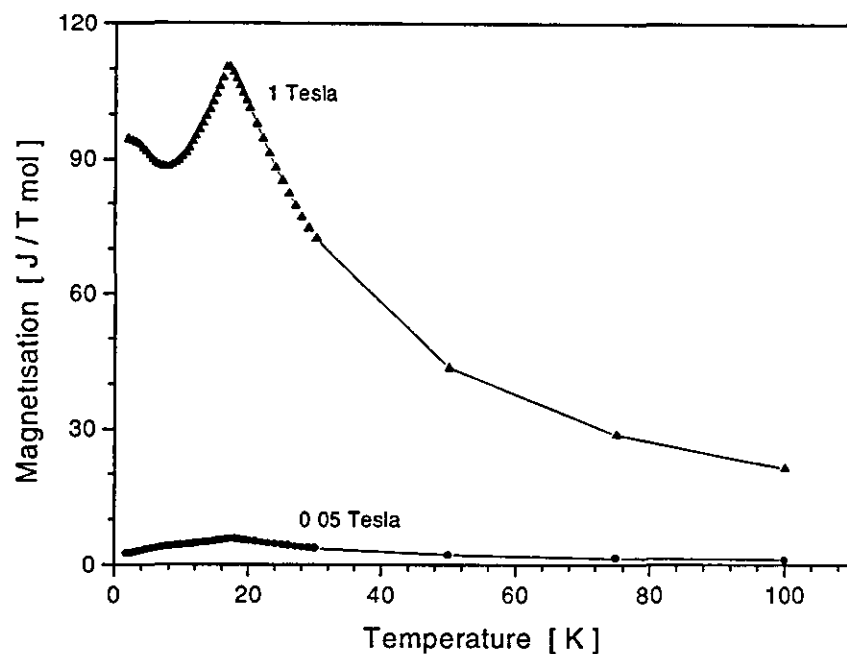
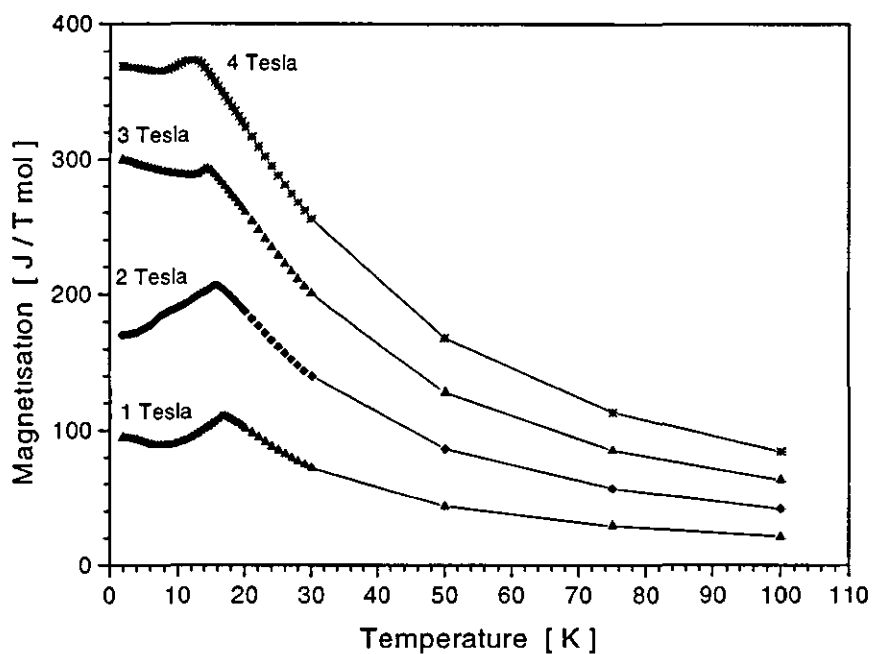*Figure 3 3 31: Magnetisation for $Dy_{14}Ag_{51}$ as a function of temperature*

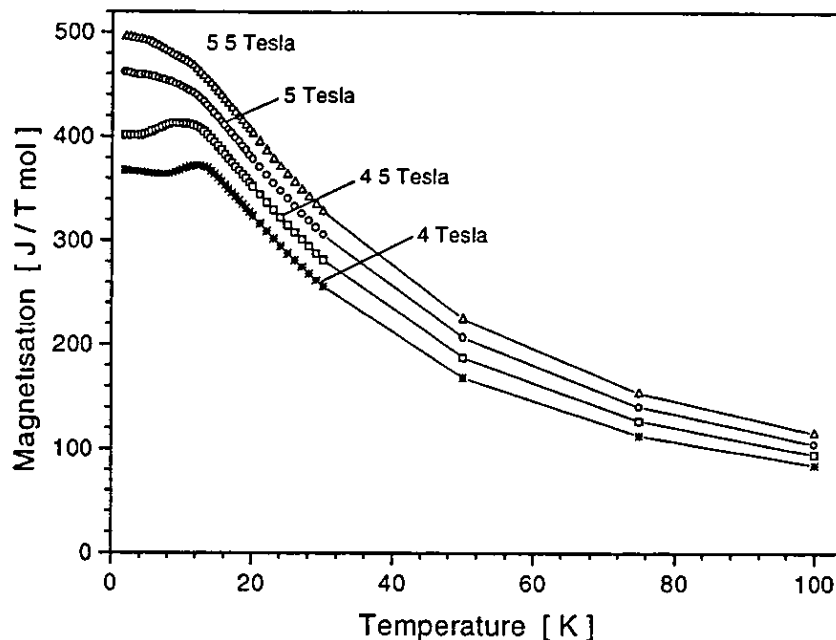*Figure 3 3 32. Magnetisation for $Dy_{14}Ag_{51}$ as a function of temperature*

Figure 3 3 33   Magnetisation for $Dy_{14}Ag_{51}$ as a function of temperature

For low applied fields one clearly observes an antiferromagnetic phase transition at ~17 K. In a field of 0 05 Tesla the magnetisation increases with increasing temperature starting at a value of ~2.2 J/Tmol to a maximum with a value of ~5 7 J/Tmol at the phase transition. At ~7.5 Kelvin a small bump appears in the magnetisation. However, this bump can not be identified as a transition point. At 1 Tesla the magnetisation first decreases to a minimum at ~7 K and then rises to a maximum located at the phase transition temperature of ~16.7 K In the 2 Tesla measurement the low temperature magnetisation generally increases with increasing temperature up to the (shifted) antiferromagnetic phase transition Above 2 Tesla the plots of the magnetisation show the same continual increasing behaviour as reported for the measurement at 1 Tesla

Up to 4 Tesla the phase transitions takes the form of a sharp peak This peak becomes broader at 4 Tesla and a second phase transition reveals itself above 4 Tesla. At higher fields the shape of the transitions become very broad However, the transitions are still discernible. As for $Gd_{14}Ag_{51}$ and $Tb_{14}Ag_{51}$ the transition temperatures T_1 and T_N shift with increasing field. The shift in the

78

transition temperatures as a function of field is shown in figure 3.3.35. In this figure a merger of the transition temperature T_1 and T_N can be seen at 4 Tesla.

In order to investigate the power law dependence of the temperature shift on the applied field a logarithmic plot is shown in figure 3.3.34 of $\ln(T_0 - T)$ versus $\ln(B)$
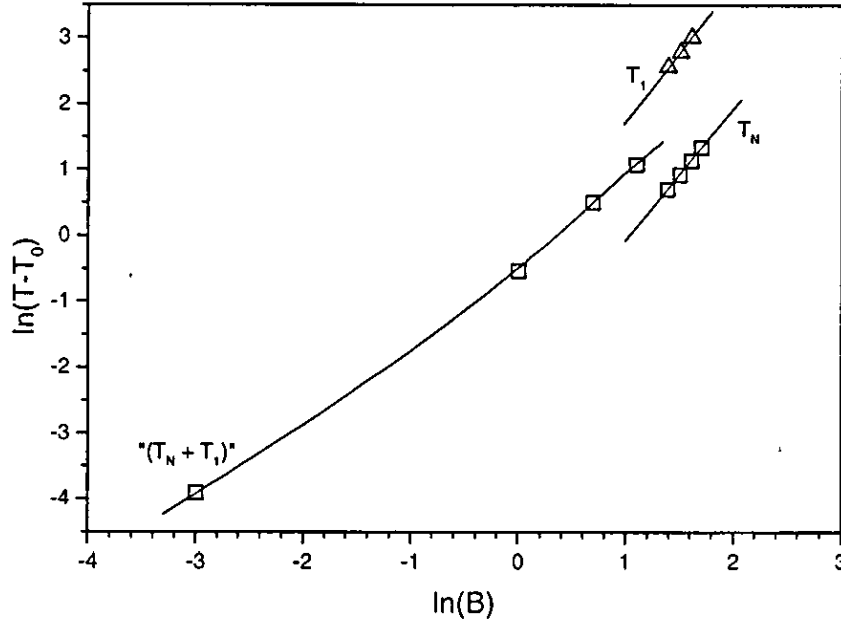

Figure 3.3 34   Logarithmic plot of characteristic temperatures to $Db_{14}Ag_{51}$

Similar to $Tb_{14}Ag_{51}$ three different graphs are obtained. The data points, belonging to T_1 lie on a straight line, as do the data points (above 4 Tesla) belonging to the temperature T_N. The data points (T_N) below 4 Tesla from a curve, which is close to a line. The various plots at figure 3.3 34 were fitted using $\ln(T_0 - T) = \ln(\alpha) + \beta \ln(B)$ resulting in

T_N: $\beta = 1.99 \pm 0.04$ $\alpha = 0.129 \pm 0 003$ $T_0 = 14\ 8 \pm 0.4$

T_1 $\beta = 1.99 \pm 0 07$ $\alpha = 0\ 83 \pm 0 04$ $T_0 = 25\ 0 \pm 0.7$

Thus T_N and T_1 the field dependence is obtained by $T = T_0 - \alpha B^2$ which is in perfect agreement with theory.

79

In the phase diagram the intersection of the phase transition with the magnetic field axis determines the value of magnetic field for which the magnetic phase transition is suppressed at zero temperature. At zero temperature the transition at T_1 occurs for a field of (5.56 ± 0.04) Tesla, while the transition at T_N is extrapolated to occur at a field of (10.9 ± 0.2) Tesla.
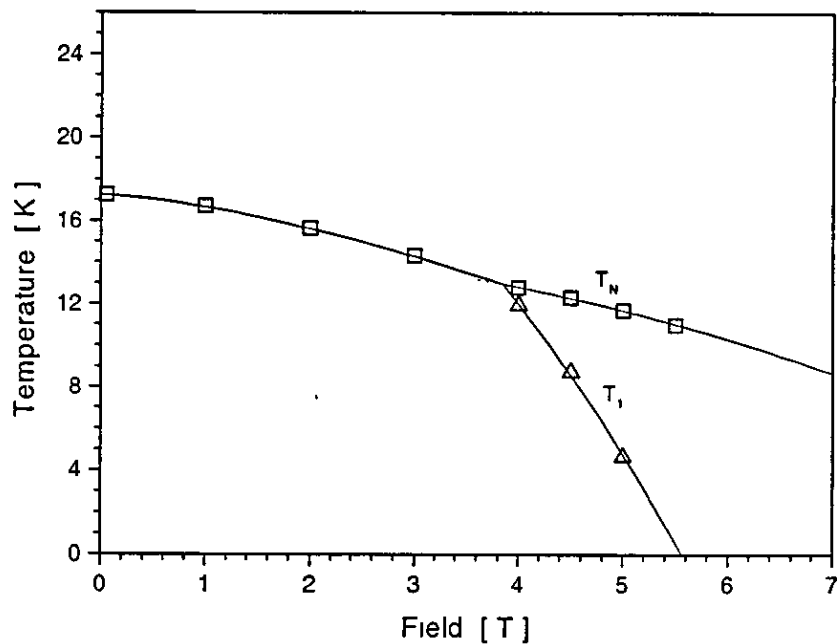

Figure 3 3 35 Temperature shift of T_N and T_1 as a function of field for $Tb_{14}Ag_{51}$

The magnetisation measurements as a function of magnetic field are shown in figure 3.3.36 and 3.3.37 for various temperatures ranging from 1.8 to 300 K.
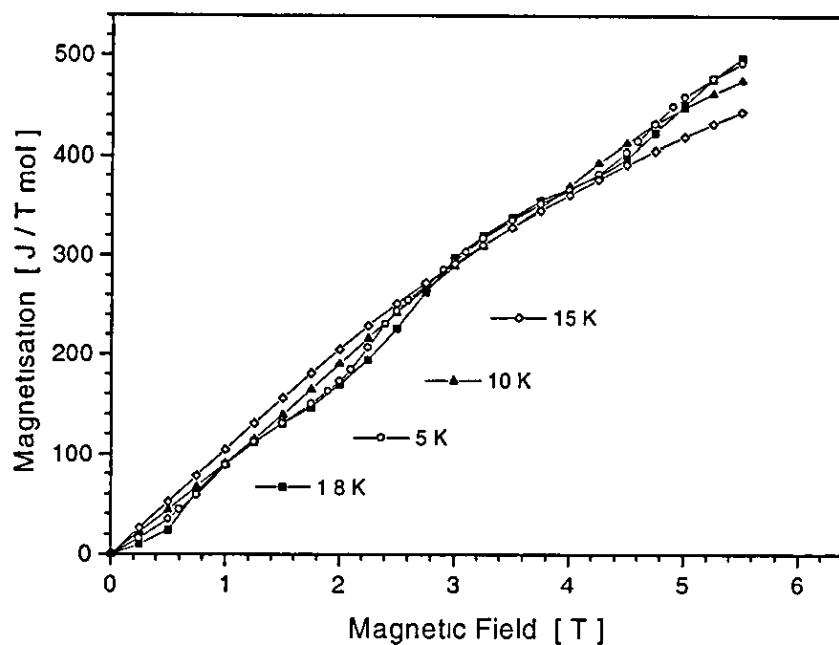
Figure 3 3 36 Magnetisation of Dy$_{14}$Ag$_{51}$ as a function of applied magnetic field for various temperatures
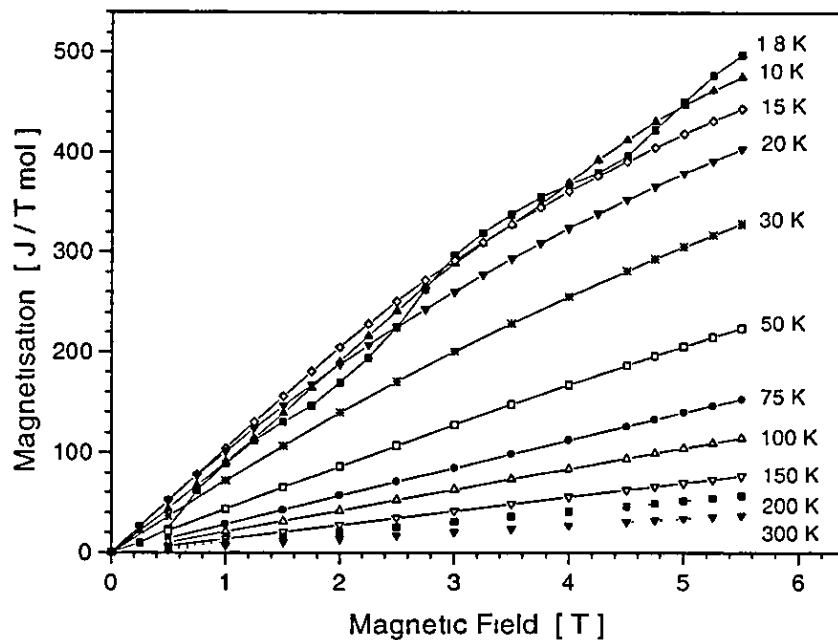

Figure 3 3 37. Magnetisation of Dy$_{14}$Ag$_{51}$ as a function of applied magnetic field for various temperatures

81

For the magnetisation measurements at 1.8 and 5 Kelvin a step structure is obtained as a function of increasing field. A hysteresis measurement at 1.8 indicates small hysteresis loops in the magnetisation "steps" as shown in figure 3.3.38.
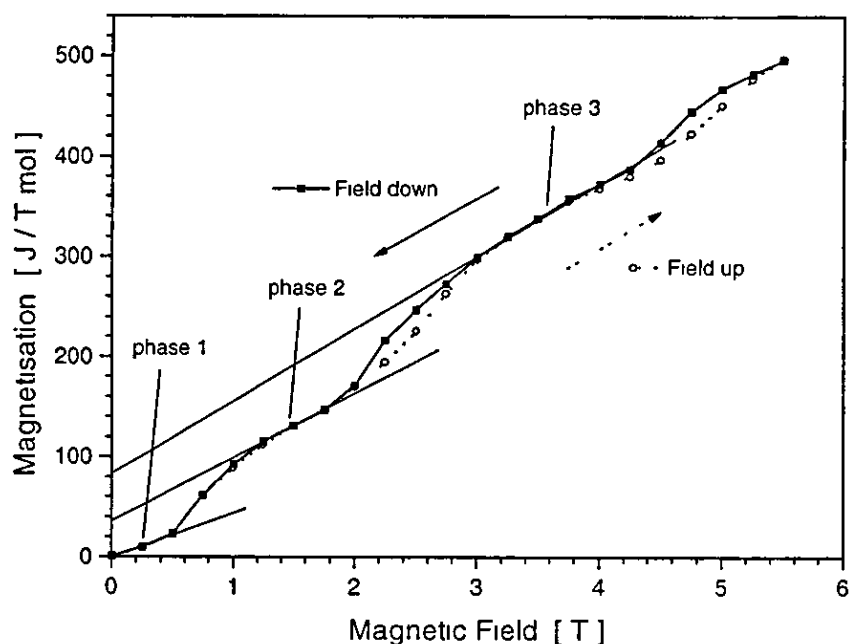

Figure 3 3 38. Magnetisation for Dy₁₄Ag₅₁ as a function of increasing and decreasing magnetic field (5 5 → 0 → 5 5 Tesla) at T = 1 8 K.

In figure 3.3.38 three magnetic phase transitions are observed at a temperature of 1 8 K and within a magnetic field range of 0 to 5 5 Tesla. The transitions occurs at ~0.75, ~2.42, and ~4.85 Tesla and each step exhibits a small hysteresis loop Between these transitions different magnetic phases can be identified. These phases are characterised by a linear magnetic field dependence of the magnetisation. The static (i. e. zero-field) magnetisation is obtained by extrapolating the straight part to the intersection with the magnetisation axis This is indicated in the figure 3.3.38 by straight lines The magnetisation values are obtained as ~40 J/Tmol for phase 2 and ~80 J/Tmol for phase 3 These values may be compared to the value obtained for the second phase of the Tb₁₄Ag₅₁ compound of ~40 J/Tmol The magnetisation values of the second phase of Dy₁₄Ag₅₁ and Tb₁₄Ag₅₁ are in a excellent agreement. The value of the

82

intersection with the y-axis obtained for phase 3 of the $Dy_{14}Ag_{51}$ compound is twice as big compared to the value of phase 2 Thus, considering the theoretical values of 50.26 J/Tmol for Terbium and 55 84 J/Tmol for Dysprosium, it may be argued that phase 2 is characterised by the full alignment of the magnetic moment of one rare earth atom by the external magnetic field and phase 3 is characterised by the alignment of two rare earth moments per unit cell.

For the measurement of the magnetisation at T = 5 K the three field induced transitions occur at slightly higher fields of ~0 75, ~2 4, and ~4.75 Tesla. Therefore the field induced phase transitions are temperature dependent Above a temperature of ~10 Kelvin the "step shape" of the magnetisation diminishes and finally disappears. It may argued that above 10 Kelvin the thermal energy ($k_B T$) is sufficient to have all different magnetic arrangements equally excited. All observed phase transitions and their temperature dependencies are illustrated in the phase diagram shown in figure 3.3 39.
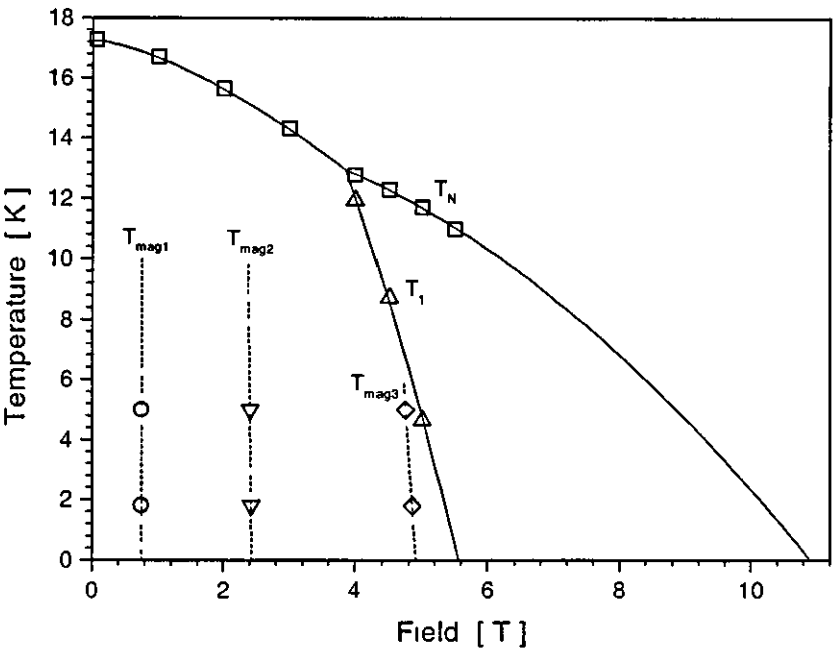

Figure 3 3 39   Low temperature magnetic phase diagram of $Dy_{14}Ag_{51}$

In figure 3.3.40 and 3.3 41 Arrott plots are shown of $Dy_{14}Ag_{51}$, obtained by using isothermal magnetisation measurements as a function of field.
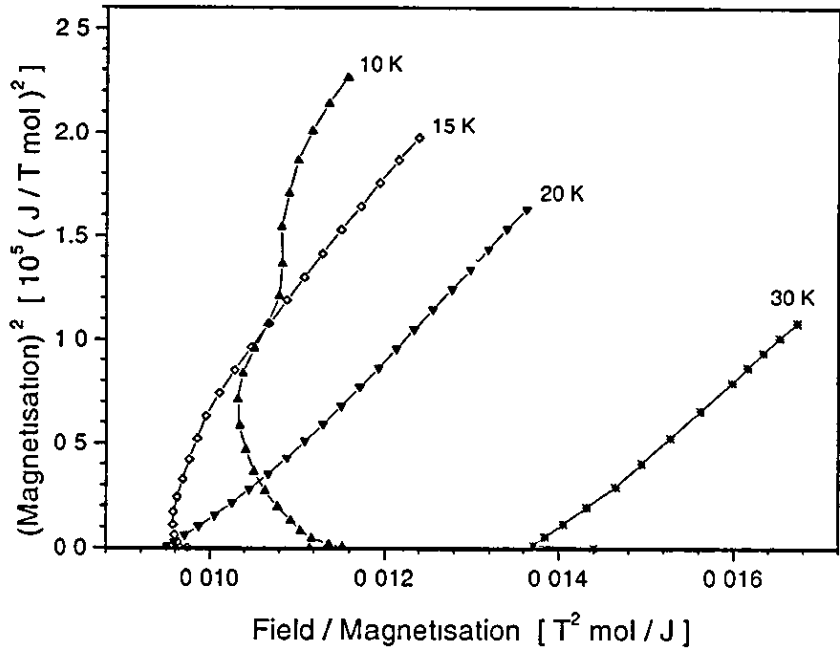

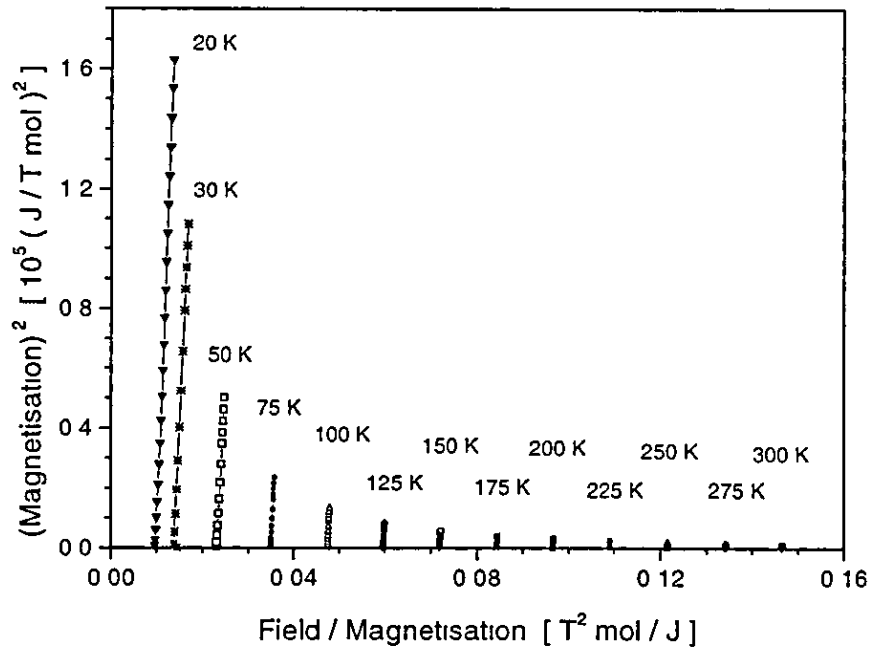Figure 3 3 40   Arrott plots of $Dy_{14}Ag_{51}$ for various temperatures (low temperatures)

Figure 3 3 41.   Arrott plots of $Dy_{14}Ag_{51}$ for various temperatures (high temperatures)

Above the transition at ~17 Kelvin the Arrott plots are given by straight lines Fitting yields values of the inverse susceptibility at various temperatures as given by the intersection with the x–axis (B/M–axis). In figure 3.3.42 the values of the inverse susceptibility are plotted as a function of temperature With the exception of the point at 300 K all other points are well described by a straight line indicating a Curie Weiss behaviour in the paramagnetic region. The intersection with the temperature axis occurs for θ_N = (– 0.4 ± 0.5) K. The slope of the line (excluding the 300 K data point) yields the molar Curie constant C_m. This in turn enables the value of p_{eff} to be calculated with p_{eff} = 10 9 ± 0.3. The theoretical value using J = 15/2, g = 4/3, and considering 14 Dysprosium atoms per unit cell yields a Bohr magneton number of 10 6. This agrees, to within the experimental error, with the experimental value.
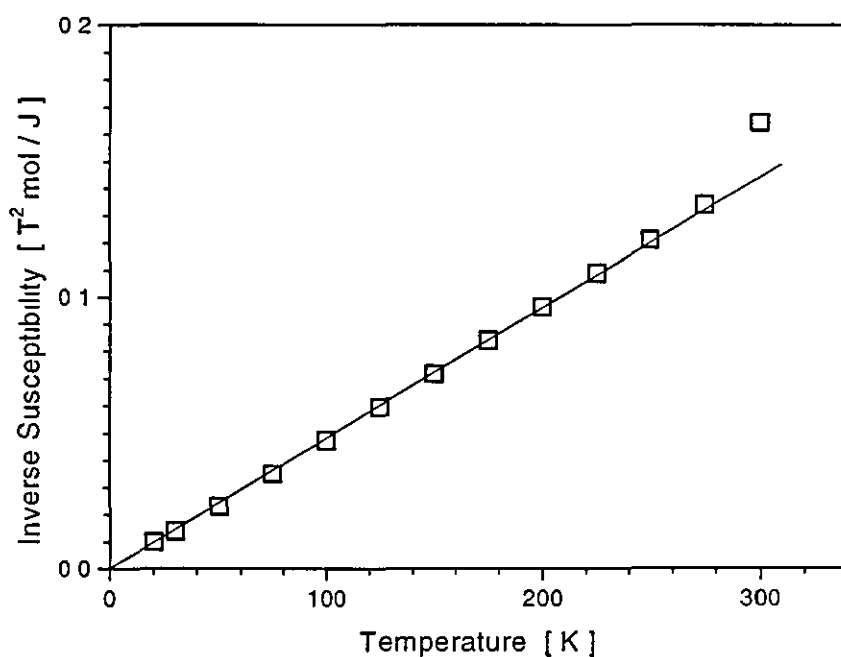

Figure 3 3 42 Inverse susceptibility of $Dy_{14}Ag_{51}$ as a function of temperature as obtained from Arrott plots

The magnetisation of Ho$_{14}$Ag$_{51}$ has been measured as a function of temperature and applied magnetic field. Plots of constant field measurements are shown in figures 3.3 43 to 3.3 46. The magnetisation was measured between 1.8 and 300 Kelvin, but here only the part up to 80 K is shown for clarity. Above 80 K the magnetisation is similar to the one of the other rare earth compounds discussed earlier.
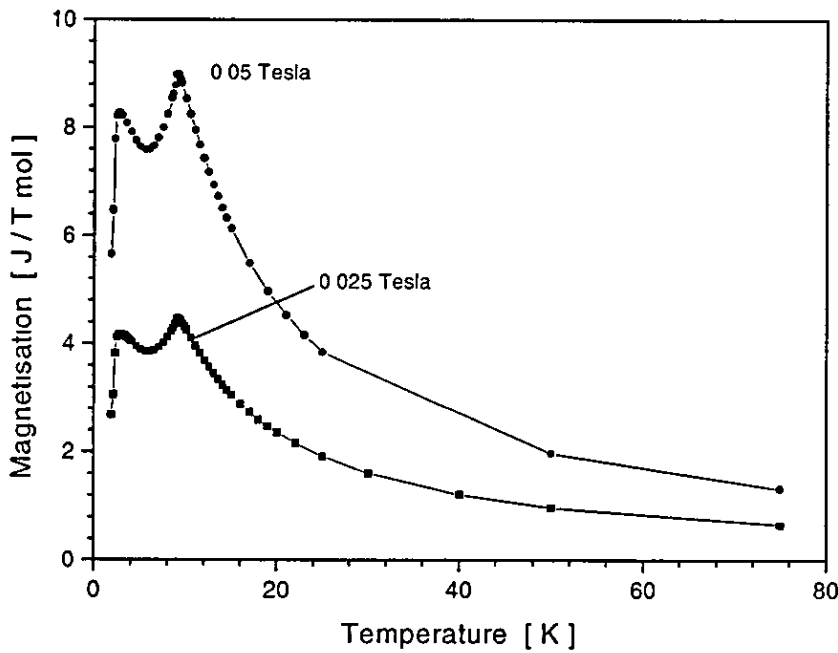

Figure 3 3 43· Magnetisation of Ho$_{14}$Ag$_{51}$ as a function of temperature at various magnetic fields

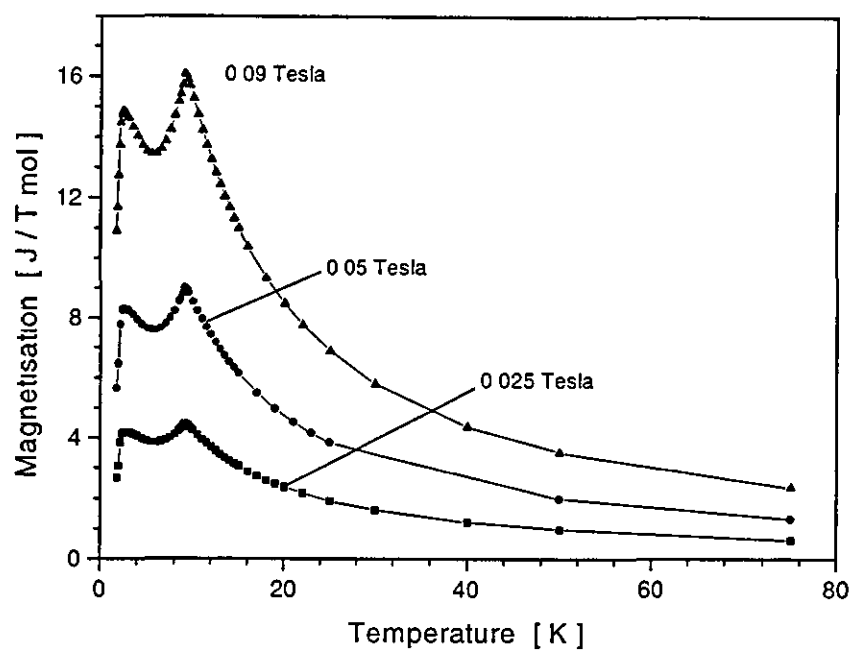*Figure 3 3 44: Magnetisation of Ho$_{14}$Ag$_{51}$ as a function of temperature at various magnetic fields*

Figure 3.3 45. Magnetisation of Ho$_{14}$Ag$_{51}$ as a function of temperature at various magnetic fields

Figure 3 3.46· Magnetisation of $Ho_{14}Ag_{51}$ as a function of temperature at various magnetic fields

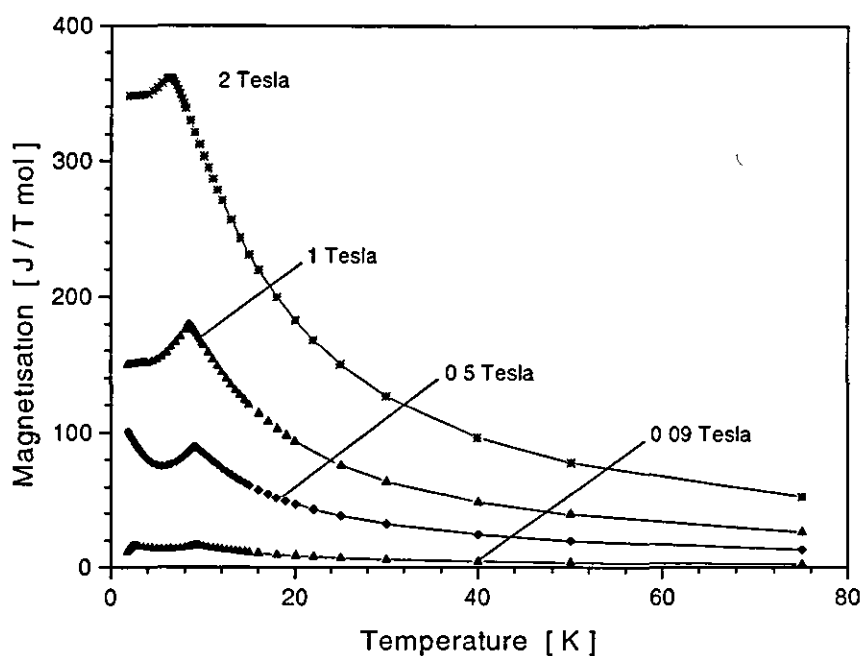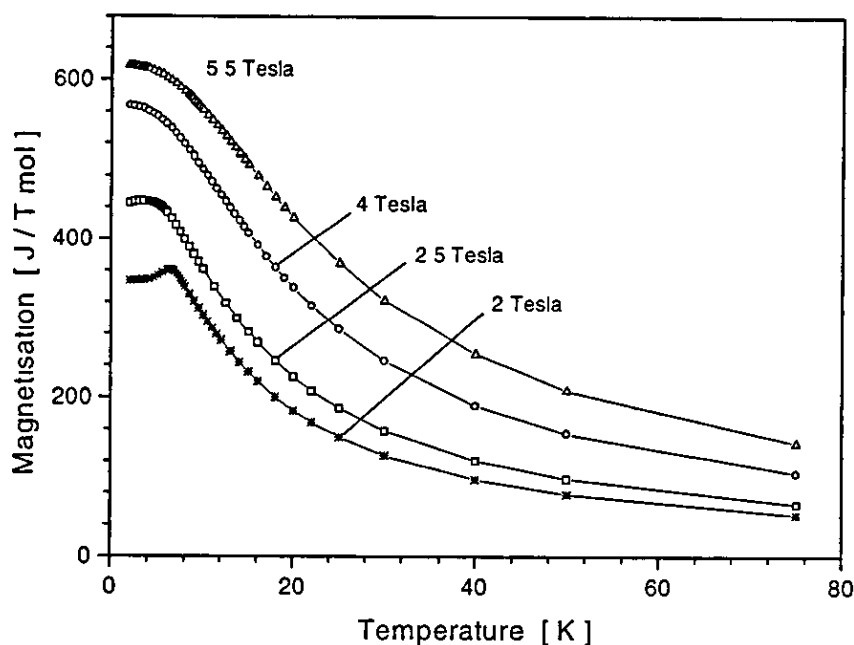From the figures it can be seen that for low applied fields two transitions appear at temperature of ~3 and ~9 Kelvin. Above ~0 09 Tesla only the second antiferromagnetic phase transition at $T_N \approx 9$ Kelvin remains. Above fields of 2.5 Tesla also this antiferromagnetic phase transition disappears and the magnetisation decreases continuously with increasing temperature A shift in the transition temperatures T_I and T_N can be seen by comparing the measurements at different magnetic fields to one another. In order to analysis the dependence of the shift as a function of applied magnetic field a plot of $\ln(T_0-T)$ versus $\ln(B)$ has been constructed. This plot is shown in figure 3 3 44. Three lines (attributed to T_I, T_N) are obtained. One line belongs to the temperature T_I and two lines to T_N. Linear fits to straight lines were carried out using $\ln(T_0 - T) = \ln(\alpha) + \beta \ln(B)$ and the following parameter were obtained:

T_N (below 2 Tesla):

$\beta = 1.57 \pm 0.06$ $\alpha = 0\,76 \pm 0\,08$ $T_0 = 9\,07 \pm 0\,02$

T_N (above 2 Tesla):

$\beta = 2\,00 \pm 0\,02$ $\alpha = 1.34 \pm 0\,03$ $T_0 = 11.7 \pm 0.2$

$$T_1: \quad \beta = 1.99 \pm 0.07 \qquad \alpha = 5.7 \pm 0.3 \qquad T_0 = 2.91 \pm 0.2$$
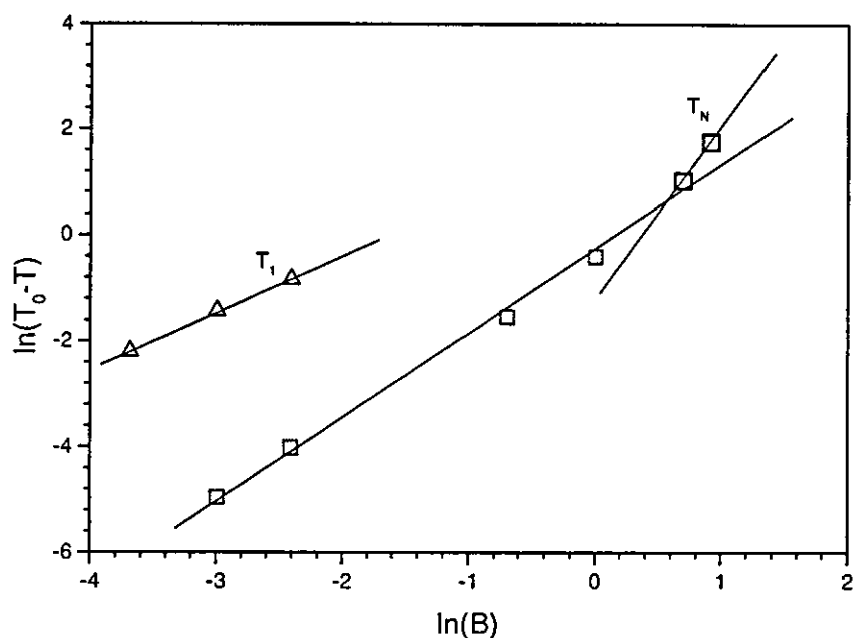
Figure 3 3 44 ln(T$_0$-T) as a function of ln(B) for the shift in the temperature of T$_1$ and T$_N$ for the Ho$_{14}$Ag$_{51}$ alloy

The fit parameter reveal the functional dependence of $T = T_0 - \alpha B^2$ for the temperature shift of T_1, and for fields larger than 2 Tesla, for T_N Below 2 Tesla the shift in the antiferromagnetic transition temperature depends on the field with an exponent of (1.57 ±0 06). A phase diagram has been constructed and is shown in figure 3 3 45 For 0 Kelvin the critical fields for T_N and T_1 phase transition lines are extrapolated to fields of magnitude (0 53 ± 0.01) Tesla for T_1 and (2.95 ± 0 01) Tesla for T_N.
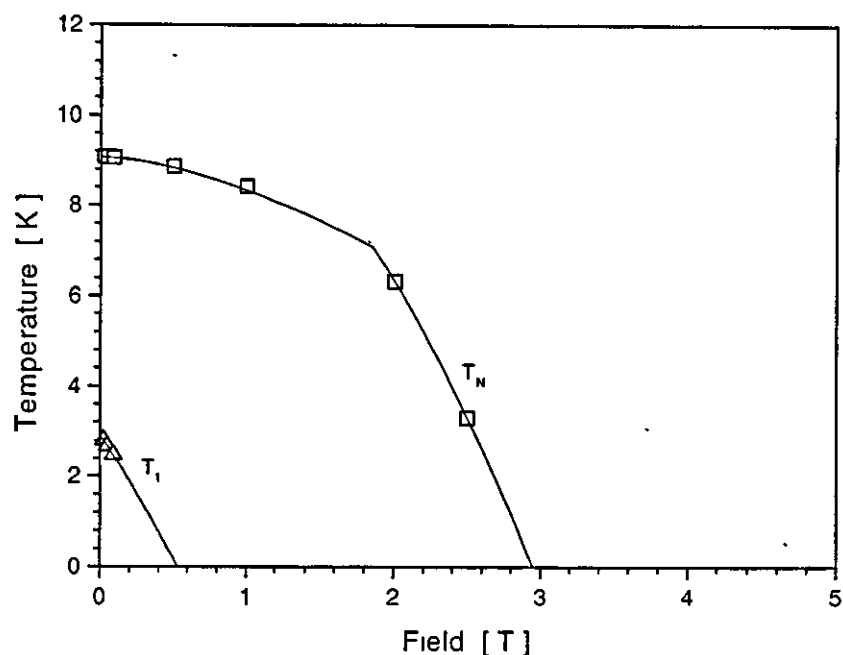
Figure 3 3 45   Phase diagram of the phase transitions T_I and T_N for $Ho_{14}Ag_{51}$

The results of the magnetisation measurements as a function of field for various temperatures are shown in figure 3.3 46 and 3 3.47. For the measurements at 1 8, 2, and 3 5 Kelvin the magnetisation "steps" are clearly visible below 3 Tesla. Above 3.5 K the magnetic transitions are washed out and then the magnetisation versus field curve becomes a smooth increasing curve. A more detailed presentation of the magnetisation at T = 1 8 K is given in figure 3.3 48 and 3.3 49.
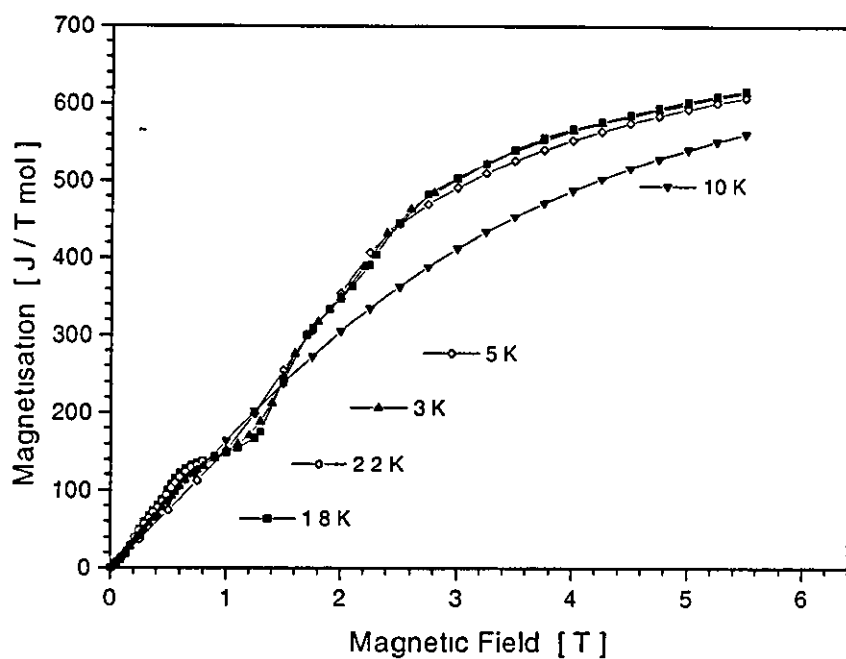
Figure 3 3 46 Molar magnetisation as a function of field at various temperatures for $Ho_{14}Ag_{51}$
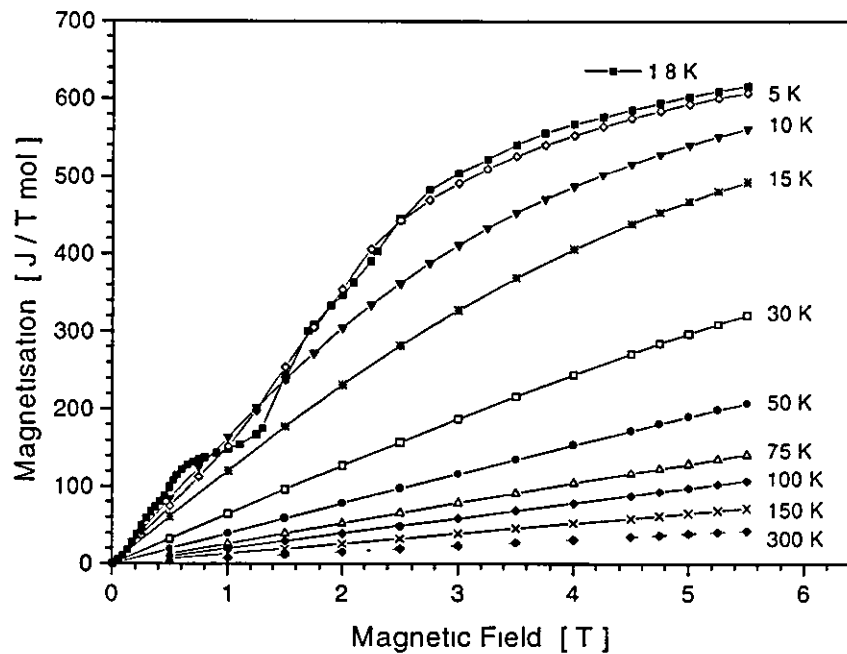
Figure 3 3 47 Molar magnetisation as a function of field at various temperatures for $Ho_{14}Ag_{51}$

91
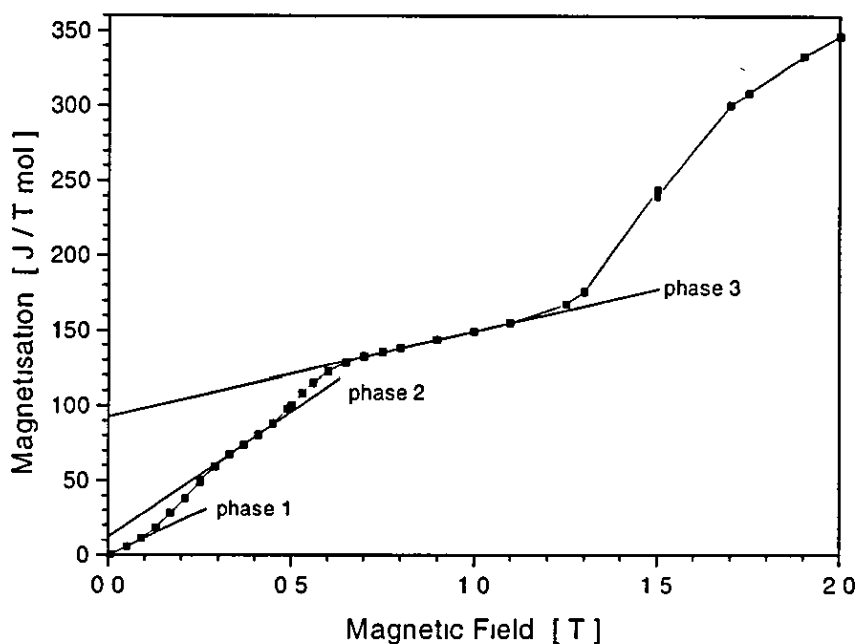
Figure 3 3 48 Molar magnetisation as a function of field at 1 8 K for Ho$_{14}$Ag$_{51}$
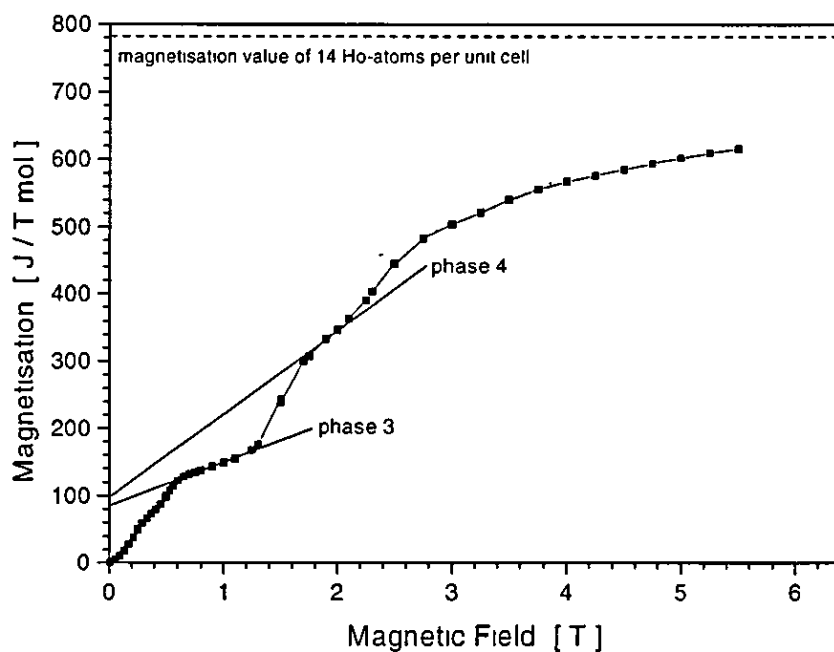
Figure 3 3 49 Molar magnetisation as a function of field at 1 8 K for Ho$_{14}$Ag$_{51}$

At 1.8 Kelvin the magnetisation versus field passes through four field induced phase transitions at 0 2, 0 6, 1.4, and 2.4 Tesla The magnetisation of the various

phases shows a linear behaviour which increases with increasing field. The magnetisation which belongs to each phase (level) has been estimated using a linear extrapolation of each level to the intersection with the magnetisation axis at zero external magnetic field. These lines are shown in figures 3.3.48 and 3.3.49. The following remnant magnetisation values have been obtained.

Phase 2:	12 J/T mol
Phase 3:	90 J/T mol
Phase 4:	100 J/T mol

The theoretical value of the total magnetisation of one Holmium atom per mol of the $Ho_{14}Ag_{51}$ compound is 55.84 J/Tmol. Comparing this calculated to the experimentally obtained value above the differences are too marked in order to be able to draw any reliable conclusions for this polycrystalline measurement. A phase diagram with all phases are shown in figure 3.3.50.
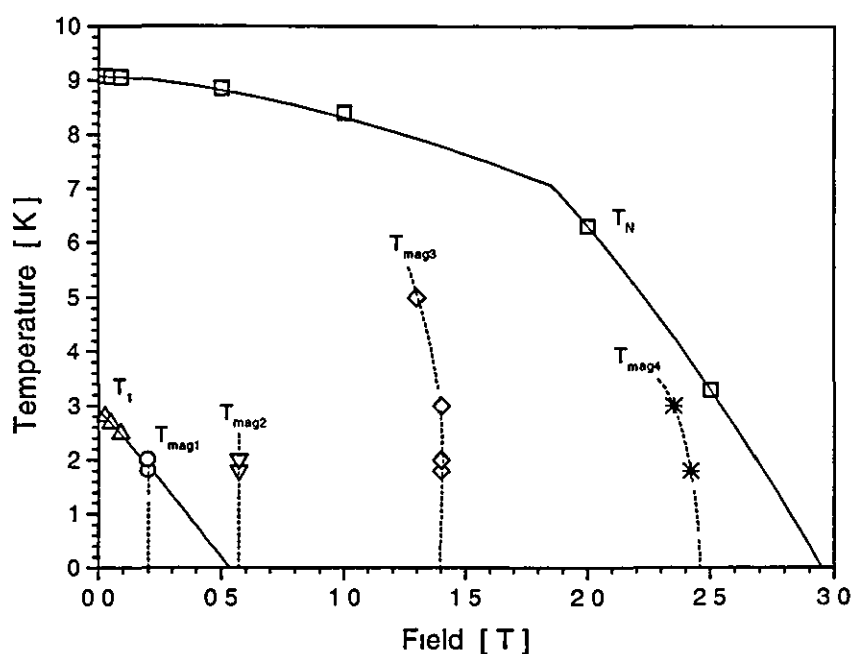
Figure 3 3 50   Phase diagram of all phase transitions for $Ho_{14}Ag_{51}$

93

Above a field of ~3 Tesla the magnetisation increases continuously with increasing field. The gradient of the magnetisation decreases with increasing applied field. Thus it may be seen that the magnetisation starts to approach saturation. The magnetisation value of 14 Holmium atoms per unit cell amounts to 781.8 J/Tmol and is also indicated in figure 3.3 49.

The Arrott plots of the isotherm magnetisation measurements are shown in figure 3.3.50 and 3.3.51. By using the Arrott plots for temperatures higher than T_N. values of the inverse susceptibility, extrapolated to zero magnetic field, are obtained These values are plotted as a function of temperature in figure 3 3.52
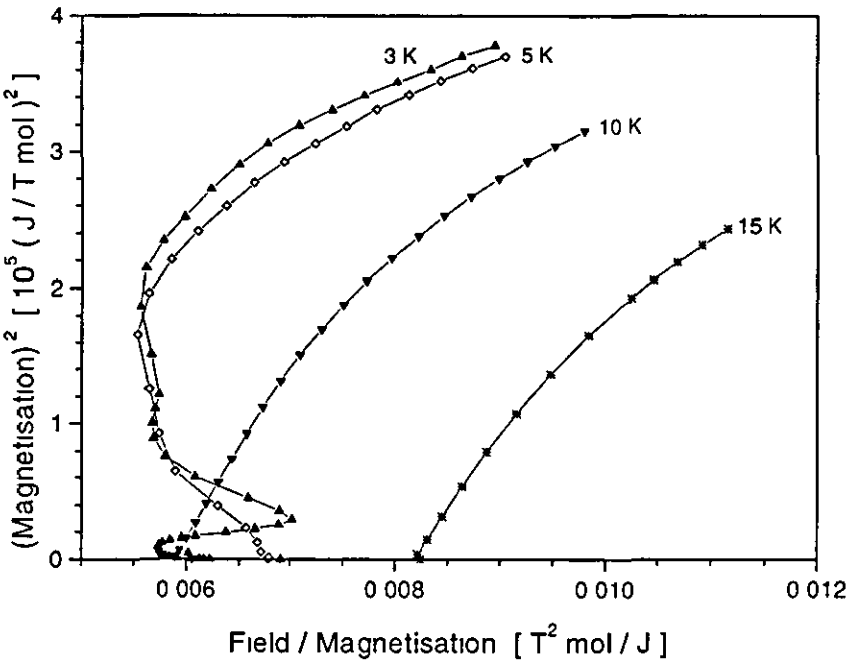
Figure 3 3 50   Arrott plots at various temperatures for $Ho_{14}Ag_{51}$
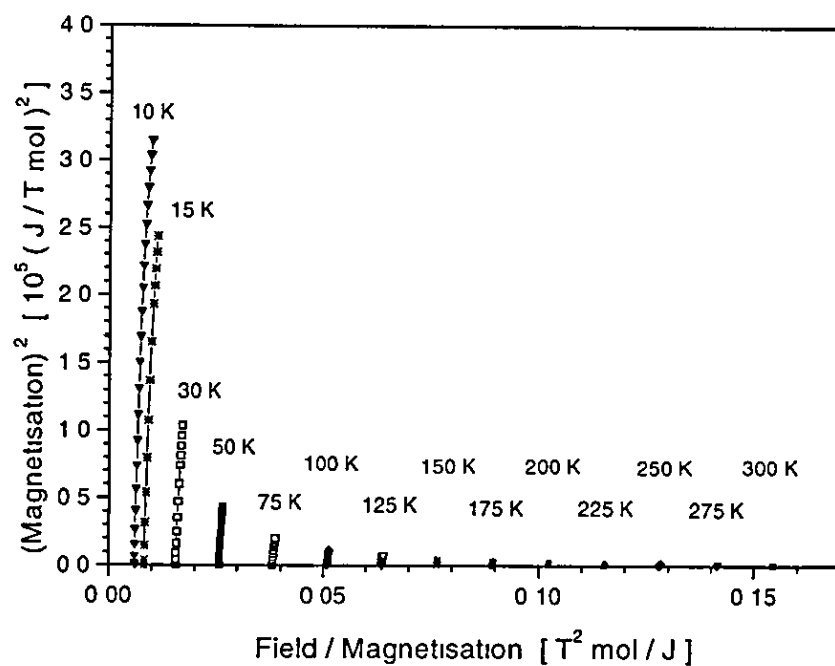
Figure 3 3 50 Arrott plots at various temperatures for Ho$_{14}$Ag$_{51}$
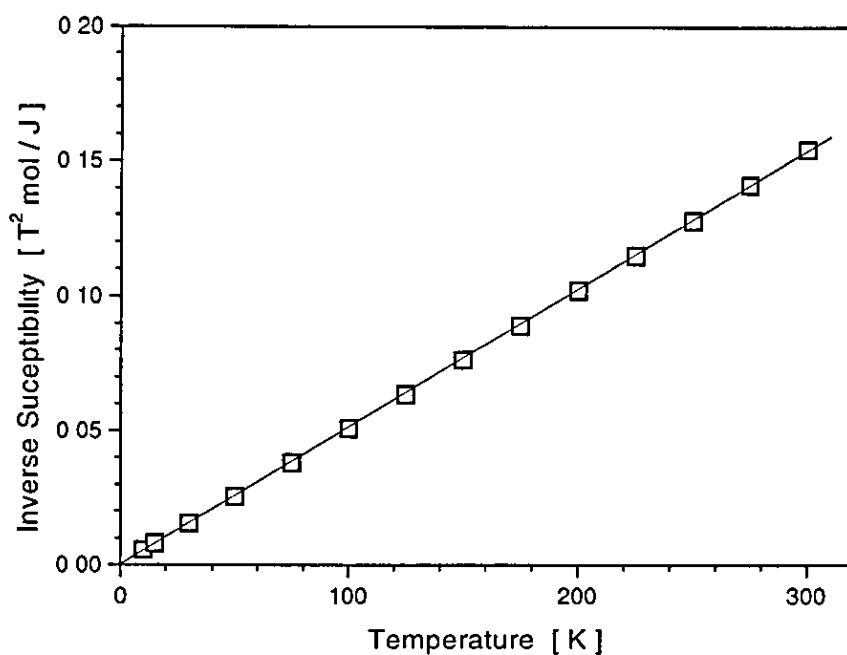
Figure 3 3.52· Inverse susceptibility as a function of temperature obtained by Arrott plots for Ho$_{14}$Ag$_{51}$

The paramagnetic behaviour of $Ho_{14}Ag_{51}$ is well described by a Curie Weiss law. A linear fit through the data points of figure 3.3 52 yields the slope from which the molar Curie constant and thus $p_{eff} = 10.54 \pm 0.04$ can be determined The theoretical value of p_{eff} is given as $p_{eff} = 10 6$. For the paramagnetic Curie temperature θ_N a value of $\theta_N = (-0.4 \pm 0.2)$ K has been obtained.

The alloy $Er_{14}Ag_{51}$

SQUID measurements have been carried out also for the rare earth compound of $Er_{14}Ag_{51}$ within a temperature range of 1.8 to 300 K. In figures 3 3.53 to 3.3.56 the magnetisation is shown as a function of temperature.
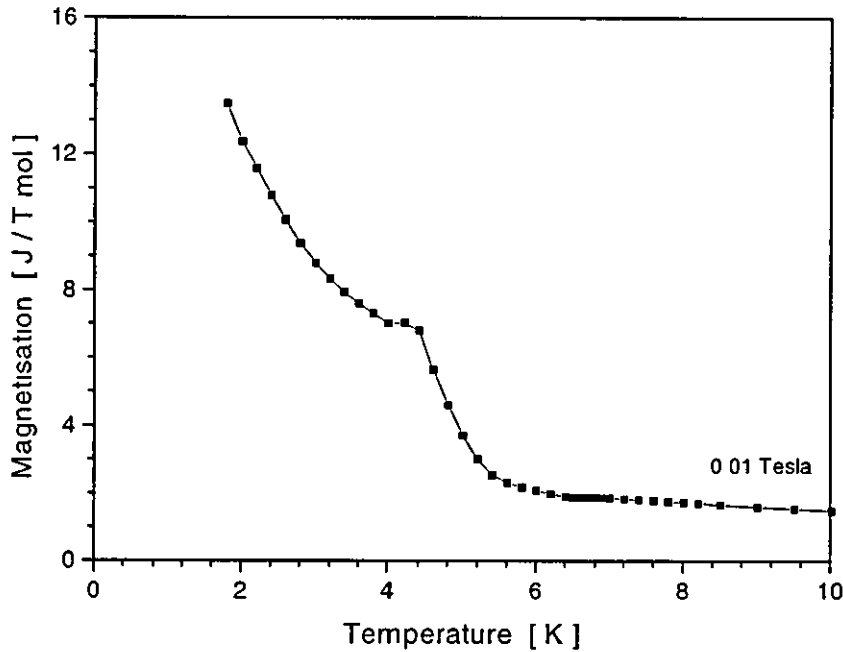
Figure 3 3 53 Magnetisation as a function of temperature for $Er_{14}Ag_{51}$ in a field of 0 01 Tesla
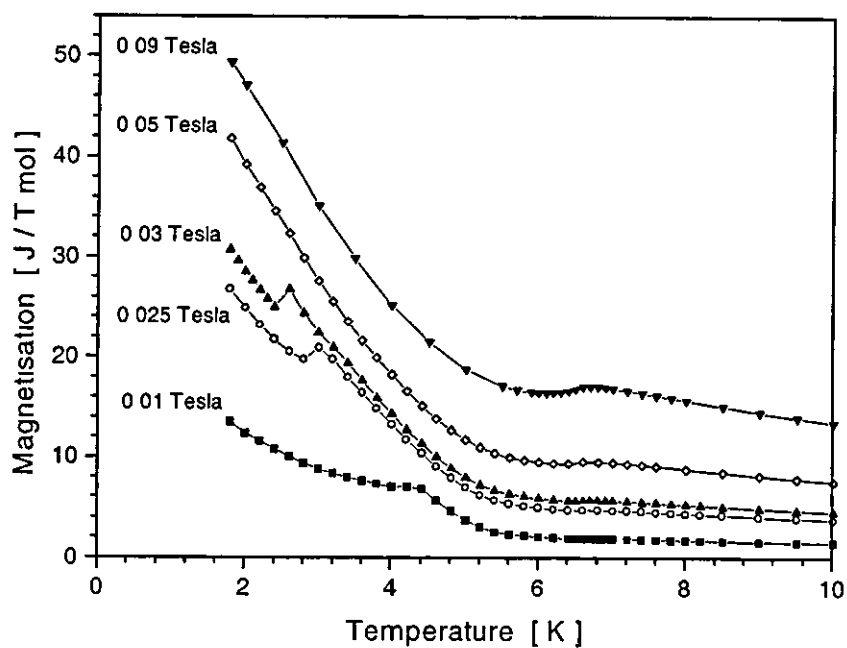
Figure 3 3 54. Magnetisation as a function of temperature for $Er_{14}Ag_{51}$ for various fields
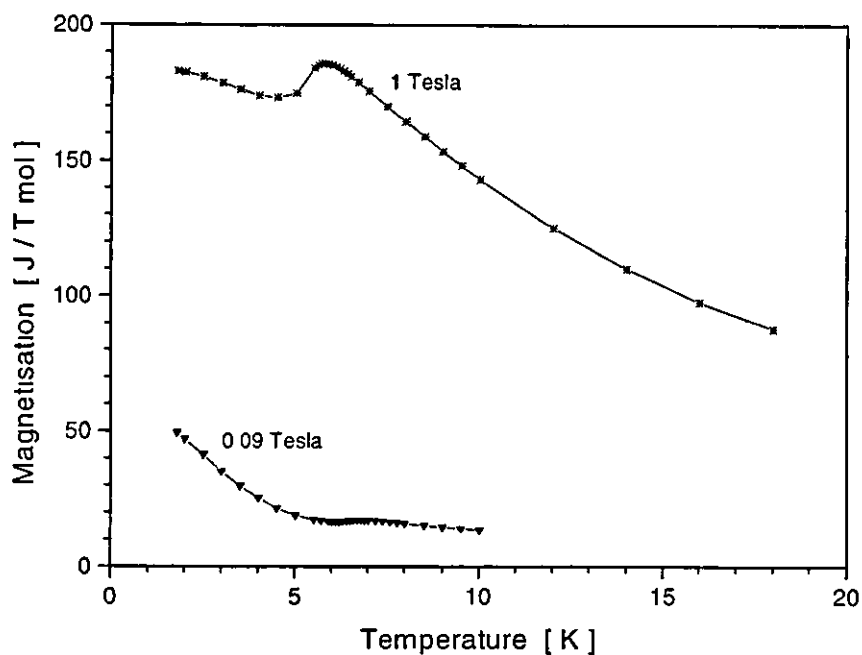
Figure 3 3 55. Magnetisation as a function of temperature for $Er_{14}Ag_{51}$ for various fields

97
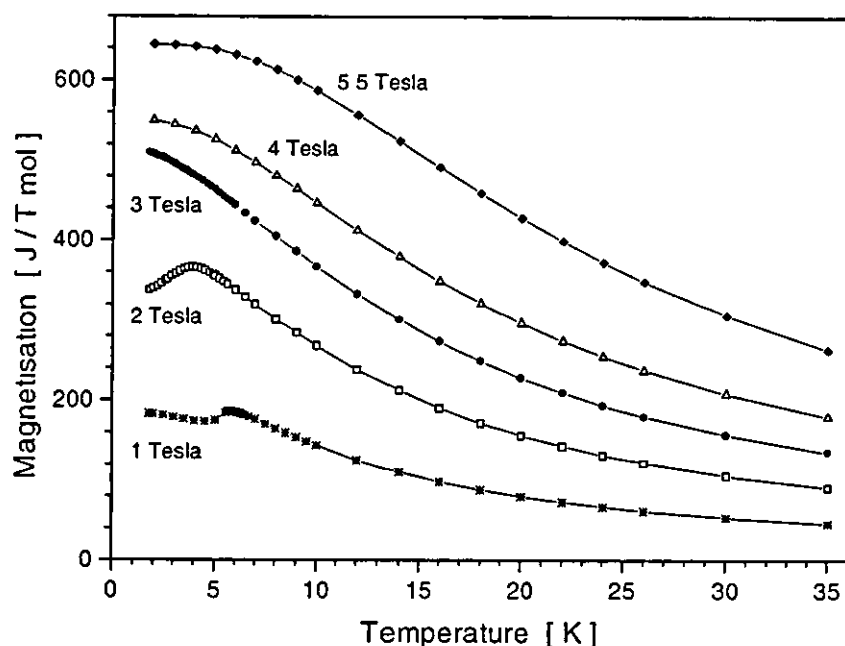
Figure 3 3 56· Magnetisation as a function of temperature for $Er_{14}Ag_{51}$ for various fields

In these figures two magnetic phase transitions can be identified In small fields the first transition occurs at a temperature T_1 of ~3 Kelvin. This transition is absent in the measurement at 3 Tesla A second phase transition T_N of ~6 5 Kelvin is indicated by a very prominent peak at low fields. At higher field values the peak sharpens, and for fields above 2 Tesla this transition disappears.

The temperature shift of the phase transitions have been analysed using a logarithmic plot of $\ln(T_0 - T)$ versus $\ln(B)$. This plot is shown in figure 3.3.57.
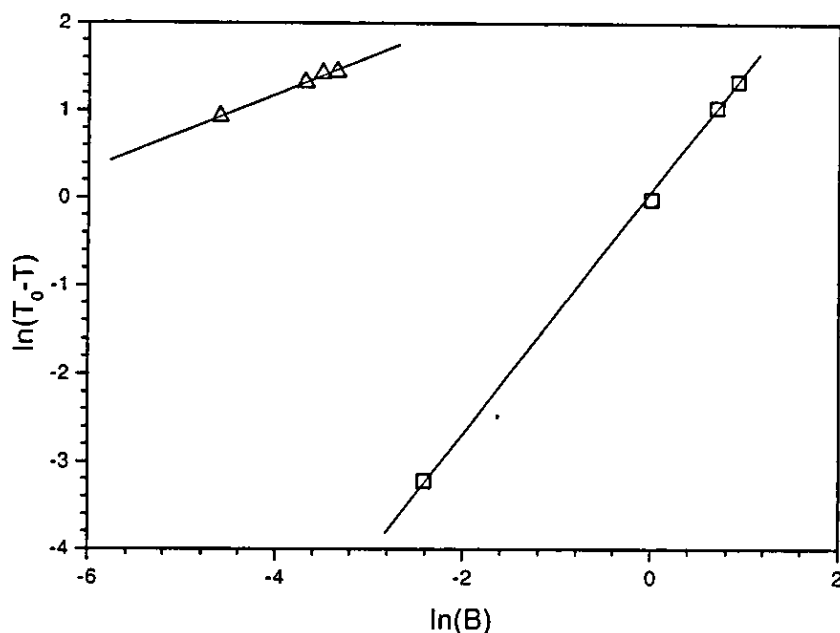
Figure 3 3 57. Plot of $\ln(T_0 - T)$ as a function of $\ln(B)$ for the temperature shifts of the transitions T_1 and T_N for $Er_{14}Ag_{51}$

The temperature shift of both transitions reveals a power law behaviour. Linear fits to the data points yield fit parameters β and α.

T_N $\beta = 1.37 \pm 0\,03$ $\alpha = 1\,0 \pm 0.5$ $T_0 = 6\,74 \pm 0.3$

T_1 · $\beta = 0.95 \pm 0\,06$ $\alpha = 65 \pm 3$ $T_0 = 5\,0 \pm 0.1$

Thus the temperature shift of the transition temperature T_1 is a linear function of the applied field. The transition temperature T_N does not have a conventional field dependence. In particular the value of 1.37 for the exponent of B is significantly different from 2. Such a behaviour may arise due to the presence of a L M coupling term within the free energy expansion in addition to the $L^2\,M^2$ one. Combined with a powder average the above dependence may arise.

The magnetisation of $Er_{14}Ag_{51}$ as a function of applied field has been measured in the range of 0.005 to 5.5 Tesla. Some graphs of these measurements are shown in figures 3.3.58, 3 3.59, and 3 3 60.
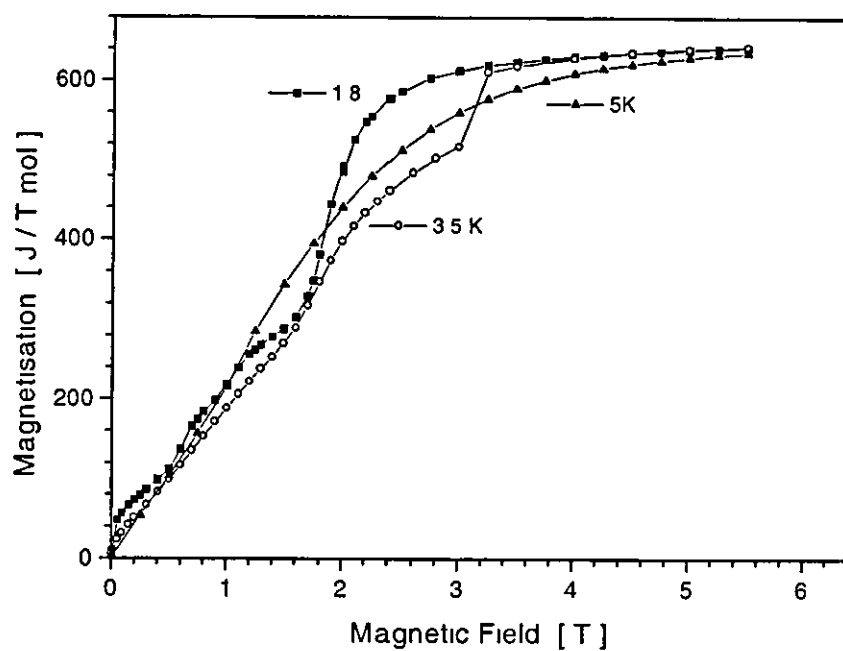
Figure 3 3 58· Magnetisation as a function of magnetic field at various temperatures for $Er_{14}Ag_{51}$
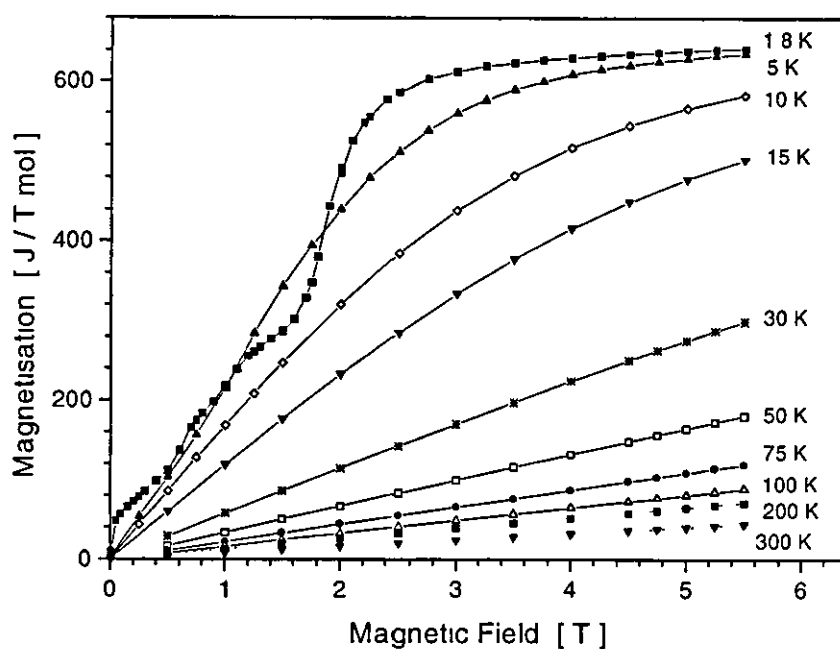
Figure 3 3 59 Magnetisation as a function of magnetic field at various temperatures for $Er_{14}Ag_{51}$
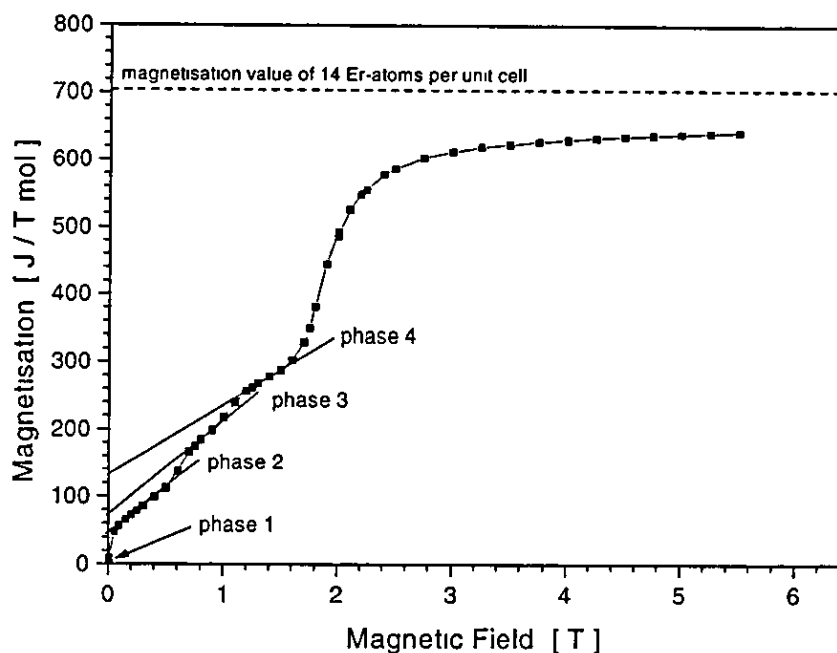
Figure 3 3 60: Magnetisation as a function of magnetic field at 1.8 Kelvin for $Er_{14}Ag_{51}$

Clear step features are seen in the graphs for the 1 8 and 3 5 Kelvin measurements. Three field induced phase transitions occur at magnetic fields of ~0 06, ~0.61, and ~1 05 Tesla. The magnetisation values of the phases between the transitions are obtained as ~45 J/Tmol for phase 2, ~75 J/Tmol for phase 3, and ~130 J/Tmol for phase 4 (see figure 3 3 58). All three values may be related to a multiple of the theoretical magnetisation of one Erbium atom per mole namely 50.26 J/Tmol. The phase diagram is given in figure 3 3.61. The critical fields at zero temperature are obtained as $(0.068 \pm 0\ 004)$ Tesla for T_1 and for T_N as $(3.8 \pm 0\ 2)$ Tesla.
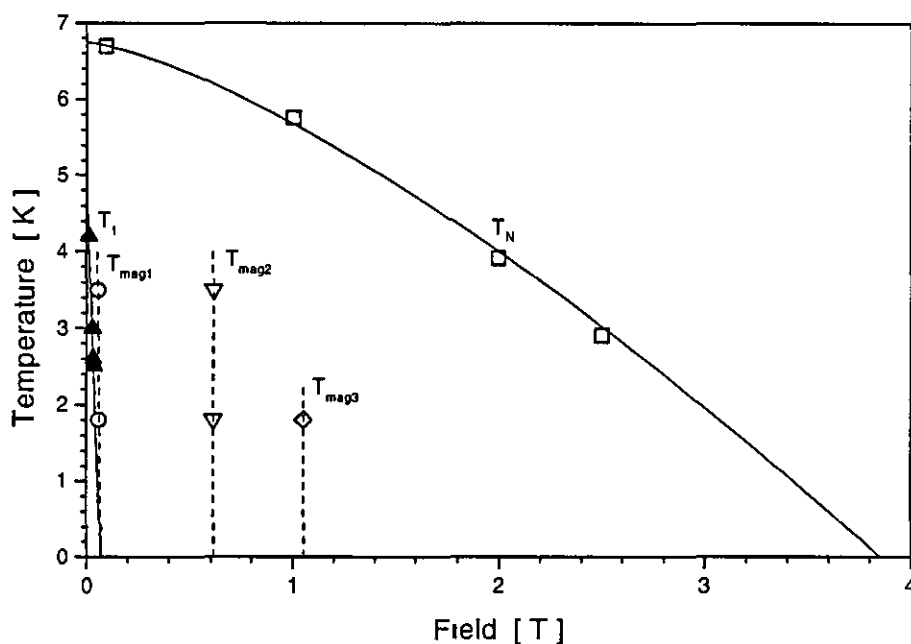
Figure 3 3 61 · Phase diagram of all obtained phase transitions for the alloy Er₁₄Ag₅₁

Using the measurements shown in figure 3.3.59 Arrott plots have been constructed and values for the inverse susceptibility have been obtained at various temperatures as described in detail for the other rare earth alloys. The Arrott plots are shown in figures 3.3 62 and 3.3.63. The temperature dependence of the inverse susceptibility is shown in figure 3.3.64 A paramagnetic behaviour is characterised by a the Curie-Weiss law. A linear fit to the data has been carried out, and a paramagnetic Curie temperature θ_N = (1.7 ± 0 2) K and a value of p_{eff} of p_{eff} = 9.6 ± 0 1 have been obtained. The theoretical value of p_{eff} for Erbium is given by p_{eff} = 9 6. Thus experimental and theoretical values are in excellent agreement
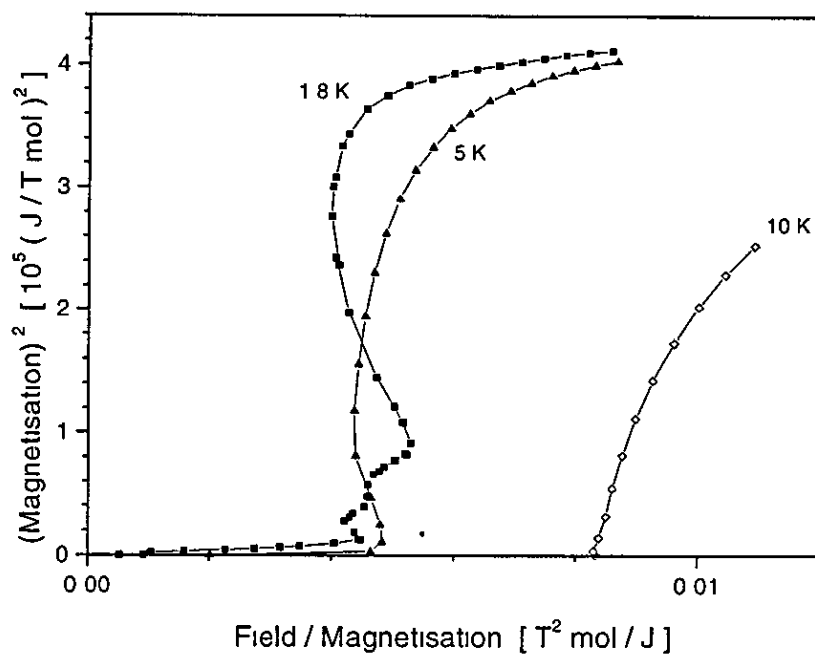
Figure 3 3 62 Arrott plots for the alloy Er$_{14}$Ag$_{51}$ (low temperatures)
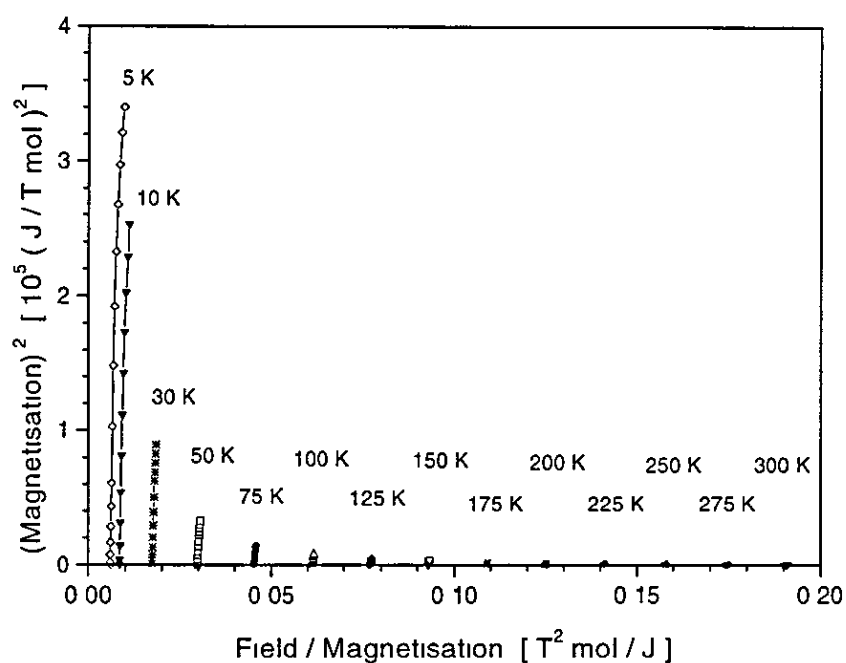
Figure 3 3 63 Arrott plots for the alloy Er$_{14}$Ag$_{51}$ (high temperatures)

103
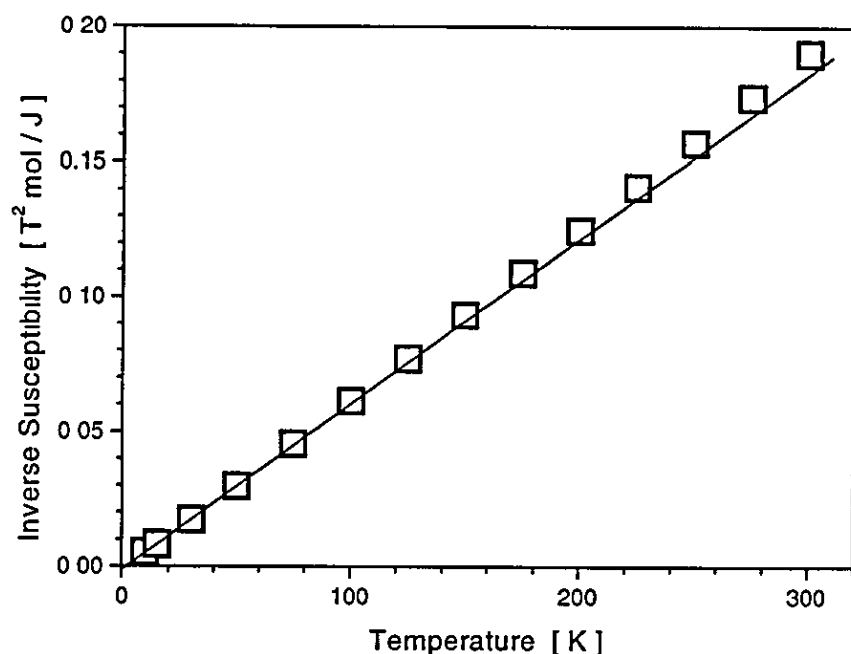
Figure 3 3 64: Inverse molar susceptibility as a function of temperature for the alloy Er₁₄Ag₅₁ obtained using Arrott plots

The alloy La$_{14}$Ag$_{51}$

The La$_{14}$Ag$_{51}$ has been included in order to allow the investigation of a non magnetic reference compound for the alloy series RE$_{14}$Ag$_{51}$. Lanthanum (La) is the first rare earth element in the periodic table and belongs to the light rare earth elements. The rare earth alloys which are considered here contain heavy magnetic rare earth elements between Gadolinium and Erbium. Therefore, it would be more logical to expect the element Lutetium (Lu) to be used for the non magnetic reference compound. However, for Lutetium an alloy within the Ag$_{51}$Gd$_{14}$ structure type does not exist (McMaster et al. [1]) and thus an isostructural Lu-based reference sample is not available. As the appropriate La-compound does exist, this has been chosen as the non-magnetic reference compound.

Magnetisation measurements have been carried out as a function of temperature and magnetic field for $La_{14}Ag_{51}$ in an identical manner to the measurements of the magnetic compounds. For this compound the signal in the magnetisation was found to be very small and a big sample had to be measured for obtaining reliable values of the magnetisation. The weight of this sample was twenty times larger than that of the other rare earth samples. The measurements of the magnetisation as a function of temperature are shown in figure 3.3.65.
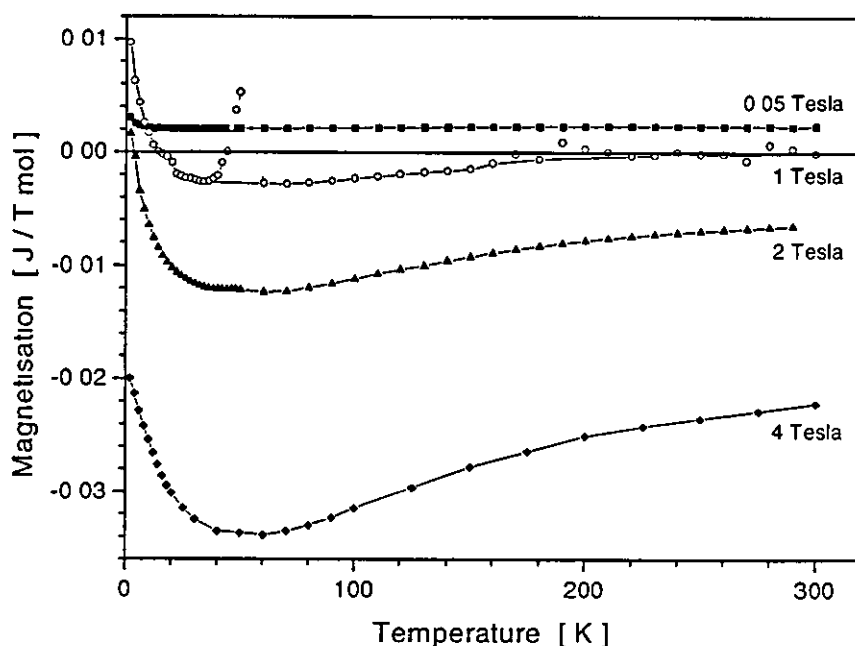
Figure 3 3 65   Molar magnetisation as a function of temperature for $La_{14}Ag_{51}$

From the y-scale of figure 3.3.65 it can be seen that the molar magnetisation is significantly smaller compered to the magnetisation of the magnetic rare earth compounds. Furthermore, it is clearly shown that the $La_{14}Ag_{51}$ compound is diamagnetic for large values of the applied field. The magnetisation above a field at 1 Tesla is negative and the negative value increases with increasing field. At low fields below ~1 Tesla the magnetisation is positive. This is attributed to the presence of paramagnetic impurities. All magnetisation curves drop to a local minimum at ~55 K and increase again slowly with increasing temperature. Only a weak temperature dependence is observed. The sharp peak in the measurement at 1 Tesla attributed to a small amount of oxygen in the system. After heating the

sample to ~100 K and pumping for a couple of hours the oxygen was removed. The amount, which could not be removed using this procedure, gives rise to the small bump in the measurement at 2 Tesla.

In figure 3.3.66 the magnetisation measured is shown as a function of magnetic field for various temperatures.
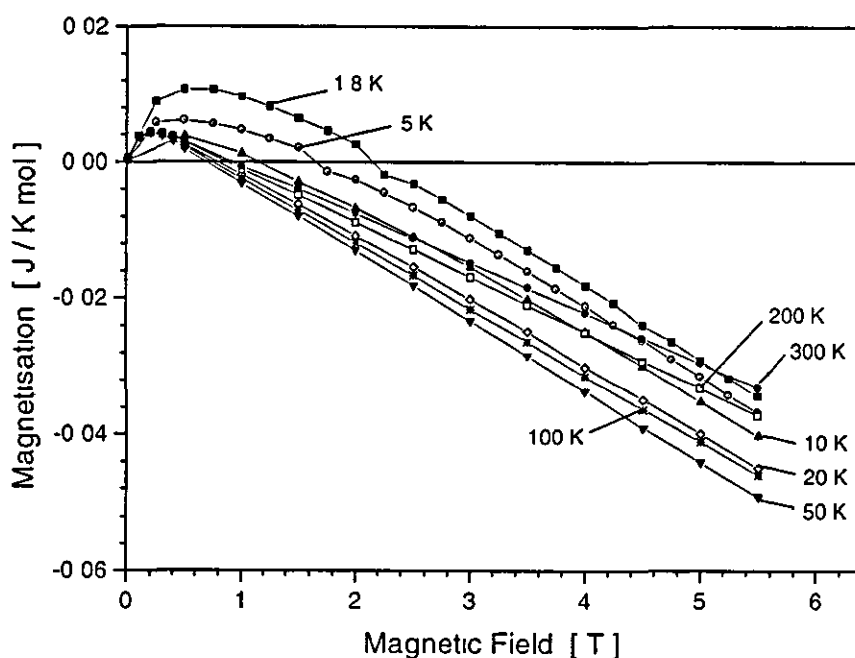
Figure 3 3 66   Molar magnetisation as a function of magnetic field at various temperatures for $La_{14}Ag_{51}$

Figure 3 3 66 clearly reveals the weak temperature dependence of the magnetisation for all temperatures. The magnetisation starts at zero and increases. It reaches a maximum at ~0 4 Tesla After this maximum the magnetisation decreases linear with increasing magnetic field and becomes negative. This confirm that $La_{14}Ag_{51}$ is a diamagnet.
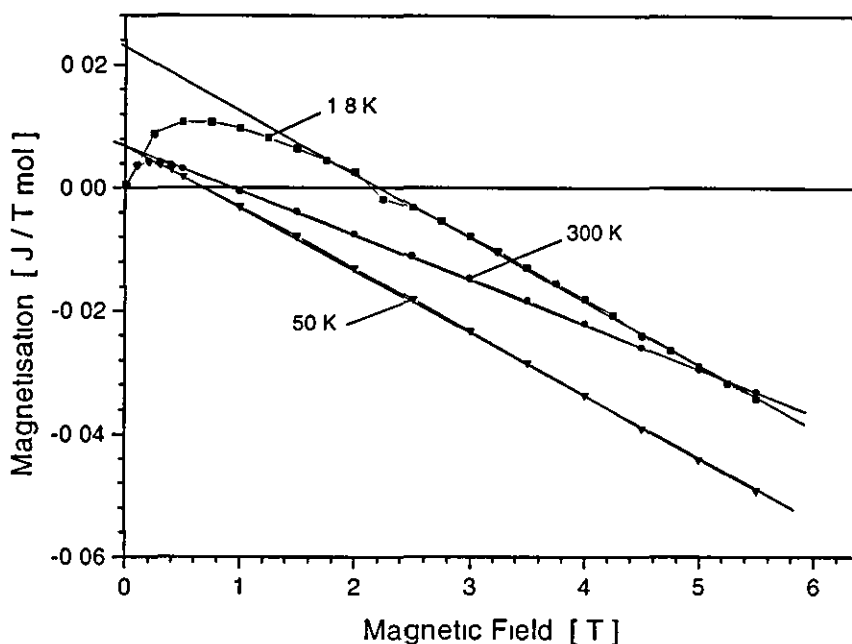
Figure 3 3 67   Molar magnetisation as a function of field for La₁₄Ag₅₁ The
intersections with the magnetisation axis indicate the paramagnetic magnetisation
which is attributed to an impurity

From the high field part of the magnetisation curve of figure 3.3.67 a zero field
magnetisation is extrapolated of approximately 0.02 J/Tmol. This is the magnetic
moment of a paramagnetic impurity phase in the La₁₄Ag₅₁ sample. Under the
assumption that this phase is iron the magnetisation would require ~0 2% of the
La₁₄Ag₅₁ sample to be iron. For a rare earth impurity the percentage value would
be reduced to ~0 05% This is indeed a very small value. It is only observable
here due to the intrinsic smallness of the magnetic signal of La₁₄Ag₅₁.

For the further analysis only the linear part of the magnetisation at high fields
was used. The slope of the linear part yields the value of the susceptibility for
each isotherm. The resulting values of χ are plotted against temperature in
figure 3 3 68.
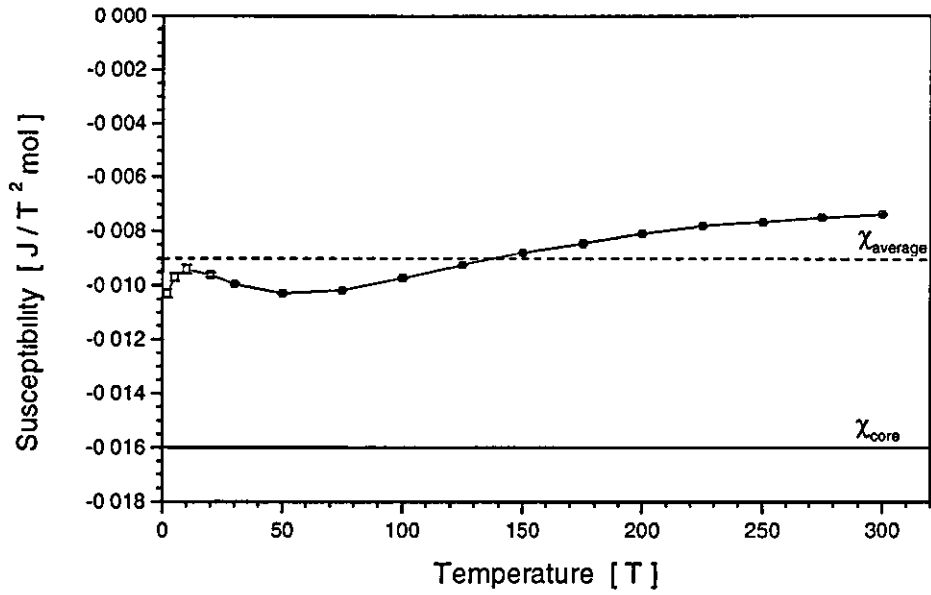
Figure 3 3 68. Molar susceptibility as a function of temperature The solid line indicate the value of the susceptibility of the atom cores of –0 016 J/T²mol The dashed line shows an estimated average value of the temperature independent susceptibility of –0 009 J/T²mol

The susceptibility in figure 3.3 68 shows only a weak temperature dependence. For the following this temperature dependence will be neglected. The average value of the susceptibility has been estimated to χ = -0.09 J/T²mol. This susceptibility is composed of contributions

$$\chi = \chi_{core} + \chi_{Pauli} + \chi_{Lan} + \chi_{Vleck} \,, \qquad\qquad [3.115]$$

where

χ_{core} originates from the diamagnetic contribution of the atom core,

χ_{Pauli} is the Pauli paramagnetic term,

χ_{Lan} is the Landau diamagnetisation, and

χ_{Vleck} is due to the orbital Van Vleck contribution.

108

Alloy	B_{C1} [T]	M_1 [J/Tmol]	B_{C2} [T]	M_2 [J/Tmol]	B_{C3} [T]	M_3 [J/Tmol]	B_{C4} [T]	M_{one} [J/Tmol]
$Gd_{14}Ag_{51}$	-	-	-	-	-	-	-	39 09
$Tb_{14}Ag_{51}$	2.5	40	5.1	-	-	-	-	50 26
$Dy_{14}Ag_{51}$	0 75	40	2 42	80	4 85	-	-	55.84
$Ho_{14}Ag_{51}$	0.2	12	0 57	90	1 4	100	1.42	55 84
$Er_{14}Ag_{51}$	0 06	45	0 61	75	1 05	130	-	50 26

Table 3 3 3. Magnetic characteristics of field induced magnetic phase transitions of $RE_{14}Ag_{51}$

With the help of isothermal magnetisation measurements Arrott plots have been constructed. Using these Arrott plots values for the inverse susceptibility have been obtained in the absence of an applied magnetic field for various temperatures. The paramagnetic regime is well described by a Curie Weiss law. A straight line fit of the inverse susceptibility versus temperature data yields values for the effective paramagnetic Bohr magneton number p_{eff} and the paramagnetic Curie temperature θ_N. These are listed in table 3.3.4.

Alloy	T_N [K]	T_1 [K]	θ_N [K]	p_{eff} obs	p_{eff} cal
$Gd_{14}Ag_{51}$	36 7 ± 0 1	13.6 ± 0 1	-6 9 ± 1	8.1 ± 0 1	7 94
$Tb_{14}Ag_{51}$	27.8 ± 0 1	~ 15	1 2 ± 1	9 9 ± 0 3	9.7
$Dy_{14}Ag_{51}$	17.3 ± 0.1	~ 4	-0 4 ± 0 5	10 9 ± 0 3	10 6
$Ho_{14}Ag_{51}$	9.1 ± 0 1	2 8 ± 0 1	-0 4 ± 0 2	10 54 ± 00 4	10 6
$Er_{14}Ag_{51}$	6 7 ± 0 1	4 2 ± 0 1	1 7 ± 0 2	9 65 ± 0 1	9 6

Table 3 3 4 Magnetic characteristics of $RE_{14}Ag_{51}$

Chapter 4: Low Temperature Properties of $RE_{14}Ag_{51}$

Introduction

Specific heat is a physical property which provides information on the internal energy and the entropy of a substance. Furthermore, the measurement of the specific heat yields information on the electronic density of states at the Fermi level and the existence of phase transitions. The onset of a correlated state generally reduces the entropy of a system and therefore depending on the nature of the transition, can manifest itself as an anomaly in the specific heat. An analysis of such anomalies allows a quantitative and qualitative investigation to be obtained of the nature of the ordered state in a solid Thus specific heat measurements, which may be isolated or combined the other measurements of physical properties, are a powerful and useful tool for studying the properties of solids.

The behaviour of the specific heat with respect to temperature is a result of the change in the internal energy. The internal energy of a solid is affected by lattice dynamics, the energy given by the density of electrons at the Fermi level in metals and by magnetic contributions for materials with a magnetic degree of freedom. Therefore the total specific heat can be considered as being composed of various contributions from the phonon, the electronic and the magnetic subsystems.

The theory of the specific heat of solids is briefly summarised in this chapter in section 4.1 starting with the discussion of the difference between C_p and C_V, and going on to discuss the specific heat contribution from the lattice, electrons and magnetic moments. An overview of the equipment is given in section 4.2 and a description is presented of the calorimeter. In section 4.3 the specific heat measurements of the $RE_{14}Ag_{51}$ compounds (RE = La, Gd, Tb, Dy, Ho, and Er) are presented and discussed.

4.1 Theory of Specific Heat

Theory of C_p and C_V

When a solid of unit mass receives a quantity of heat dQ, and its temperature rises by dT the specific heat is defined by

$$C = \frac{dQ}{dT}.$$
[4.1]

The specific heat of a solid can be determined experimentally by heating a sample and measuring its temperature change. Due to the specific heat being directly related to the internal energy of a solid some properties of samples can be investigated and analysed by measuring the specific heat. The first law of thermodynamics gives the relation between the "energy input" dQ, the change of the internal energy dU and the work which is done due to a change in volume dV at a given pressure p.

$$dQ = dU + pdV$$
[4.2]

As a result of the second law of thermodynamics the "input energy" can be written as TdS where dS is the change in the entropy S. Thus the change of the internal energy U of a closed hydrostatic system is given by

$$dU = TdS - pdV .$$
[4.3]

From this equation the specific heat can be derived at constant pressure and at constant volume of a system as a function of the internal energy U.

$$C_p = \left(\frac{\partial U}{\partial T}\right)_p + p\left(\frac{\partial V}{\partial T}\right)_p$$
[4.4]

$$C_V = \left(\frac{\partial U}{\partial T}\right)_V$$
[4.5]

For conventional experiments it is the specific heat at constant pressure which is being determined However, for theoretical models the specific heat at constant volume is evaluated. As seen in the equations [4 4] and [4 5] there is a difference between C_p and C_V. This difference can be evaluated and thus the measured value for C_p may be related to the specific heat obtained by model calculations Replacing dQ in equation [4.1] by the term TdS yields

$$C_p = T\left(\frac{\partial S}{\partial T}\right)_p$$ [4.6]

and

$$C_V = T\left(\frac{\partial S}{\partial T}\right)_V$$ [4.7]

From statistical mechanics it is known that the entropy S depends on the temperature T, volume V and number of molecules N. As $S = S(T,V,N)$ the total differential of the entropy is given by

$$dS = \left(\frac{\partial S}{\partial T}\right)_{V,N} dT + \left(\frac{\partial S}{\partial V}\right)_{T,N} dV + \left(\frac{\partial S}{\partial N}\right)_{T,V} dN$$ [4 8]

The solids considered here are a closed system and therefore the number of particles N is fixed. The total differential for S becomes

$$dS = \left(\frac{\partial S}{\partial T}\right)_V dT + \left(\frac{\partial S}{\partial V}\right)_T dV$$ [4.9]

If equation [4.9] is differentiated with respect to T for constant p then both differential terms

$$\left(\frac{\partial S}{\partial T}\right)_p = \left(\frac{\partial S}{\partial T}\right)_V + \left(\frac{\partial S}{\partial V}\right)_T \left(\frac{\partial V}{\partial T}\right)_p$$ [4.10]

and

$$C_p = T\left(\frac{\partial S}{\partial T}\right)_p = T\left(\frac{\partial S}{\partial T}\right)_V + T\left(\frac{\partial S}{\partial V}\right)_T \left(\frac{\partial V}{\partial T}\right)_p = C_V + T\left(\frac{\partial S}{\partial V}\right)_T \left(\frac{\partial V}{\partial T}\right)_p$$

$$[4.11]$$

$$C_p - C_V = T\left(\frac{\partial S}{\partial V}\right)_T \left(\frac{\partial V}{\partial T}\right)_p .$$

$$[4.12]$$

To eliminate the entropy expression it is convenient to employ the following Maxwell relations

$$\left(\frac{\partial S}{\partial V}\right)_T = \left(\frac{\partial p}{\partial T}\right)_V$$

$$[4.13]$$

and

$$\left(\frac{\partial T}{\partial V}\right)_p \left(\frac{\partial V}{\partial p}\right)_T \left(\frac{\partial p}{\partial T}\right)_V = -1 .$$

$$[4.14]$$

Thus the difference of the specific heats C_p and C_V is given by

$$C_p - C_V = T\left(\frac{\partial p}{\partial T}\right)_V \left(\frac{\partial V}{\partial T}\right)_p = -T\left(\frac{\partial p}{\partial V}\right)_T \left(\frac{\partial V}{\partial T}\right)_p^2 .$$

$$[4.15]$$

With the volume expansion coefficient α

$$\alpha = \frac{1}{V}\left(\frac{\partial V}{\partial T}\right)_p$$

$$[4.16]$$

and the isothermal compressibility κ

$$\kappa = -\frac{1}{V}\left(\frac{\partial V}{\partial p}\right)_T$$

$$[4.17]$$

equation [4.15] can be expressed as

$$C_p - C_V = TV\frac{\alpha^2}{\kappa} .$$

$$[4.18]$$

116

Obviously C_p is larger than C_V, as α and κ are positive The difference between C_p and C_V is positive and increases linearly with increasing temperature At low temperatures the difference is very small and as the temperature tends towards zero Kelvin the value of C_p will be equal to C_V.

Lattice contribution to the specific heat

Lattice vibrations often provide the largest contribution to the specific heat in a solid, especially at high temperatures. With decreasing temperature the energy of the oscillating atoms decreases.

There are various models which allow an approximate description of the motion of atoms. One of these model is the classical one by Dulong and Petit The model assumes that all atoms in a solid have the same energy. The internal energy U is given by the summation over all energies. Consequently the specific heat C_V (see equation [4.5]) is constant and temperature independent and has the value of $3 k_B N$, where N is the number of atoms.

Einstein proposed a theory based on Planck's quantum hypothesis by assuming that each atom vibrates independently of other atoms about its equilibrium position with an angular frequency ω. Furthermore, each atom has the same frequency. So the solid may be seen as a lattice of independent harmonic oscillators with quantised energy spectra. The occupancy of these quantised energy levels are determined by a Bose-Einstein distribution function. Therefore, the internal energy becomes

$$U = \frac{3 N \hbar \omega}{\exp[\beta \hbar \omega] - 1},$$
[4.19]

where N is the number of atoms, $\hbar$ the Planck constant and $\beta = (k_B T)^{-1}$ Within the written model the specific heat is obtained as

$$C_V = 3R \left(\frac{\theta_E}{T} \right)^2 \frac{\exp[\theta_E/T]}{(\exp[\theta_E/T]-1)^2}$$ [4 20]

with $\theta_E = \dfrac{\hbar \omega}{k_B}$ being the Einstein temperature.

However the approach by Einstein is too simple The atoms form a system of coupled oscillators and do not vibrate independently of one another. So there is a frequency spectrum like that of an elastic continuum. The internal energy of such a system is then given by an integral of the vibration energy of each atom with respect to the spectrum of frequencies as given by the density of frequency modes $D(\omega)$ over the range of all permitted frequencies ω.

$$U = \int_{\omega} \hbar \omega D(\omega) f(\omega) d\omega,$$ [4.21]

where $f(\omega)$ is the Bose-Einstein distribution function

$$f(\omega) = \frac{1}{\exp[\beta \hbar \omega]-1}.$$ [4.22]

In order to obtain the internal energy the density of modes or states is required. The density of states per unit frequency range $D(\omega)d\omega$ is given by the number of k values between the frequencies ω and $\omega + d\omega$, where k is the wave vector of a permitted vibration or/and a point in the k space. To obtain this density $D(\omega)d\omega$ the volume of the shell d^3k between the surfaces $S(\omega)$ belonging to ω and $\omega + d\omega$ in the k space has to determined and to be divided by the volume of one k value (see figure 4.1.1).

$$D(\omega)d\omega = \frac{1}{\Delta^3 k} \oint_{\omega} d^3k$$ [4.23]

118

The volume d^3k is given by the product of the surface dS with the change in the k vector $d\mathbf{k}$ projected with the normal vector $\mathbf{n}$ in the direction which is perpendicular to the surface dS.

$$d^3k = dS\ \mathbf{n} \circ d\mathbf{k} \tag{4.24}$$

In equation [4 24] $d\mathbf{k}$ can expressed by

$$d\mathbf{k} = \frac{d\omega}{\nabla_k \omega} = \frac{d\omega}{|\nabla_k \omega| \mathbf{n}} = \frac{d\omega}{v_g \mathbf{n}}, \tag{4.25}$$

where $v_g = d\omega/dk$ is the group- or sound velocity. Thus the density of states becomes

$$D(\omega) = \frac{1}{\Delta^3 k} \oint_\omega \frac{dS}{v_g} = \frac{V}{8\pi^3 v_g} \oint_\omega dS. \tag{4.26}$$

If the propagation of waves in a solid is anisotropic then the shape of the surfaces has a complicated form and it is difficult to calculate the integral in equation [4.26]. In this case the relation between ω and k, the dispersion, is non-linear and the anisotropy of the dispersion increases with increasing frequency.
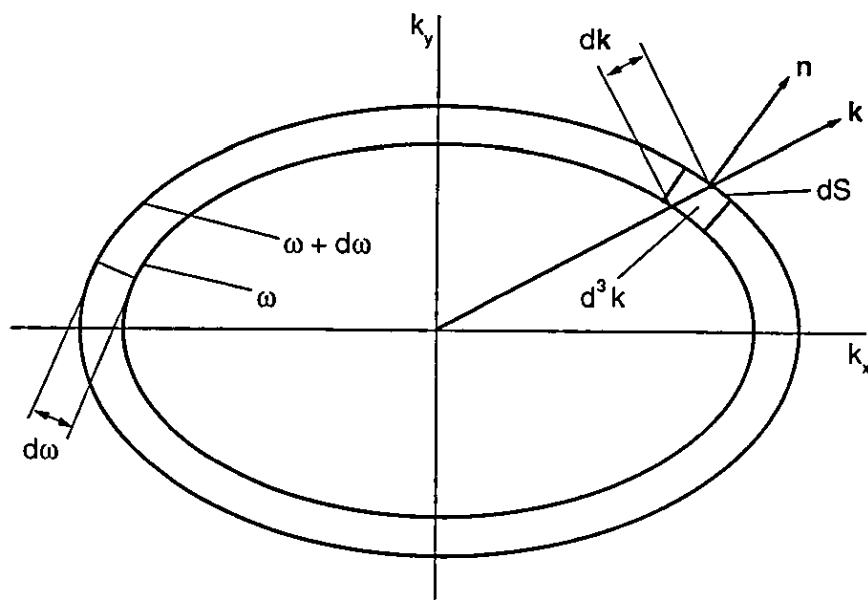
Figure 4 1 1   A shell and a small volume element d^3k of the k space bounded by surfaces of constant frequency ω and $\omega + d\omega$

Debye made the assumption that the dispersion is linear and isotropic.

$$\omega = v_g k \qquad\qquad [4\ 27]$$

resulting in

$$D(\omega) = \frac{V}{2\pi^2 v_g^3} \omega^2 \qquad\qquad [4.28]$$

In a solid one longitudinal and two transversal modes of vibration have to be considered and therefore equation [4 28] is converted to

$$D(\omega) = \frac{V}{2\pi^2} \left(\frac{1}{v_L^3} + \frac{2}{v_T^3} \right) \omega^2 \qquad\qquad [4.29]$$

Further, Debye neglected the difference between the sound velocities of longitudinal and transverse waves. Setting $v_L = v_T$ results in

$$D(\omega) = \frac{3V}{2\pi^2 v_0} \omega^2 \qquad\qquad [4.30]$$

The density of states depends on the square of the frequency. It increases up to the cut-off frequency ω_{max}. This maximum frequency can now be calculated by considered the integral of $D(\omega)d\omega$. This integral has to yield the total number of possible modes in the sample, namely

$$3N = \int_0^{\omega_{max}} D(\omega)d\omega = \frac{V}{2\pi^2 v_0^3}\omega_{max}^3 \qquad\qquad [4.31]$$

$$\omega_{max} = \omega_D = \left(\frac{6\pi^2 N v_0^3}{V}\right)^{\frac{1}{3}} \qquad\qquad [4 32]$$

This maximum frequency is called the Debye frequency ω_D. In figure 4 1.2 the density of states is shown as a function of frequency
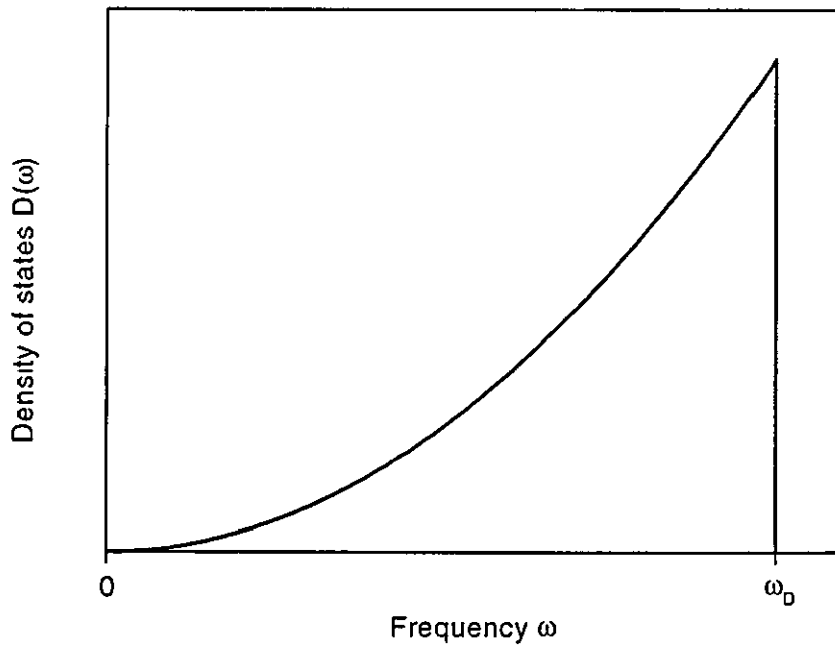
Figure 4 1 2 Density of states $D(\omega)$ as a function of frequency ω for the Debye solid (3-dimensional lattice) The axis are in arbitrary units

121

Using the density of states in equation [4.30] the internal energy (see equation [4.21]) is given by

$$U = \frac{3\hbar V}{2\pi^2 v_0^3} \int_0^{\omega_D} \frac{\omega^3}{\exp[\beta\hbar\omega]-1} d\omega$$

[4.33]

The specific heat is obtained by evaluating the derivative of U with respect to temperature.

$$C_V = \frac{3\hbar V}{2\pi^2 v_0^3} \int_0^{\omega_D} \frac{\hbar\omega}{k_B T^2} \frac{\omega^3 \exp[\beta\hbar\omega]}{(\exp[\beta\hbar\omega]-1)^2} d\omega$$

[4.34]

with substituting

$$z = \beta\hbar\omega = \frac{\hbar\omega}{k_B T}$$

[4.35]

and using the Debye temperature θ_D given by

$$\theta_D = \frac{\hbar\omega_D}{k_B} = \frac{\hbar}{k_B}\left(\frac{6\pi^2 N v_o^3}{V}\right)^{\frac{1}{3}}$$

[4.36]

it yields

$$C_V = \frac{9 N k_B}{\theta_D^3} T^3 \int_0^{\theta_D/T} \frac{z^4 \exp[z]}{(\exp[z]-1)^2} dz$$

[4 37]

For high temperatures ($k_B T \ll \hbar\omega$) the e-function in [4.33] can be expanded in a power series and the integral reduces to

$$\frac{1}{3}\frac{k_B T}{\hbar}\omega_D^3 = \frac{1}{3}\frac{k_B T}{\hbar}\frac{6\pi^2 N v_o^3}{V}.$$

[4.38]

Substituting equation [4 38] in [4 33] gives the internal energy

$$U = 3 N k_B T$$

[4.39]

which is the classical result by Dulong and Petit. Thus the specific heat at high temperatures has the constant value of

$$C_V = 3Nk_B.$$ [4.40]

At high temperatures all frequency modes are excited and the Debye frequency and Debye temperature constitute the upper bounds.

At low temperatures $(T \ll \theta_D, \omega \ll \omega_D)$ only the modes below $k_B T$ with frequencies below ω are excited and thus the temperature T may be seen as the "soft cut-off" temperature. Therefore the upper boundary in the integral in [4.33] can be chosen as infinity and with substituting equation [4.35] and the Debye temperature θ_D the internal energy becomes

$$U = \frac{3\hbar V}{2\pi^2 v_0^3} \frac{k_B^4 T^4}{\hbar^4} \int_0^\infty \frac{z^3}{\exp[z]-1} dz = \frac{3\hbar V}{2\pi^2 v_0^3} \frac{k_B^4 T^4}{\hbar^4} \frac{\pi^4}{15} = \frac{3Nk_B \pi^4}{5\theta_D^3} T^4$$

[4.41]

and the specific heat is obtained as

$$C_V = \frac{12Nk_B \pi^4}{5\theta_D^3} T^3.$$ [4.42]

Consequently the specific heat for a solid at low temperatures $(T \approx \theta_D/10)$ is given by the Debye law

$$C_V \propto T^3.$$ [4 43]

The Debye interpolation has been found to represent the specific heat of most solids with some success. Despite having some weaknesses the Debye model represents the specific heat of most solids well and has been widely used for the interpretation of experimental data.

Electronic contribution to the specific heat

The electronic contribution to the specific heat is defined by equation [4.5]

$$C_V = \left(\frac{\partial E}{\partial T}\right)_V,$$ [4 44]

where the energy E the energy of the electrons in the solid.

An explanation of metallic behaviour has been attempted by Paul Drude in terms of a classical electron gas. If the electrons are independent classical particles then the law of equipartition of energy applies and each electron has the energy of

$$\varepsilon = \frac{3}{2}k_B T.$$ [4.45]

Therefore the specific heat has a constant temperature independent value of

$$C_V = \frac{3}{2}N k_B$$ [4.46]

Where N is the number of electrons in the metal.

This value is half of the specific heat of lattice vibrations [4.40]. For metallic samples where the number of electrons and atoms are the same. Therefore, the measured specific heat should increase by 50 % compared to a non-conducting sample. This has not been observed experimentally. The electronic specific heat in metals in actually very small and it depends on temperature.

In analogy to the discussion of the lattice contribution the energy of the electron gas has to be considered by an integral of the energy of one electron ε, the density of energy states $D(\varepsilon)$ and a distribution function over the range of all permitted energies $f(\varepsilon)$.

$$E = \int_{\varepsilon} \varepsilon\, D(\varepsilon) f(\varepsilon) d\varepsilon$$ [4.47]

The difference to phonons is that electrons are fermions and therefore the Pauli exclusion principle has to be considered. The distribution function of particles like electrons is then the Fermi-Dirac distribution function

$$f(\varepsilon) = \frac{1}{\exp[\beta(\varepsilon - \mu)] + 1}$$

[4.48]

where μ is the chemical potential.

Electrons in a metal have kinetic and potential energy. For the present consider a free electron gas. The total energy of the gas is equal to the kinetic energy of all electrons.

$$\varepsilon = \frac{m_e}{2} v^2 = \frac{p^2}{2m_e}$$

[4.49]

where $p = m_e v$ is the linear momentum and v the velocity.

In quantum mechanics a particle can be described using a wave function and applying the rule due to de Broglie, namely that each electron is related to a wave with a wave vector

$$\mathbf{k} = \frac{\mathbf{p}}{\hbar}$$

[4.50]

and the energy of one electron can be written as

$$\varepsilon = \frac{\hbar^2 k^2}{2m_e}.$$

[4.51]

The density of energy states per unit energy range is given by the volume between the surfaces of constant ε and $\varepsilon + d\varepsilon$ multiplied with the factor of two, because each energy sate can be occupied by two electrons with their spins either up or down.

$$D(\varepsilon)d\varepsilon = 2\frac{1}{\Delta^3 k}\oint_\varepsilon d^3 k = 2\frac{V}{(2\pi)^3}\oint_\varepsilon dS\, \mathbf{n}\, d\mathbf{k} \qquad [4.52]$$

For a free electron gas the surfaces of equal energy are spherical and thus

$$D(\varepsilon)d\varepsilon = 2\frac{V}{(2\pi)^3}\oint_k dS\, dk = 2\frac{V}{8\pi^3}4\pi\, k^2\, dk\,. \qquad [4.53]$$

Substituting equation [4.51] yields

$$D(\varepsilon) = \frac{V}{2\pi}\left(\frac{2m_e}{\hbar^2}\right)^{\frac{3}{2}}\sqrt{\varepsilon} \qquad [4.54]$$

With the obtained density of states the total energy at zero temperature can be evaluated as

$$E = \frac{V}{2\pi^2}\left(\frac{2m_e}{\hbar^2}\right)^{\frac{3}{2}}\int_0^{\varepsilon_F}\varepsilon^{3/2}\frac{1}{\exp\left[(\varepsilon-\varepsilon_F)/k_B T\right]+1}d\varepsilon\,. \qquad [4.55]$$

Using the Fermi energy

$$\varepsilon_F = \left(\frac{3\pi^2 N}{V}\right)^{\frac{2}{3}}\frac{\hbar^2}{2m_e} \qquad [4.56]$$

equation [4.55] can be expressed as

$$E(T=0) = \frac{3N}{5}\varepsilon_F\,. \qquad [4.57]$$

Thus there is an average energy of $3\varepsilon_F/5$ per atom without any thermal excitations.

At finite temperatures the total energy is given by

$$E = \frac{V}{2\pi^2}\left(\frac{2m_e}{\hbar^2}\right)^{\frac{3}{2}}\int_0^{\infty}\varepsilon^{3/2}\frac{1}{\exp\left[\varepsilon-\varepsilon_F/k_B T\right]+1}d\varepsilon \qquad [4.58]$$

The approximate solution of equation [4.58] for low temperatures ($T \ll \varepsilon_F / k_B$) is

$$E \approx \frac{V}{5\pi^2}\left(\frac{2m_e}{\hbar^2}\right)^{\frac{3}{2}}\varepsilon_F\left(1+\frac{5}{24}\left(\frac{\pi k_B T}{\varepsilon_F}\right)^2\right)$$

[4.59]

And thus the contribution of the specific heat by electrons is

$$C_V = \frac{\pi^2 N k_B T}{2\varepsilon_F},$$

[4.60]

which results in

$$C_V = \frac{\pi^2}{3}k_B^2 D(\varepsilon)T.$$

[4 61]

The specific heat of the electron gas is therefore a linear function of temperature The total specific heat including the electronic and Debye terms can be written as

$$C_V = \frac{\pi^2}{3}k_B^2 D(\varepsilon)T + \frac{12 N k_B \pi^4}{\theta^3}T^3$$

[4 62]

and may be expressed as

$$C_V = \gamma T + \alpha T^3,$$

[4 63]

where α is the phonon and γ the electronic coefficient [1]

Plotting experimental data in the form of C_p/T versus T^2 a straight line is obtained and the two contributions can be isolated and by the determination of the intersection of the straight line with the y-axis (γ) and its slope (α).

---

[1] Usually the greek letter β is used for the phonon coefficient, but this letter β will be used later for another expression In order to not confuse the reader here the letter α has been chosen

Magnetic contribution to the specific heat

As discussed in chapter 3 in section 3.1 electrons fill energy levels belonging to energy shells of an atom and magnetism arises due to incompletely filled energy shells. For the case of rare-earth alloys the $4f$ shell is partially filled. The $4f$-electron shell is located well within the 5s and 5p energy shells and consequently the $4f$-electrons of the rare-earth atoms do not contribute to the conduction band. Thus the magnetism of the rare-earth alloys is well represented by a localised moment model. The magnetic contribution to the specific heat is therefore related to the alignment of the magnetic moments and thus to the magnetic degrees of freedom. Therefore, the magnetic specific heat is associated with the entropy S of a system.

$$C_{mag} = T \left(\frac{\partial S}{\partial T} \right)_B .$$
[4.64]

The change in the internal order of a magnetic material as it passes through the transition temperature may be clearly displayed in measurements of the specific heat as a function of temperature The sharp peak at the transition temperature is typical of a second order thermodynamic phase transition and is associated with the disappearance of long-range magnetic order. The small contribution of the magnetic specific heat just above the transition temperature arises from the presence of residual short-range magnetic order.

The change in entropy of the magnetic state is given by

$$\Delta S_{mag}(T) = \int_0^T \frac{C_{mag}(\tilde{T})}{\tilde{T}} d\tilde{T}$$
[4 65]

and can be obtained from experimental measurements. Furthermore this entropy is directly related to the quantum number J of the magnetic atoms.

$$\Delta S^{sat} = c k_B N_A \ln[2J + 1],$$
[4.66]

where c is the number of magnetic atoms per unit cell present carrying the magnetic moment and N_A the Avogadro constant.

The total integral of the magnetic contribution to the specific heat is proportional to ln[2J+1]. This assumes that the entropy of the ground state is equal to zero (i e. that there in are unique state) and that the temperature integration is carried out such that all CEF contributions an incorporated.

4.2 Description of Specific Heat Measurement Apparatus

Adiabatic calorimetry

For the measurements of the specific heat the method of adiabatic calorimetry was used. This continuous method involves injecting a known quantity of input energy into the sample and measuring its response in terms of a temperature rise. The energy input is supplied at constant power and the temperature of the sample is measured as a function of time before the heat pulse and after the heat pulse is applied. The specific heat is derived from the ratio of the heat input ΔQ to the temperature rise ΔT.

$$C_p = \frac{\Delta Q}{\Delta T} \qquad [4.67]$$

However, a true adiabatic condition is not achievable experimentally, especially at low temperatures where the specific heat is very low. Furthermore, this continuous method suffers from the disadvantage of not allowing the characterisation of a heat loss from the sample. The heat flow from the sample system can be estimated by observing the sample temperature before and after the heating period (pre- and post drift). This can be incorporated into the calculation of the temperature change. An advantage is that the time which is required to reach equilibrium is not a limiting factor and thus relatively large samples can be measured. A sketch of the time dependence of the sample temperature for the heat pulse method is shown in figure 4 2.1.

The calorimeter consists of a sapphire disc of thickness 0.5mm, which is suspended within a copper ring using a thin cotton thread. On the bottom side of the disk a thin film substrate of chromium has been evaporated. This film acts as the sample heater. The sample was placed on the disk above the heater and fixed with a small amount of Apiezon N-type grease (ca. 4mg). A low mass Cernox temperature sensor was attached to the bottom side of the disk and used to measure the temperature of the sample. The ensemble is situated within two copper radiation shields to minimise the thermal response time. The outer shield is a copper can onto which a copper wire has been wound to act as a shield heater. The shield temperature was measured using a carbon glass thermometer. This outer shield is again placed into a vacuum can manufactured using stainless steel in order to isolate the calorimeter from the liquid helium. To minimise the heat flow the sample space was evacuated down to pressures of approximately 10^{-6} mbar using a diffusing pump, backed by a rotary pump. A cross-section of the vacuum can is shown in figure 4.2.4.
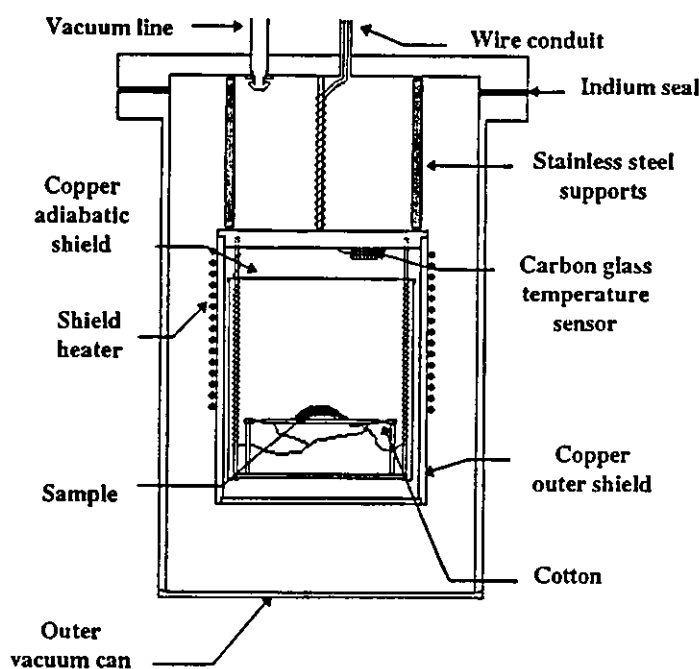

Figure 4 2 4   Cross-section of the vacuum can and the calorimeter [Parson, PhD Thesis]

Due to the time constants involved in achieving thermal equilibrium it was necessary to automate the calorimeter. The automation was based on a computer with a pentium processor communicating to the temperature controller, a DVM and a current source using an IEEE-488 interface bus. The original software was written by M. Parsons, J. Taylor and B. Dennis [Parson, PhD Thesis] using Microsoft Quick Basic version 4. The software program consists of three parts: the preparation phase, where the communications, the experimental run parameters and the temperature are being set up, the measurement phase and the analysis phase.

If within the preparation phase the temperature is stable then the second phase of the measurement starts. This phase consist of four time regions: pre-drift, sample heating, delay and post-drift. During the pre-drift period the sample temperature is measured every 1 - 4 seconds. After the sample heating phase is started the system circles in a loop measuring the current through the sample heater and the voltage. The current is provided by a constant current source, made in-house When the heating of the sample is finished the system waits for a predetermined time, the delay time. The delay is implemented to allow the sample to reach thermal equilibrium. The next phase is the post-drift routine, which follows the same procedure as in the pre-drift routine.

The analysis phase calculates the input energy ΔQ the temperature rise ΔT, and finally the specific heat of the sample C_p. The energy input is calculated by averaging the sample heater current and heater voltage, by taking the product of current and voltage and by using Simpson's rule to integrate the heating power as a function of time. In order to obtain the temperature rise both the pre- and post-drift curves are subject to a least squares linear regression and extrapolated to the time at the middle of the heating phase. At this intersection point ΔT is calculated. Finally the specific heat is calculated in units of [J / K mol] by equation [4.67] and a correction factor (addenda) is subtracted

The correction factor (addenda) contains the specific heat of the sample holder and the grease To obtain the addenda a measurement of the calorimeter without

a sample was carried out and fitted to a polynomial equation. The addenda and the obtained polynomial fit are shown in figure 4.2.5. The deviation of the measured data from the fitted curve yields a percentage error of the addenda specific heat. This is combined with the errors involved in the measurement process such as the temperature, current, and voltage. The largest relative error of the addenda occurs at low temperatures, but the specific heat of the addenda is so small that the errors will have a negligible effect on the total error. However, at high temperatures the specific heat of the addenda becomes a large fraction of the total specific heat and thus the uncertainty in the addenda becomes more important. Also the errors in temperature (thermometer) and in the heater current become larger. Therefore, the total error increases with increasing temperature.
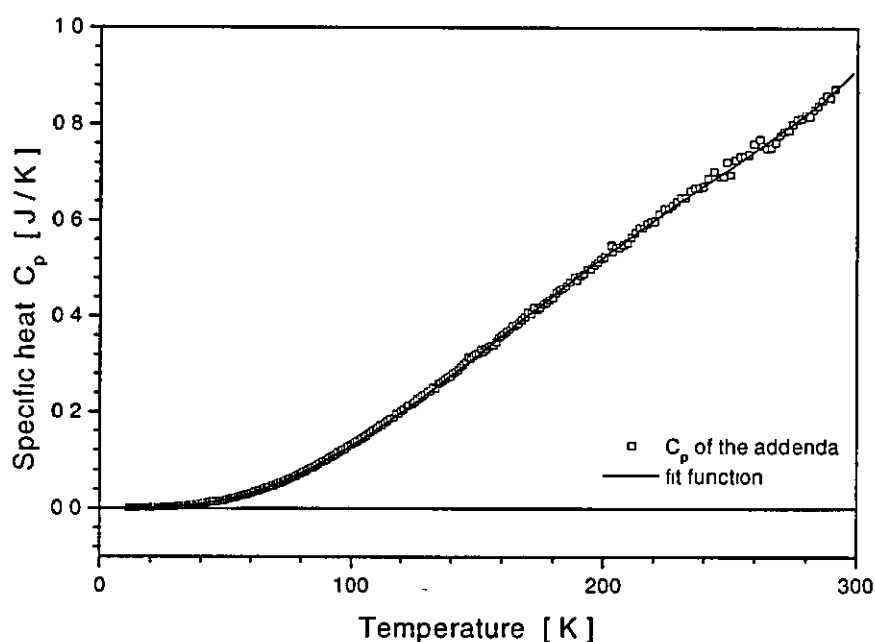

Figure 4 2 5 Specific heat of the addenda (sample holder and grease) The solid line indicates the fit function to the specific heat of the addenda

135

4.3 Experimental Results

Experimental work

From the long ingot of each compound (molten in the argon-arc furnace and annealed afterwards) a small piece was cut using a spark eroder. In order to ensure good thermal contact to the disc in the calorimeter the flat side of this small piece has been polish to a flat and smooth surface. The sample was placed on the sapphire disc with the flat side down using Apiezon grease. The chamber of the calorimeter was evacuate over one day to a vacuum of at least $1 \cdot 10^{-6}$ mbar. When this vacuum was reached the chamber was placed into the cryostat and the system was cooled down to 4.2 Kelvin using liquid nitrogen and helium.

The measurement of the specific heat as a function of temperature has been carried out in temperature steps of less then 1 Kelvin in a temperature range from 4 2 Kelvin to room temperature. In table 4 3.1 some sample details are given

Sample	Weight [g]	Relative atomic mass [g/mol]	Number of mole [mol]
$La_{14}Ag_{51}$	$1.2343 \pm 0\ 0001$	7445 945	$(1\ 658 \pm 0\ 001)\ 10^{-4}$
$Gd_{14}Ag_{51}$	$1\ 2011 \pm 0\ 0001$	7702.87	$(1\ 559 \pm 0.001)\ 10^{-4}$
$Tb_{14}Ag_{51}$	$1\ 3076 \pm 0\ 0001$	7726.32	$(1\ 692 \pm 0.001)\ 10^{-4}$
$Dy_{14}Ag_{51}$	$1\ 0471 \pm 0\ 0001$	7776 37	$(1\ 347 \pm 0\ 001)\ 10^{-4}$
$Ho_{14}Ag_{51}$	$1\ 2249 \pm 0\ 0001$	7810 39	$(1\ 568 \pm 0\ 001)\ 10^{-4}$
$Er_{14}Ag_{51}$	$1.3900 \pm 0\ 0001$	7843 01	$(1.772 \pm 0\ 001)\ 10^{-4}$

Table 4 3 1: Weight, relative atomic mass and number of moles of $RE_{14}Ag_{51}$ compounds used for the specific heat measurements

The compound La$_{14}$Ag$_{51}$

The La$_{14}$Ag$_{51}$ alloy is the non-magnetic reference compound. The specific heat of this intermetallic compound contains only a contribution of the lattice and the electrons. Therefore this sample was used as the phonon blank.

A measurement of specific heat as a function of temperature was carried out and is shown in figure 4.3.1. In order to use the specific heat of the phonon blank as a reference for the magnetic compounds (Gd$_{14}$Ag$_{51}$, Tb$_{14}$Ag$_{51}$, ...) several fit-functions have been employed to model the data of the specific heat. The fit-function is shown in figure 4.3.1. It has to be mentioned that the error of this fit-function (due to the variation of the data in the specific heat of La$_{14}$Ag$_{51}$) is relative large and increases drastically with increasing values of the specific heat At temperatures above 100 Kelvin the error amounts to 5%
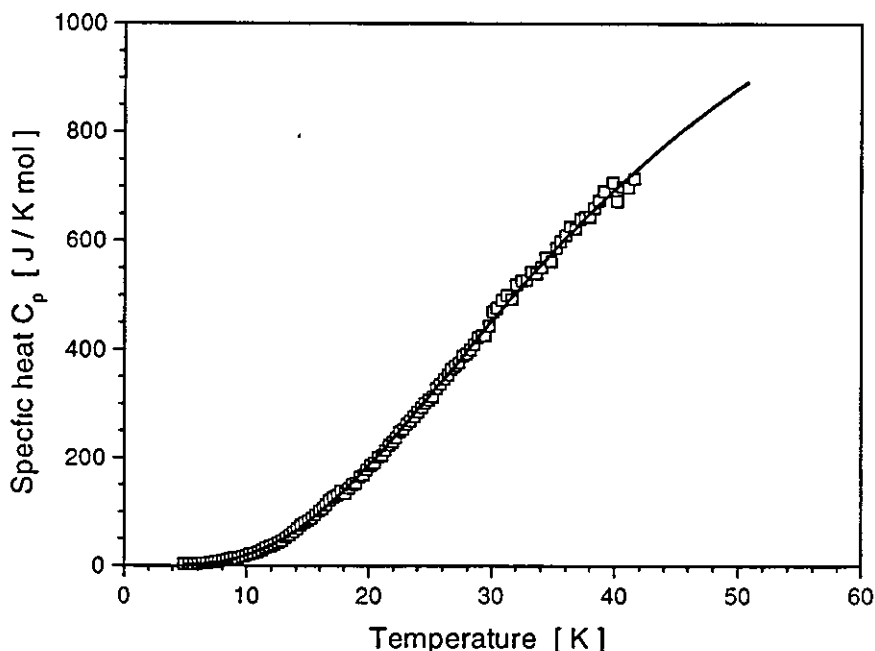

Figure 4 3 1. Molar specific heat as a function of temperature for La$_{14}$Ag$_{51}$ The solid line indicates the fit

In the Debye model the specific heat can be written as $C_V = \gamma T + \alpha T^3$, where α is the phonon and γ electronic coefficient (see equation [4.63]) Plotting C_V / T as a function of T^2 should result in a straight line at low temperatures, with the intersection point with the C_V / T-axis yields the γ value and the slope α the Debye temperature θ_D. The plot of C_V / T versus T^2 and a fit to the data at low temperatures is shown in figure 4.3.2. A more detailed presentation of the same plot is shown in figure 4.3.3.
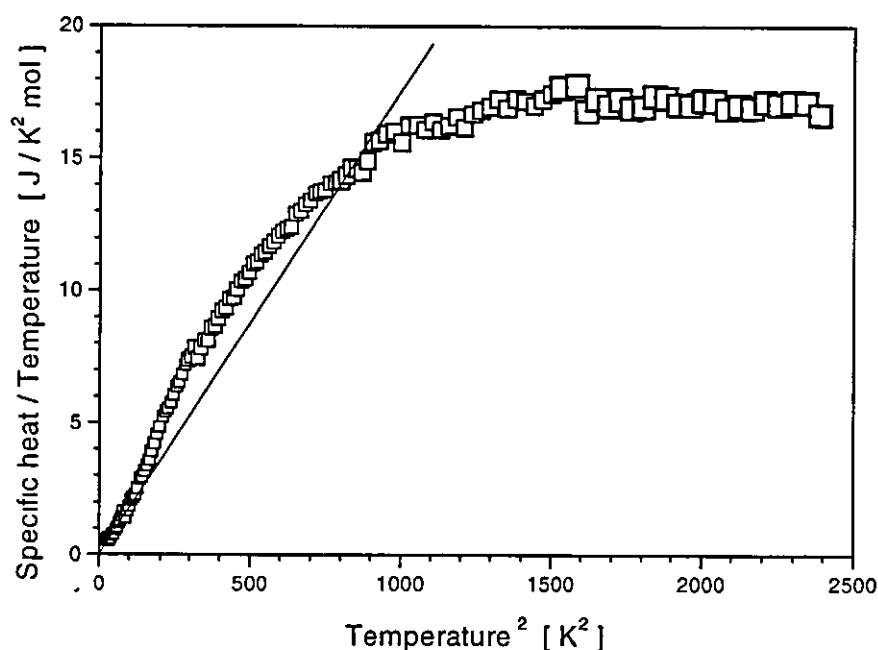

Figure 4 3 2 C_V / T as a function of T^2 for $La_{14}Ag_{51}$ The solid line indicates a linear fit to the data at low temperatures
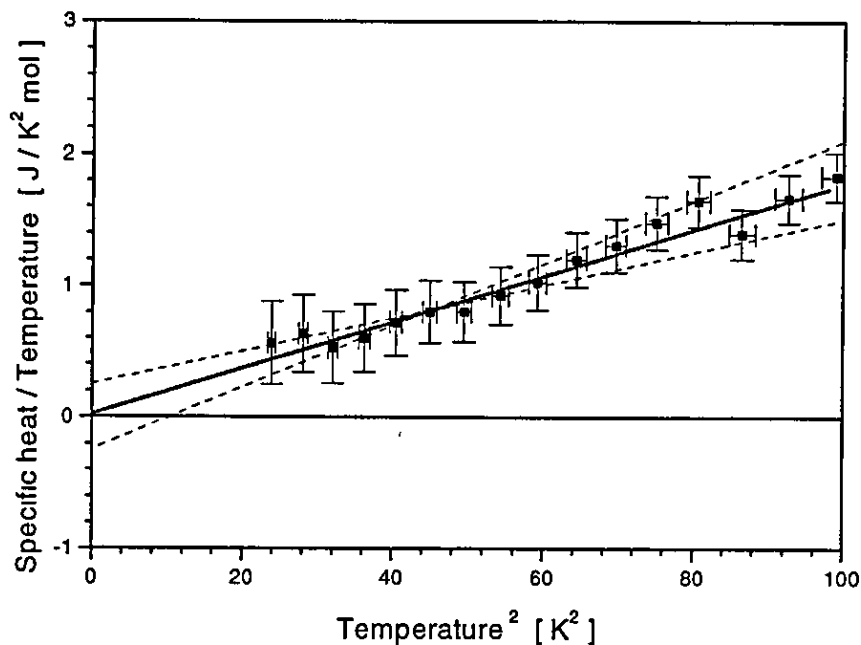
Figure 4 3 3· C_V/T *as a function of* T^2 *for* $La_{14}Ag_{51}$ *at low temperatures. The solid line indicates a linear fit to the data and the dashed lines the error of this fit*

From figures 4.3.2 and 4.3.3 a linear fit C_V/T as a function on T^2 can be seen to represent the data at low temperatures (below 10 Kelvin). Up to ~30 Kelvin the gradient of the plot is weakly temperature dependent. Evaluating the linear fit to the data below 10 K (see figure 4.3.3) a γ value of $\gamma = (20 \pm 80) \cdot$mJ/K^{2}mol and a Debye temperature of $\theta_D = (193 \pm 5)$ K is obtained. The γ value is directly related to the density of states at the Fermi surface (see equation [4 61]) given by

$$\gamma = \frac{\pi^2}{3} k_B^2 D(\varepsilon) , \qquad [4.68]$$

which yields an estimated value of the density of states per formula unit and eV of

$$D(\varepsilon_F) \approx 8.5 \text{ states / f.u eV}. \qquad [4.69]$$

139

According to the relatively large error of the experimental γ value this value is in fair agreement with the value of 32 states / f.u eV obtained from the magnetisation measurements (see [3.118]).

The value for the Debye temperature θ_D obtained for $La_{14}Ag_{51}$ have to be compared to literature values of Lanthanum $\theta_D = 132$ K and Silver $\theta_D = 215$ K [12]. The value of (193 ± 5) K is within the range of θ_D values for the constituent elements

In summary, $La_{14}Ag_{51}$ has a specific heat which is characterised by a relatively low γ value of

$$\gamma = (20 \pm 80) \ mJ/K^2 mol$$

and a Debye temperature of

$$\theta_D = (193 \pm 5) \ K.$$

These contributions to the specific heat are taken to represent the electronic and lattice contribution for the magnetic compounds. This is a valid procedure if the various subsystems of magnetic, lattice and electronic subsystem are not coupled. If such an assumption is applicable then it is possible to use the estimates obtained by the $La_{14}Ag_{51}$ specific heat measurement also for the other $RE_{14}Ag_{51}$ samples. The validity of such a procedure will be discussed more fully below.

The alloy $Gd_{14}Ag_{51}$

The specific heat of $Gd_{14}Ag_{51}$ was measured in a temperature range of ~4 Kelvin to 300 Kelvin. The specific heat of this compound is shown in figure 4.3.4. From the graph in figure 4.3 4 it can be seen that the specific heat increases continually as a function of temperature up to a distinct anomaly at 34 Kelvin. Then the graph is rapidly decreasing to a minimum and again increasing up to 300 Kelvin

without any sign of saturation. The peak in the specific heat indicates an antiferromagnetic phase transition occurring at T_N ~36 Kelvin in zero-field. The obtained value of the Néel temperature of T_N = (36 ± 1) Kelvin is equal to, within the error bars, the value given by the magnetisation measurements of T_N = (36.7 ± 0.1) Kelvin.
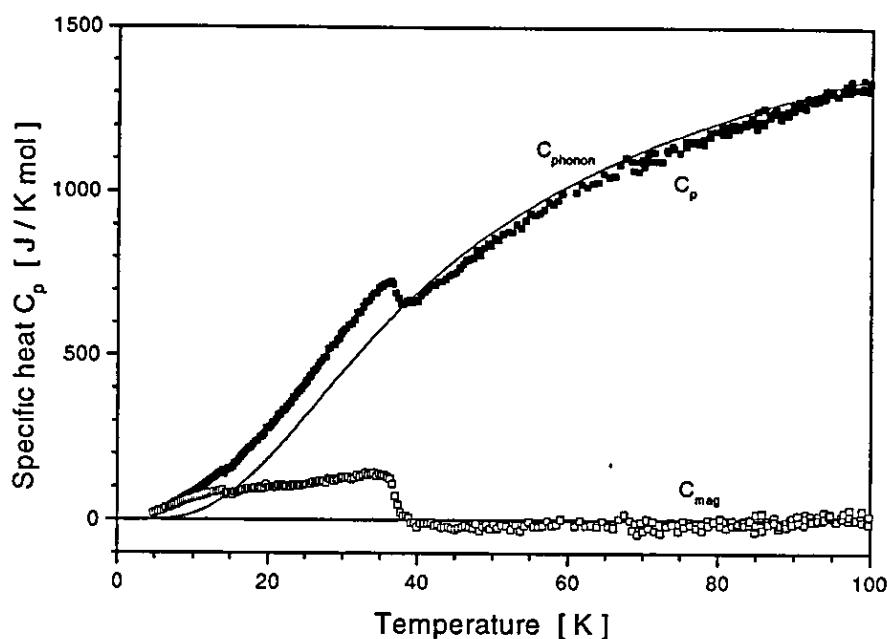

Figure 4.3 4· Molar specific heat C_p of $Gd_{14}Ag_{51}$ as a function of temperature (solid dots) The specific heat of $La_{14}Ag_{51}$, the non-magnetic reference compound, is represented by the fit-function as shown by a solid line The magnetic specific heat C_{mag} of $Gd_{14}Ag_{51}$ is shown by open dots

Comparing the specific heat of $Gd_{14}Ag_{51}$ to the measurement of the non-magnetic compound $La_{14}Ag_{51}$ (represented by a solid line in figure 4.3.4) reveals that $Gd_{14}Ag_{51}$ has a larger specific heat than $La_{14}Ag_{51}$ below T_N and slightly smaller values above the Néel temperature. Above approximately 100 Kelvin the specific heats of both compounds are identical.

The initial analysis of the specific heat of $Gd_{14}Ag_{51}$ has been carried out assuming the specific heat to be compound of three separate contributions

originating from the lattice C_{latt}, the conduction electrons C_{elec}, and the magnetic moments of the rare earth atoms C_{mag}. Thus the specific heat C_p can be written as

$$C_p = C_{latt} + C_{elec} + C_{mag}. \qquad [4.70]$$

This functional form of the equation [4.70] assumes that the three contributions are distinct and there is no coupling between the various subsystems. Only the sum of all contributions is measured experimentally and an unambiguous separation of the total specific heat into the constituent parts, as given by equation [4.70], is not possible. However, the subtraction of the lattice and conduction electron contributions, obtained above for the $La_{14}Ag_{51}$ compound, from the specific heat of $Gd_{14}Ag_{51}$ should yield, in principle, the magnetic contribution C_{mag} (see figure 4.3.4). A more detailed picture of the magnetic specific heat is shown in figure 4.3.5.

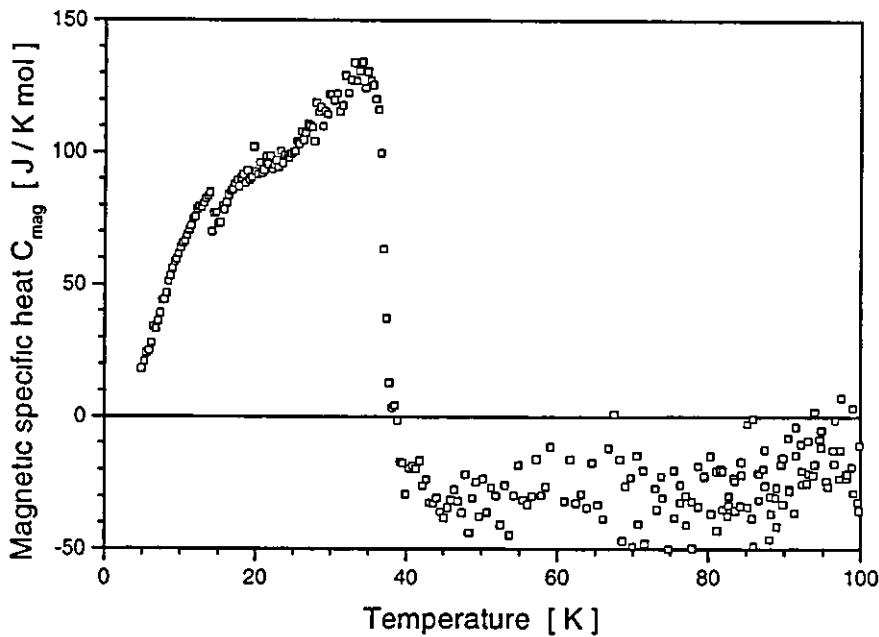*Figure 4 3.5: Magnetic contribution C_{mag} to the specific heat of $Gd_{14}Ag_{51}$ as a function of temperature.*

The graph of the magnetic specific heat in figure 4.3.5 clearly exhibit a second bump at a temperature (14 ± 1) Kelvin. This bump indicates the first phase

transition at T_1 observed in the magnetisation measurements at $T_1 = (13\ 6 \pm 0.2)$ Kelvin. From this figure it can also be seen that the magnetic specific heat of $Gd_{14}Ag_{51}$ increases with increasing temperature up to 36 Kelvin and then decreases abruptly. The graph of the specific heat at low temperatures has been extrapolated to zero-temperature in order to estimate the contribution to the magnetic entropy below the lowest experimental temperature.

As explained in section 4.1 the magnetic specific heat is attributed to the magnetic entropy as given by (see equation [4.66])

$$\Delta S_{mag}(T) = \int_0^T \frac{C_{mag}(\tilde{T})}{\tilde{T}} d\tilde{T} .$$

[4.71]

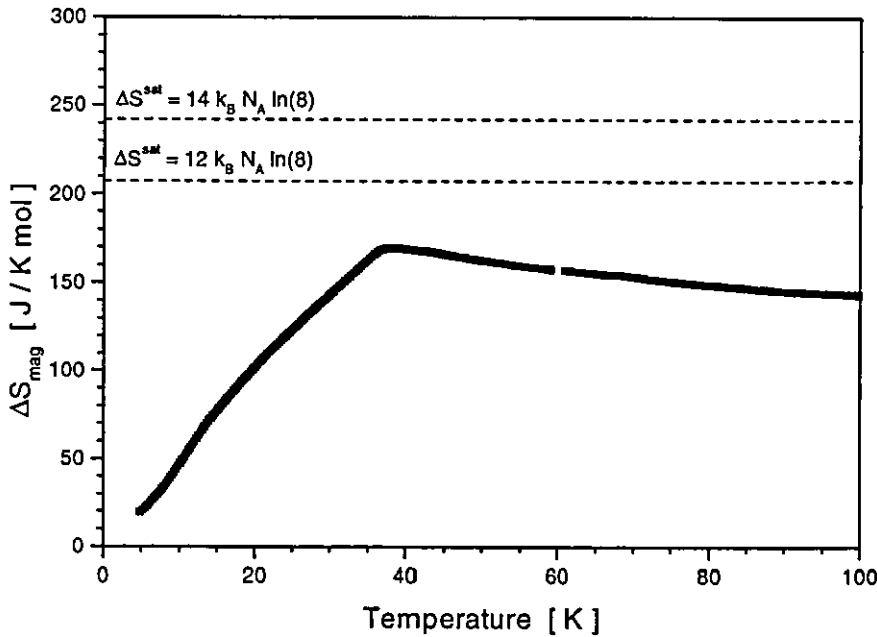The thermal dependence of the magnetic entropy ΔS_{mag} is illustrated in figure 4.3.6.

Figure 4 3 6· The magnetic entropy of $Gd_{14}Ag_{51}$ as a function of temperature obtained from the magnetic specific heat The dashed lines indicate the entropy by $\Delta S^{sat} = 14\ k_B N_A\ ln(8)$ and $\Delta S^{sat} = 12\ k_B N_A\ ln(8)$

143

From figure 4 3 6 it can be seen that the entropy increases rather linearly as a function of temperature to a maximum at ~40 Kelvin. Above 40 Kelvin the entropy decreases a little and reaches a constant level at 100 Kelvin. The reason for this unusual decrease is due to negative values of the magnetic specific heat above ~40 Kelvin.

The magnetic entropy as given in equation [4 65]/[4.71] and [4.66] is related to the spin degrees of freedom (2 S + 1), by

$$\Delta S^{sat} = c\,k_B\,N_A \ln[2S+1],\qquad\qquad [4.72]$$

where c is the number of magnetic atoms per unit cell carrying a magnetic moment and N_A the Avogadro constant (for Gadolinium J = S).

For Gadolinium with S = 7/2, a value for (2·S + 1) 8 is obtained and thus the magnetic entropy for one mole of $Gd_{14}Ag_{51}$ is given by $\Delta S^{sat} = 14\ k_B N_A \cdot \ln(8)$. This value is represented by a dashed line in figure 4.3.6. Since there are no contributions from crystal fields splitting effects, the full magnetic entropy of this value is expected to be obtained within a few degrees of the phase transition temperature. In figure 4.3.6 it is seen that the experimental values of the entropy does not reach this value. The measured value is ~20% smaller than the theoretical value. Also under the assumption that only 12 rare earth atoms contributed to the magnetic entropy, i.e. $\Delta S^{sat} = 12\ k_B N_A \cdot \ln(8)$, the saturation value is not reached. The assumption that only 12 rare earth atoms affect the magnetic behaviour is attributed to the hexagonal crystallographic structure of the compound, described in chapter 2

The alloy $Tb_{14}Ag_{51}$

In figure 4 3.7 the total specific heat C_p of $Tb_{14}Ag_{51}$ is shown as a function of temperature and the electronic and lattice contribution to the specific heat C_{phonon} is indicated by the full line. The difference between C_p and the fit-function, i.e. the magnetic contribution, is shown in figure 4.3.7.
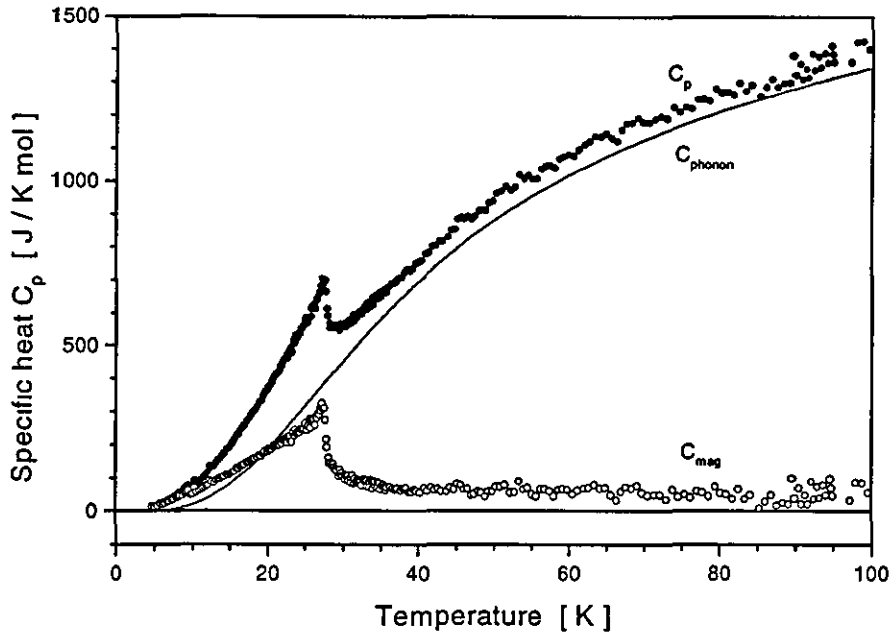
144

Figure 4 3.7: Molar specific heat C_p of $Tb_{14}Ag_{51}$ as a function of temperature (solid dots) The solid line indicates the phonon blank C_{phonon}. The magnetic specific heat C_{mag} is shown by open dots

In figure 4.3.7 one phase transition is observed, indicated by a peak at $T_N = (27.3 \pm 0.5)$ K. The transition temperature T_N obtained by magnetisation measurements is (27.8 ± 0.1) Kelvin. In figure 4.3.8 the magnetic specific heat is shown in more detail In this figure it is seen that the specific heat of the magnetic contribution has a sharp peak at T_N. However, it does not decrease to values around zero for temperatures above T_N. At 100 Kelvin C_{mag} has still a value of ~50 J/K mol. This "offset" results in a continued increase above T_N of the magnetic entropy as illustrated in figure 4.3 9.
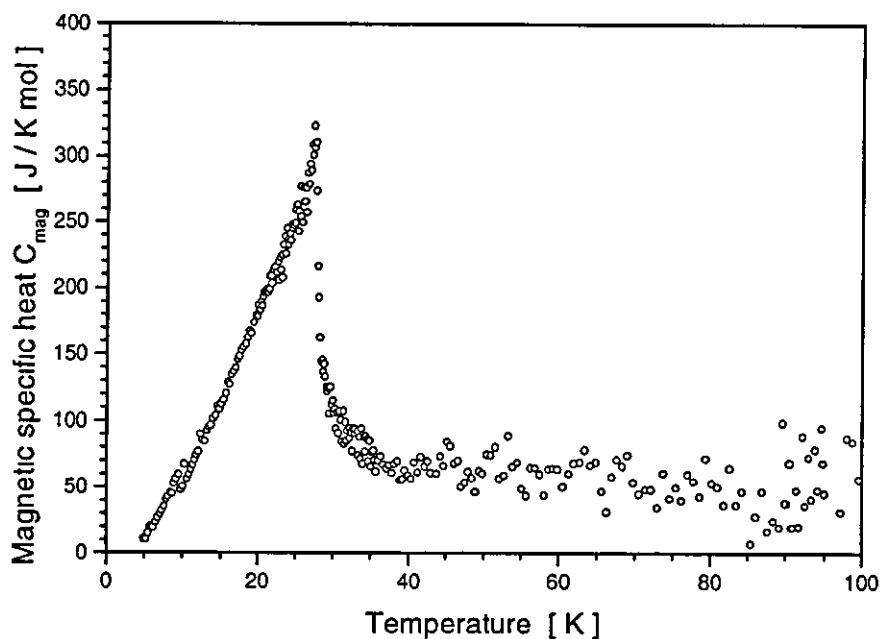
Figure 4 3 8· Magnetic specific heat as a function of temperature of $Tb_{14}Ag_{51}$
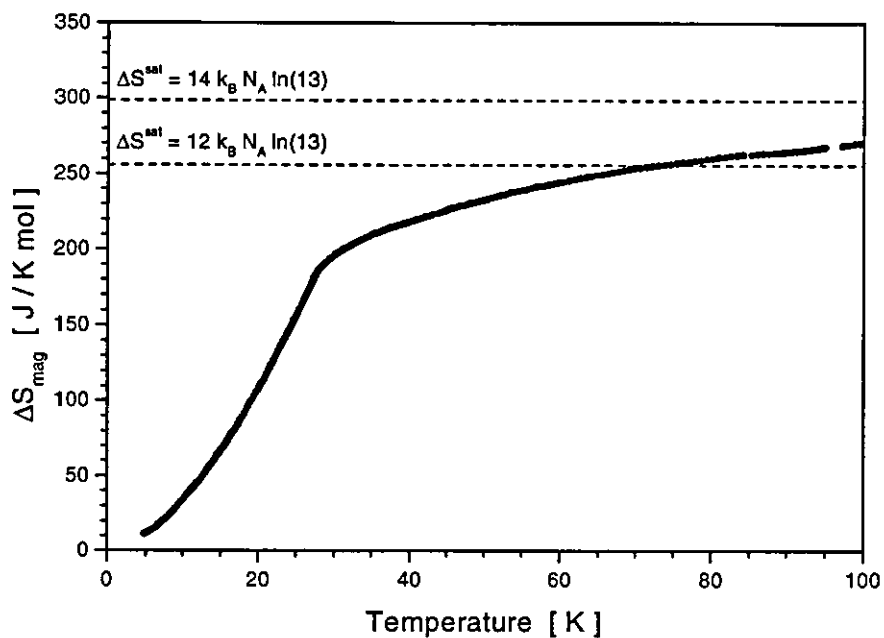

Figure 4 3 9· Magnetic entropy as a function of temperature of $Tb_{14}Ag_{51}$ The dashed lines indicates the values expected for the magnetic specific heat considering the contribution of either 14 or 12 Terbium atoms per unit cell

In figure 4.3.9 the theoretical values for the magnetic entropy is shown for the Terbium compound with a total angular momentum J of J = 6 and $\Delta S^{sat} = 14\ k_B N_A \cdot \ln(13)$ for 14 and $\Delta S^{sat} = 12 \cdot k_B N_A \cdot \ln(13)$ for 12 Terbium atoms per unit cell. Both entropy levels are not reached at the transition temperature.

The alloy $Dy_{14}Ag_{51}$

The specific heat C_p of the alloy $Dy_{14}Ag_{51}$ has been determined as a function of temperature and is shown in figure 4.3.10 together with the phonon contribution C_{phonon} and the magnetic specific heat C_{mag} obtained by subtracting the $La_{14}Ag_{51}$-specific heat values. A more detailed plot of C_{mag} is shown in figure 4.3.11.
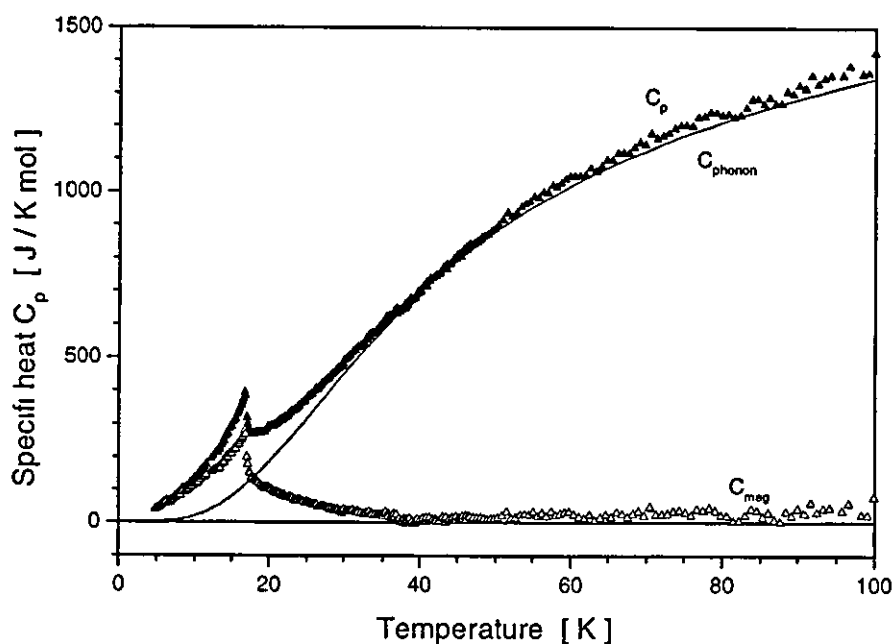
Figure 4 3 10: Specific heat C_p, phonon contribution C_{phonon} and magnetic specific heat C_{mag} of $Dy_{14}Ag_{51}$ as a function of temperature.
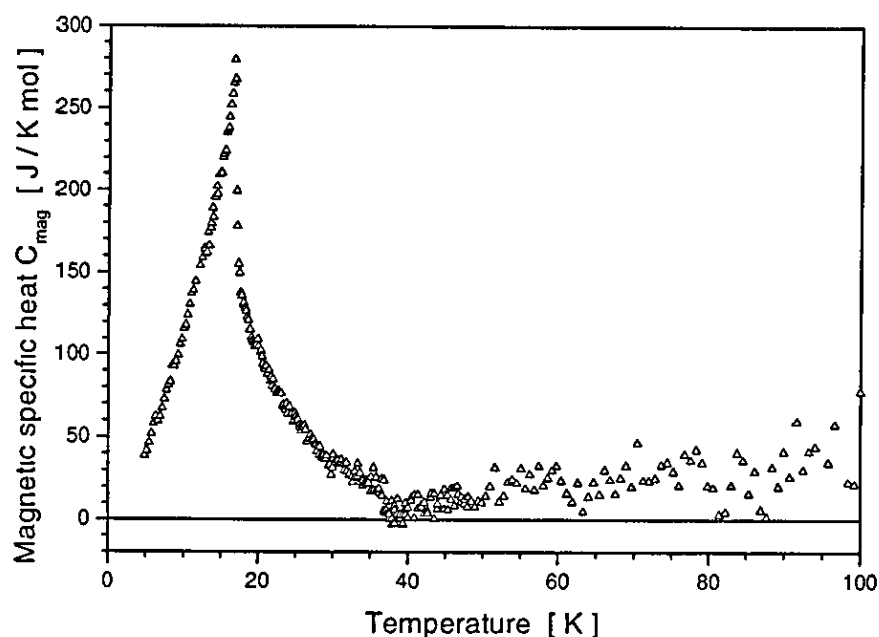
Figure 4 3 11   Magnetic specific heat of $Dy_{14}Ag_{51}$ *as a function of temperature*

Form the specific heat measurement of $Dy_{14}Ag_{51}$ (see figure 4.3.11) one phase transition has been observed at (17.0 ± 0.5) Kelvin. This value is in excellent agreement with the one obtained from magnetisation measurements namely $T_N = (17.3 \pm 0.1)$ Kelvin

From the data of the magnetic specific heat the magnetic entropy has been obtained using equation [4.71]. The entropy, as a function of T, is shown in figure 4.3.12.
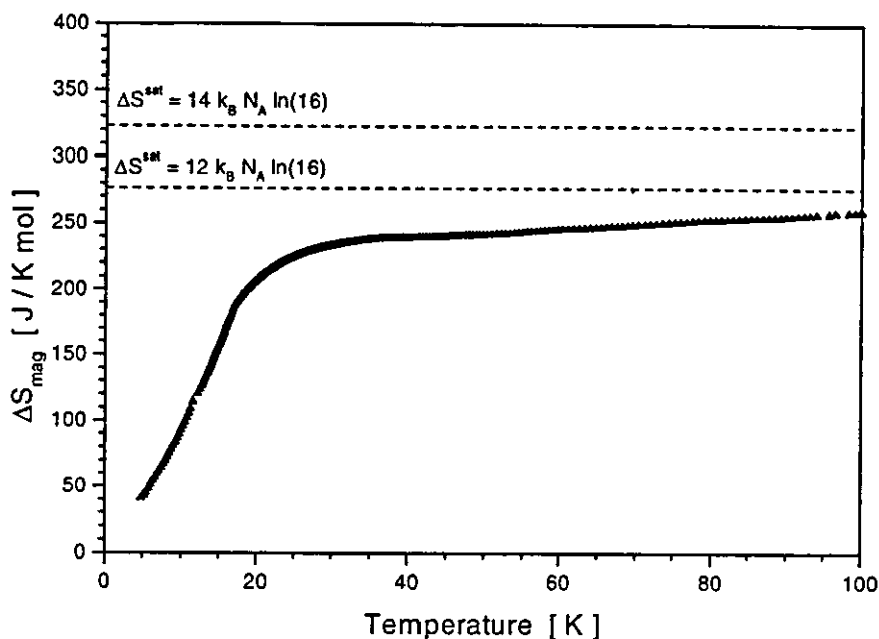
Figure 4 3 12. Magnetic entropy of $Dy_{14}Ag_{51}$ as a function of temperature

Similar to the results of the $Gd_{14}Ag_{51}$ and $Tb_{14}Ag_{51}$ samples the magnetic entropy is smaller than the theoretical entropy of $\Delta S^{sat} = 14 \cdot k_B N_A \cdot \ln(16)$ for 14 and $\Delta S^{sat} = 12\ k_B N_A \cdot \ln(16)$ for 12 Dysprosium atoms per unit cell.

The alloys $Ho_{14}Ag_{51}$ and $Er_{14}Ag_{51}$

Specific heat measurements have been carried out also for $Ho_{14}Ag_{51}$ and $Er_{14}Ag_{51}$ The plots of the total specific heat C_p, the magnetic contribution C_{mag} and the phonon contribution ($La_{14}Ag_{51}$) C_{phonon} are plotted in figures 4 3 13 and 4.3.15 for $Ho_{14}Ag_{51}$ and $Er_{14}Ag_{51}$, respectively. More detailed plots of the magnetic contribution are given in figures 4.3.14 and 4.3.16.

Figure 4 3.13 Molar specific heat C_p of $Ho_{14}Ag_{51}$ as a function of temperature (solid dots). The solid line indicates the phonon contribution C_{phonon}. The magnetic specific heat C_{mag} is shown by open dots.
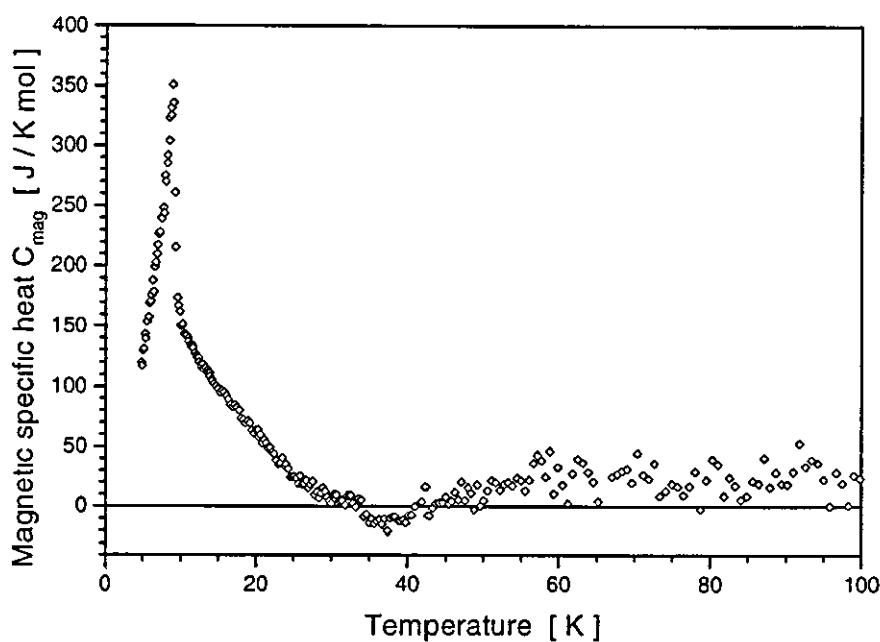
Figure 4 3.14· Magnetic specific heat of $Ho_{14}Ag_{51}$

The magnetic specific heat C_{mag} clearly reveals the phase transition at T_N of $(9\,0 \pm 0\,5)$ Kelvin by a sharp peak. The Néel temperature obtained by in magnetisation measurements is (9.1 ± 0.1) Kelvin. The first ordering point at T_1 of ~2.8 Kelvin, observed in the magnetisation measurements, could not be confirmed, because it was not possible to cool the system down to temperatures below 3.5 Kelvin.
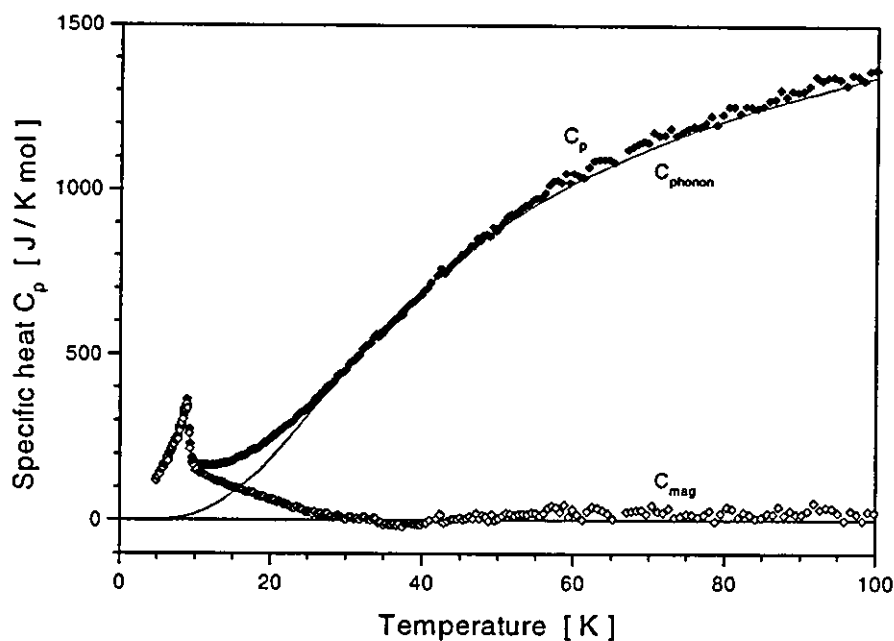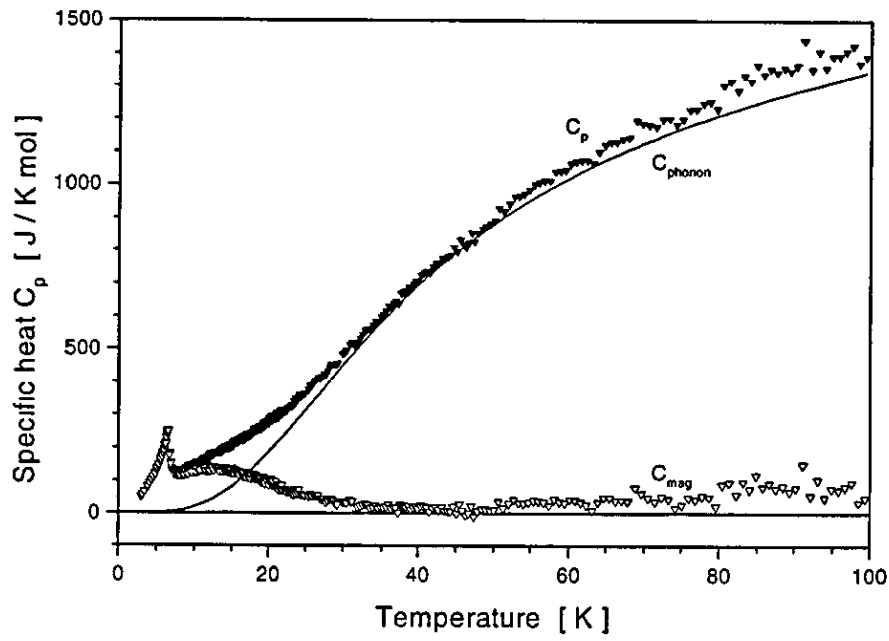

Figure 4 3 15· Molar specific heat C_p of $Er_{14}Ag_{51}$ as a function of temperature (solid dots) The solid line indicates the phonon contribution C_{phonon} The magnetic specific heat C_{mag} is shown by open dots

300

250

200

Magnetic specific heat C_{mag} [J / K mol]

150

100

50

0

0   20   40   60   80   100
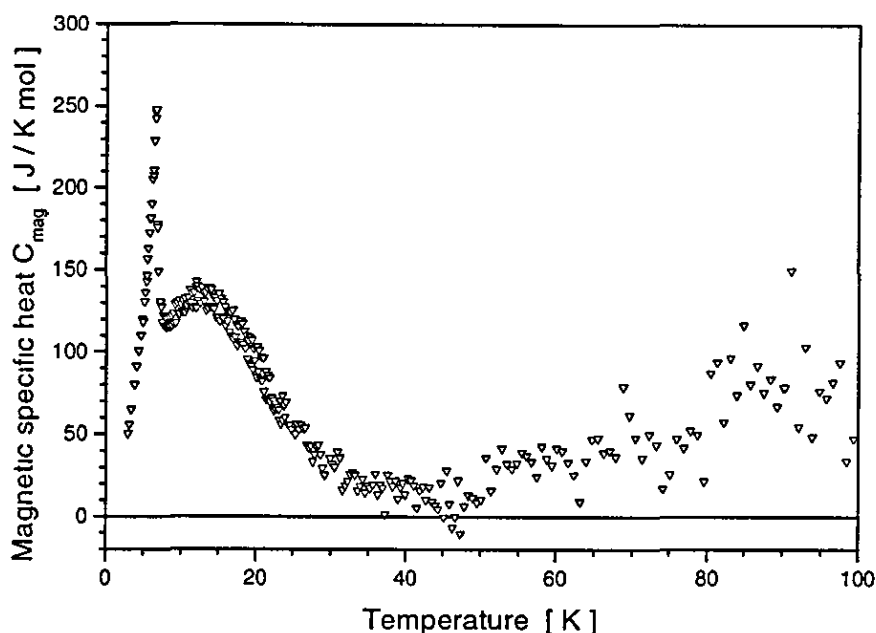
Temperature [K]

Figure 4 3 16   Magnetic specific heat of $Er_{14}Ag_{51}$

The magnetic specific heat of $Er_{14}Ag_{51}$ exhibits an unusual behaviour as a function of temperature. At $T_N = (6.5 \pm 0.3)$ Kelvin the phase transition can clearly be identified. The transition temperature T_N is in excellent agreement with the value of (6.7 ± 0.1) K obtained in magnetisation measurements However, a broad bump occurs at approximately 13 Kelvin. This bump can be attributed to CEF contributions. The first transition point obtained in the magnetisation measurements at T_1 of (4.2 ± 0.1) K has not been observed in the specific heat data.

The dependence of the magnetic entropy as a function of temperature for both alloys has been obtained from the magnetic specific heat and is shown in figure 4.3.17 for $Ho_{14}Ag_{51}$ and in figure 4.3.18 for $Er_{14}Ag_{51}$.

152

Figure 4 3.17: Magnetic entropy of $Ho_{14}Ag_{51}$. The dashed lines indicate the expected entropy values of $\Delta S^{sat} = 14\ k_B N_A\ ln(17)$ and $\Delta S^{sat} = 12\ k_B N_A\ ln(17)$

From figure 4.3.17 it can be seen that the experimental entropy ΔS exceeds the predicted value of $\Delta S^{sat} = 14 \cdot k_B N_A \cdot ln(17)$. This result is not physical. The theoretical value given by considering all rare earth atoms per unit cell is an upper bound to the magnetic entropy. Thus the experimentally obtained entropy should not exceed this value.

This "impossible" result for the magnetic specific heat indicates that the procedure to separating the lattice, electronic, and magnetic contributions is not valid. The above result indicates that interactions are important between these different contributions. Due to the magnitude of the entropy difference it is argued here that it must be an interaction between the magnetic and lattice subsystems which gives rise to the apparent "overshooting" of the total magnetic entropy. If such an interaction exists between these subsystems then the magnetic specific heat C_{mag} can not be obtained by subtracting the electronic and lattice contribution as observed for $La_{14}Ag_{51}$ from the total specific heat C_p.
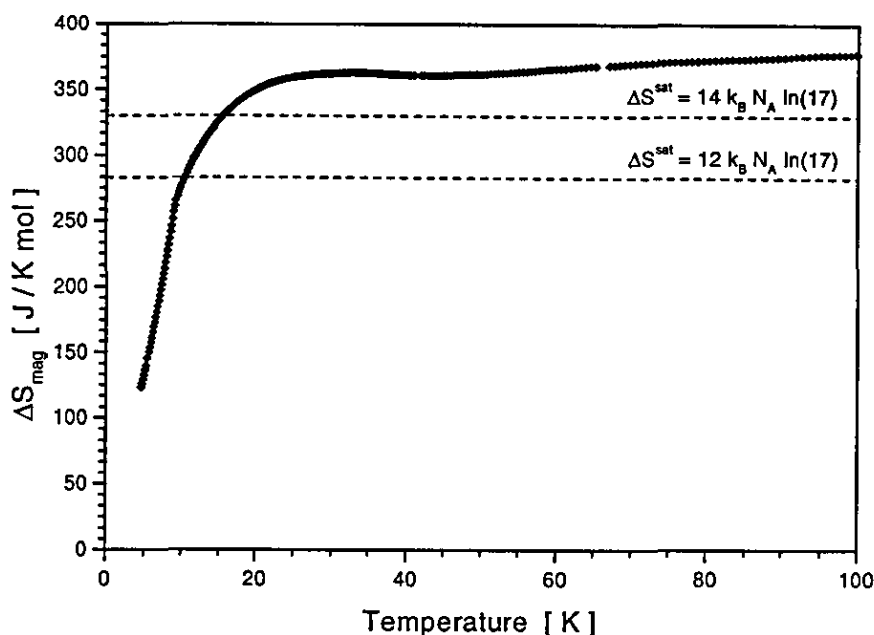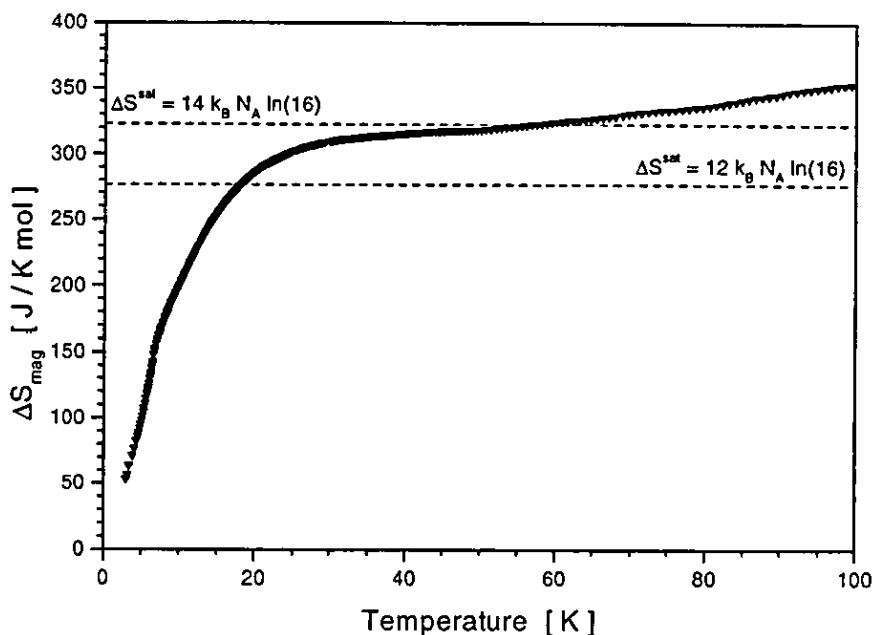
Figure 4.3 18· Magnetic entropy of $Er_{14}Ag_{51}$ The dashed lines indicate the expected entropy values of $\Delta S^{sat} = 14\,k_BN_A\cdot\ln(16)$ and $\Delta S^{sat} = 12\,k_BN_A\,\ln(16)$

The magnetic entropy of $Er_{14}Ag_{51}$ is shown in figure 4.3.18 as a function of temperature. From figure 4.3.16 it can be seen that the magnetic specific heat increases above ~40 K with increasing temperature. However the scatter in the data also increases. Thus it is not reasonable to take the data above 40 K into account. Considering only the data up to ~40 Kelvin the experimental value of the entropy of (330 ± 20) J/Kmol is equal to the expected value of 323 J/Kmol, which is equal to $\Delta S^{sat} = 14\cdot k_BN_A\ln(16)$ for 14 Erbium atoms. Therefore, with this restriction good agreement between experiment and theory is obtained for this compound.

Magnetic specific heat at low temperatures

The mean field theory of ferro- and antiferromagnetism fails at very low temperatures because it is unsuccessful in correctly representing the low lying excited states of a system, known as spin wave excitations. The difference at low

temperatures is that the energy of a spin should depend on the orientation of the spins in its neighbourhood, and not on the average magnetisation of the system. Thus the dependence of the magnetic specific heat on temperature (i.e. magnon contribution) can be derived by treating spin waves in a similar manner to the lattice vibrations considered in section 4.1.

Within the magnetically ordered ground state the low temperature properties are determined by low energy magnetic excitations. For different magnetic structures the magnon dispersion relation can take various forms which no turn determines the temperature dependence of the magnetic specific heat. For the characterisation of magnons with low energy a magnon dispersion as given by Dk^{α} is often sufficient. Here D the spin wave stiffness constant and α characterises the magnetic dispersion. The value of α depends of the type of magnetic ordering. Generally α takes a value of 2 for a ferromagnet and 1 for an antiferromagnet. Evaluating the integral of the magnetic energy at low temperature, it is sufficient to restricted the integration to the low energy part of the magnetic dispersion, namely

$$W_M = \int_{\omega} \hbar \omega D(\omega) f(\omega) d\omega,$$ [4.73]

or

$$W_M = \int_{BZ} E(\mathbf{k}) f(\mathbf{k}) d\mathbf{k},$$ [4.74]

where $f(\omega)$ is the Bose-Einstein distribution function (as magnons are bosons) and $D(\omega)$ the density of states given by the dispersion relation. A detailed calculation of this integral is given in the appendix.

The magnetic specific heat is then determined by the derivation of the energy W_M with respect to temperature. For a ferromagnet and an antiferromagnet it follows that the magnetic specific heat is proportional to

$$C_{mag} \propto T^{\frac{d}{\alpha}} = T^{\beta},$$ [4.75]

155

where d is the dimension of the magnetic system. Therefore, an exponent of $\beta = 3$ should occur for a 3-dimensional antiferromagnet and $\beta = 2$ for a 2-dimensional antiferromagnet. For a ferromagnet a β value of $\beta = 3/2$ (3-dim.) and $\beta = 1$ (2-dim.) is obtained.

Plotting the data of the magnetic specific heat C_{mag} in logarithmic form as $\ln(C_{mag})$ versus $\ln(T)$ should yield a linear dependence at low temperatures. In figures 4.3.18 - 4.3.22 the logarithmic plots are shown for the magnetic specific heat of $RE_{14}Ag_{51}$ compounds.

Figure 4.3 18   Logarithmic plot of the magnetic specific heat of $Gd_{14}Ag_{51}$

Figure 4 3 19. Logarithmic plot of the magnetic specific heat of Tb₁₄Ag₅₁

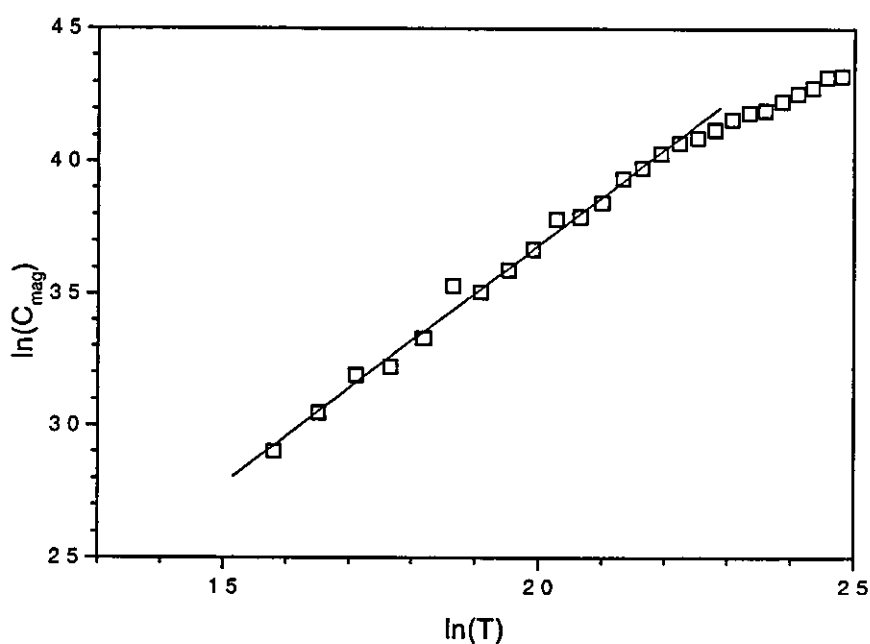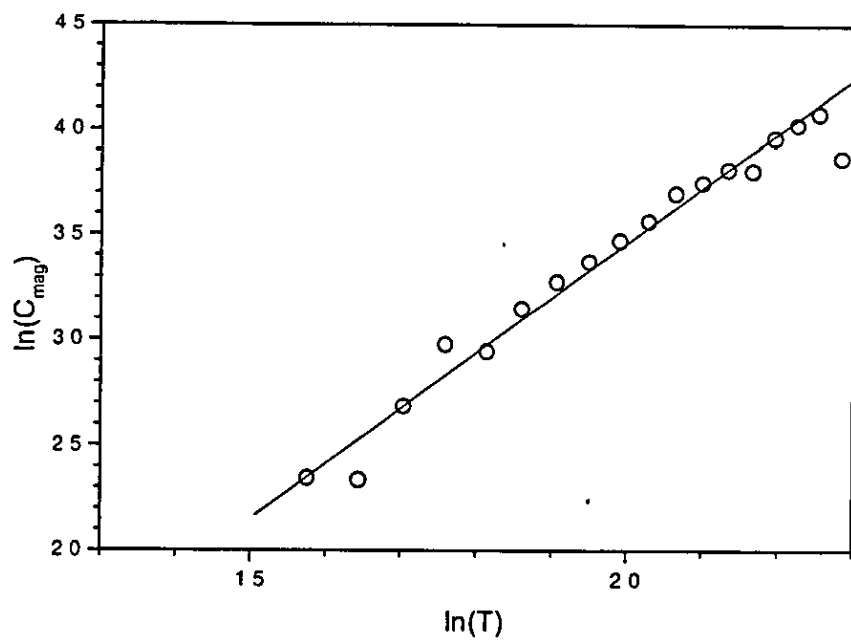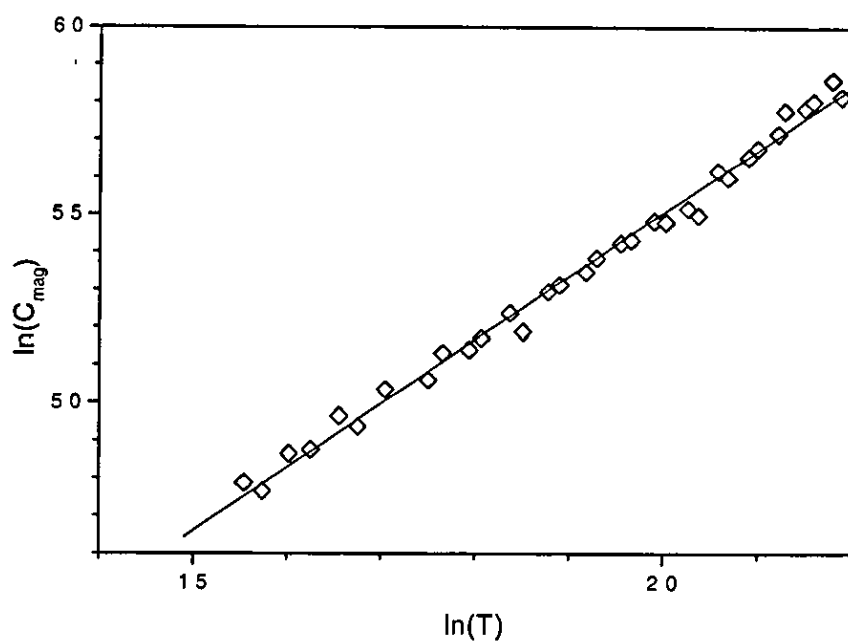*Figure 4 3 20 Logarithmic plot of the magnetic specific heat of Dy₁₄Ag₅₁*

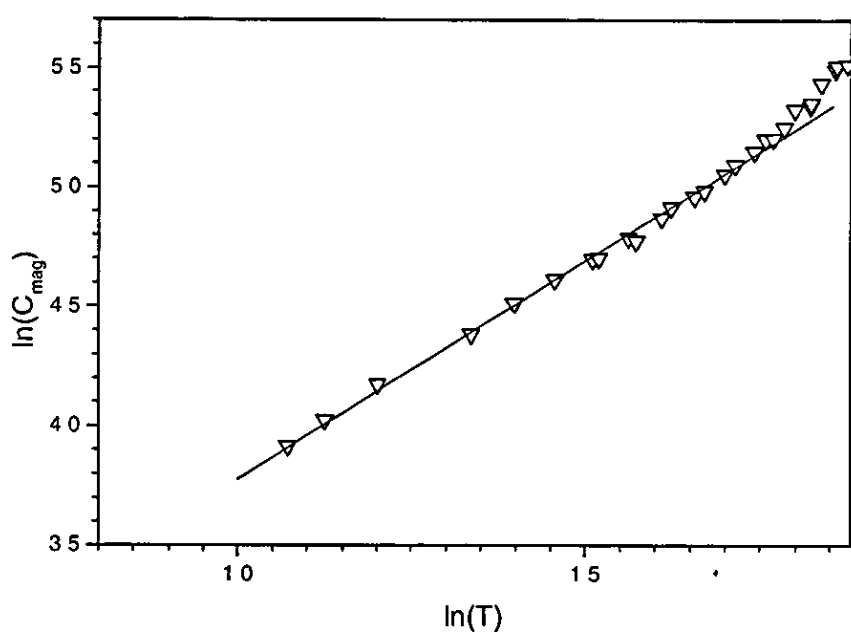*Figure 4 3.21. Logarithmic plot of the magnetic specific heat of $Ho_{14}Ag_{51}$*

Figure 4 3 22. Logarithmic plot of the magnetic specific heat of $Er_{14}Ag_{51}$

158

The plots exhibit linear behaviour at low temperatures. Thus the exponent β (see equation [4.75]) can be extracted using linear regression. The obtained values of β obtained by the fit are given in table 4.3.2 below.

Alloy	β
$Gd_{14}Ag_{51}$	1.9 ± 0.1
$Tb_{14}Ag_{51}$	2.5 ± 0.2
$Dy_{14}Ag_{51}$	1.8 ± 0.1
$Ho_{14}Ag_{51}$	1.7 ± 0.1
$Er_{14}Ag_{51}$	1.8 ± 0.1

Table 4 3 2: β values of the magnetic specific heat of $RE_{14}Ag_{51}$ (RE = Gd, Tb, Dy, Ho, Er)

From these results it can be seen that the β values are close to 2 and far from the value of 3 predicted for a 3-dimensional antiferromagnetic structure. Thus it may be argued that magnetic moments are confined to the hexagonal planes. Thus a 2-dimentional antiferromagnetic structure results.

Summary

The specific heat of the $RE_{14}Ag_{51}$ compounds (RE = La, Gd, Tb, Dy, Ho, and Er) has been measured using the method of adiabatic calorimetry over the temperature range ~4 K to 300 K. From the specific heat of $La_{14}Ag_{51}$, the non-magnetic reference compound, where only conduction electrons and lattice vibrations contribute to the total specific heat C_p (see equation [4.63]), a value for γ and the Debye temperature θ_D have been obtained of

$$\gamma = (20 \pm 80) \cdot 10^{-3} \text{ J/K}^2\text{mol}$$

$$\theta_D = (193 \pm 5) \text{ K.}$$

159

The γ value for Copper given in the literature [12] of 50·mJ/K²mol has within a factor of 2 the same magnitude as the one obtained for La₁₄Ag₅₁. The density of states $D(\varepsilon_F)$ at the Fermi surface of 8.5 states per formula unit and eV was calculated using the experimental γ value (see equation [4.61]).

$$D(\varepsilon_F) = \sim 8.5 \text{ states / f.u.. eV}$$

Considering the large error of γ (400%) the value of the density of states is of the same magnitude as the result of the magnetisation measurements namely $D(\varepsilon_F) = \sim 32$ states / f.u.. eV states per formula unit and eV.

The specific heat of La₁₄Ag₅₁ was used to subtract the electronic and lattice contribution from the total specific heat C_p of the magnetic RE₁₄Ag₅₁ compounds. The remaining specific heat was interpreted as the magnetic contribution C_{mag} of C_p and analysed. Further for all magnetic compounds a peak at the antiferromagnetic phase transition at T_N has been observed. Also the order-order transition at T_I has been identified for Gd₁₄Ag₅₁. For the compounds Ho₁₄Ag₅₁ and Er₁₄Ag₅₁ the order-order transition has not been seen in the measurements above ~4 Kelvin. Furthermore, the thermal dependence at low temperatures of the magnetic specific heat has been analysed using a logarithmic plot of ln(C_{mag}) as a function of ln(T). In these plots a linear behaviour at low temperatures was revealed for each alloy and a linear fit to the data has been carried out in order to obtain the temperature dependence given by the exponent β ($C_{mag} \propto T^\beta$). The experimentally obtained values for the transition temperatures T_N, T_I and the β values are shown in table 4.3.2 and compared to the results of the magnetisation measurements ($T_N^{(Mag)}$, $T_I^{(Mag)}$) extrapolated to zero applied magnetic field.

160

Alloy	T_N [K]	$T_N^{(Mag)}$ [K]	T_1 [K]	$T_1^{(Mag)}$ [K]	β
$Gd_{14}Ag_{51}$	36 ± 1	36 7 ± 0.1	14 ± 1	13 6 ± 0 1	1 9 ± 0 1
$Tb_{14}Ag_{51}$	27 3 ± 0 5	27.8 ± 0.1	-	-	2 5 ± 0.2
$Dy_{14}Ag_{51}$	17 0 ± 0 5	17.3 ± 0 1	-	-	1.8 ± 0 1
$Ho_{14}Ag_{51}$	9.0 ± 0 5	9 1 ± 0.1	-	2 8 ± 0 1	1.7 ± 0.1
$Er_{14}Ag_{51}$	6.5 ± 0 5	6 7 ± 0 1	-	4 2 ± 0 1	1 8 ± 0 1

Table 4 3 2· Characteristics of the magnetic specific heat of $RE_{14}Ag_{51}$ (RE = Gd, Tb, Dy, Ho, and Er)

From this table it can be seen that consistent phase transition temperatures have been obtained for both methods of measurement, magnetisation and specific heat. The absence of the order-order phase transitions at T_1 of $Ho_{14}Ag_{51}$ and $Er_{14}Ag_{51}$ in the specific heat measurement is attributed to the calorimeter system which could not be cooled down to sufficiently low temperatures. Furthermore, from this table it can be seen that the values of β are close to a value of 2.

In order to obtain the magnetic entropy as a function of temperature for each rare-earth silver compound the integral given by equation [4.65] has been calculated using the experimentally obtained magnetic specific heat C_{mag} as a function of temperature. The magnetic entropy is related to the spin degrees of freedom of each of the rare earth atoms Thus a theoretical value for the magnetic entropy assuming an ideal antiferromagnet can be calculate using $\Delta S^{sat} = c k_B N_A \ln[2J+1]$, where c is the number of magnetic rare earth atoms per unit cell carrying a magnetic moment.

The graphs of the magnetic entropy obtained for $Gd_{14}Ag_{51}$, $Tb_{14}Ag_{51}$, and $Ho_{14}Ag_{51}$ show that the theoretical value is not reached experimentally. The difference amounts to approximately 20%. There are different reasons for obtaining lower values of the magnetic entropy, e g. due to CEF splitting. However, for $Gd_{14}Ag_{51}$, where no crystal field effects are involved, this result is unusual. In comparison to $Gd_{14}Ag_{51}$ the magnetic entropy of $Ho_{14}Ag_{51}$ exceeds the theoretical value. This is in principle impossible. Only for the compound

$Er_{14}Ag_{51}$ are the experimental and theoretical value in agreement. These results justify to argue that the magnetic specific heat C_{mag}, obtained by subtract the phonon blank C_{phonon} from the total specific heat C_p of the magnetic compound, does not properly represent the magnetic contribution to the total specific heat C_p.

If the lattice and magnetic degrees of freedom are coupled then it is not possible to subtract the lattice contribution by using the specific heat of $La_{14}Ag_{51}$ from the total specific heat C_p of the magnetic compound. The interaction between lattice and magnetic degrees of freedom results in a renormalisation of both subsystems, the magnetic and the lattice one. As a consequence of this interaction the physics becomes more complicated and the different contributions are not any more separable. As a possible source of such a coupling magnetostriction is mentioned here. Therefore, the attempt to simply subtract the specific heat of $La_{14}Ag_{51}$ from the total specific heat C_p in order to obtain the magnetic specific heat C_{mag} contributions will result in part of the lattice specific heat being attributed to the magnetic subsystem. If the entropy ΔS is calculated using the magnetic specific heat C_{mag} then erroneous results are obtained

If magnetostriction mechanism is responsible then magnetostriction and thermal expansion measurements will be able to identify details of this interaction. At present it can only be argued on the basis of the specific heat measurements, that the lattice contribution as obtained experimentally by the $La_{14}Ag_{51}$ measurements, is not a truthful reference for the lattice contribution of the magnetic compounds.

Chapter 5 Discussion

The characterisation of the magnetisation measurements is summarised in section 3 3 of chapter 3. In table 4.3.2 (chapter 4) the phase transition temperatures of the specific heat measurement are shown and compared to the T_N values as extracted from magnetisation measurements. Excellent agreement is obtained been both sets of measurements. The values obtained here have to be compared to the results of Ikonomou et al. [13] carried out on the isostructural rare earth gold series. Ikonomou et al. determined the magnetic ordering temperatures and effective magnetic moments of $REAu_{36}$ compounds, which correspond to $RE_{14}Au_{51}$. In table 5.1.1 their and our results are shown and compared.

RE	T_N^* [K] $RE_{14}Ag_{51}$	T_N^* [K] $REAu_{16}$	T_1^* [K] $RE_{14}Ag_{51}$	T_1^* [K] $REAu_{16}$	θ_N^* [K] $RE_{14}Ag_{51}$	θ_N^* [K] $REAu_{16}$
Gd	36 7	22 5	13 6	13	-6 9	-10
Tb	27.8	22 5	~15	-	1 2	-12.5
Dy	17.3	13 0	~4	-	-0 4	-7 0
Ho	9 1	7 5	2 8	-	-0 4	-5 5
Er	6 7	-	4 2	-	1.7	-

*Table 5 1.1   Magnetic characteristics of $RE_{14}Ag_{51}$ and $REAu_{36} = RE_{14}Au_{51}$ [13] (RE = Gd, Tb, Dy, Ho, Er) The table shows our experimental obtained by transition and paramagnetic Curie temperatures and the results by Ikonomou et al. * this work, * Ikonomou et al*

The values of the transition temperatures for the Au-series obtained by Ikonomou et al. are smaller than those of the Ag-series. As Au and Ag are in the same column of the periodic table their electronic configuration and consequently the electronic band structure is expected to be similar for both compounds

However, the atomic radii are different, affecting the lattice constants and also the electronic band width. With the Au-atom being larger than the Ag-atom the

distance between RE-atoms is increased This may be taken as the reason for the reduction in the characteristic magnetic interaction strength for Au-alloys compared to the Ag-ones This is evidenced in the phase transition temperatures For θ_N Ikonomou et al. obtained negative values for all compounds. The values obtained for the effective paramagnetic Bohr magneton number p_{eff} are also shown in table 5.1.2. For a comparison with other RE-Ag-compounds see Kissell et al [14] for REAu compounds (CsCl structure type) and Sill et al. [15] for REAu$_2$ alloys (MoSi$_2$-type structure). For comparison the values are indicated in table 5.1.2.

RE	p_{eff} * RE$_{14}$Ag$_{51}$	p_{eff} * REAg$_{3.6}$	p_{eff} + REAu	p_{eff} ‡ REAu$_2$	p_{eff} cal
Gd	8 1	8 2	7 92	8 38	7 94
Tb	9 9	9 8	9 54	9 83	9.72
Dy	10 9	11 1	10 22	10 52	10 65
Ho	10 54	10 9	10 5	10 97	10 61
Er	9 65	-	9 42	9.45	9 58

Table 5 1.2: Results of the effective paramagnetic Bohr magneton number p_{eff} of RE$_{14}$Ag$_{51}$ and REAg$_{3.6}$ [13], REAu [14], and REAu$_2$ [15] (RE = Gd, Tb, Dy, Ho, Er) * this work, * Ikonomou et al., + Kissel et al, ‡ Sill et al.

From table 5.1.2 it can be seen that the experimental results of the effective paramagnetic Bohr magneton number p_{eff} agree with the theoretical value.

In contrast to our results on the Ag-series of alloys Ikonomou et al. only observed a second phase transition for GdAu$_{3.6}$ For all other REAu$_{3.6}$ compounds only one transition has been reported. However, additional phase transitions have been found for other antiferromagnetically ordered rare earth silver/gold compounds. Sill et al. [15] observed a second magnetic transition for TbAu$_2$ and DyAu$_2$ below the Néel temperature. In the paper by Miura et al. [16] magnetic transitions for DyAg$_2$ and HoAg$_2$ are reported in addition to the antiferromagnetic phase transition at T$_N$. A more detailed comparison and

discussion of the observed transitions is not meaningful, because the results are obtained on compounds with different crystallographic and magnetic structures.

In table 3.3.3 in section 3.3 the values are shown of the critical fields at the field induced magnetic transitions. Magnetic field induced transitions have been observed for all $RE_{14}Ag_{51}$ except $Gd_{14}Ag_{51}$ at low temperatures. The phases between these transitions are characterised by a positive magnetisation with a linear field dependence. These magnetisation values are of comparable magnitude for all compounds. Thus it may be argued that the field induced magnetic phases are due to a partial alignment of magnetic moments along the field direction In the literature field induced magnetic phase transitions are reported for some different rare-earth compounds (REAg, REAu, $REAg_2$, $REAu_2$) by Kaneko et al. [17] [18] and by S. Miura et al. [19].

In order to obtain a better explanation an investigation of the magnetic structure of the $RE_{14}Ag_{51}$ compounds is required. Neutron diffraction experiments provide a suitable method for the investigation of the atomic and magnetic structure. As long the magnetic structure is unknown, no detailed explanation can be put forward with respect to the magnetic properties.

In the previously discussion a detailed and separate analysis has been given of each compound. Therefore an attempt is made to put the results into a larger framework. A good pictured overview of the transition temperatures is given by plotting the specific heat as shown in figure 5.1.1
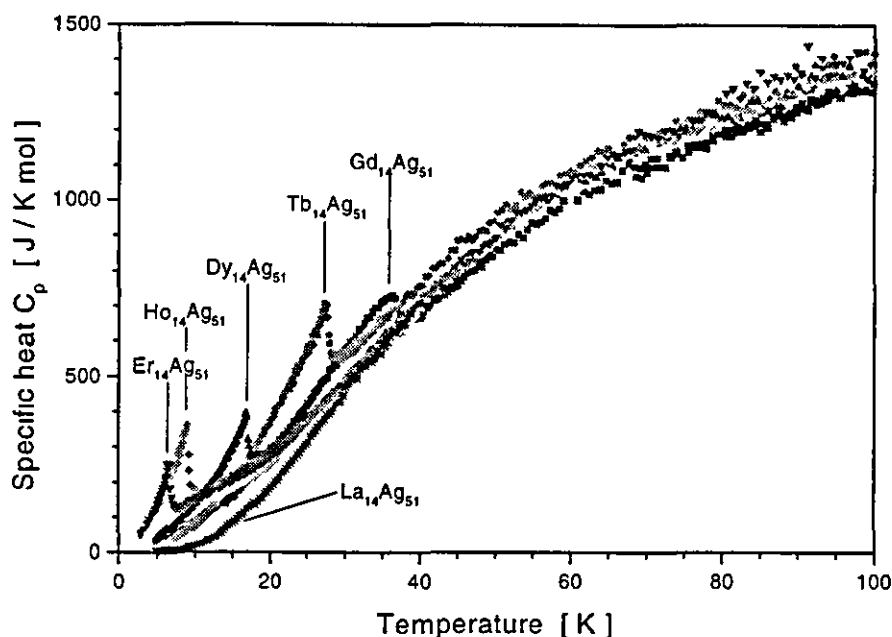
Figure 5.1.1 Specific heat as a function of temperature for $RE_{14}Ag_{51}$ (RE = Gd, Tb, Dy, Ho, ER, and La)

Figure 5 1.1 shows that each rare-earth compound has its unique phase transition (T_N) indicated by an anomaly in the specific heat. The value of the transition temperature decreases with increasing number of f-electrons for the rare-earth alloys. An analysis of the systematic of the transition temperatures is given next.

The interaction of localised magnetic moments of rare earth atoms with conduction electrons is frequently modelled using a point contact interaction, the magnitude of which depends on the details of the conduction electron density at the lattice site of the rare earth atom. In the simple model of an election band structure, which does not vary significantly across an isostructural series, the magnetic interaction strength scales with the quantum numbers of the $4f$ electrons. The type of magnetic order which minimises the magnetic energy is independent of the rare earth atoms. Only the magnetic energy scale in modified by replacing one rare earth atom by another one. Such a simple model gives rise to a scaling of the transition temperatures for the various members of the $RE_{14}Ag_{51}$ alloy series. In the presence of strong spin-orbit coupling on the rare earth ion and an interionic exchange interaction between spins, the constant of

166

the proportionality is given as $(g-1)^2 J(J+1)$. This scaling is known as de Gennes scaling and the constant of the proportionality is called the de Gennes factor Γ.

$$\Gamma = (g-1)^2 J(J+1) \tag{5.1}$$

On a molecular field model the Néel $\tilde{T}_N(RE)$ temperature is proportional to Γ

$$\tilde{T}_N(RE) \propto (g-1)^2 J(J+1) \tag{5.2}$$

For this argument the nature of the magnetic ordering is immaterial. It is only assumed that the type of magnetic order does not vary across the rare earth series.

A plot of the transition temperatures T_N of $RE_{14}Ag_{51}$ has been constructed as a function of the de Gennes factor and is shown in figure 5 3 2. The values for T_N are obtained by magnetisation measurements. The value of the transition temperature of the compound $Ce_{14}Ag_{51}$ of $T_N = 1.1$ K as reported by Trovarelli et al. [20] is also included.
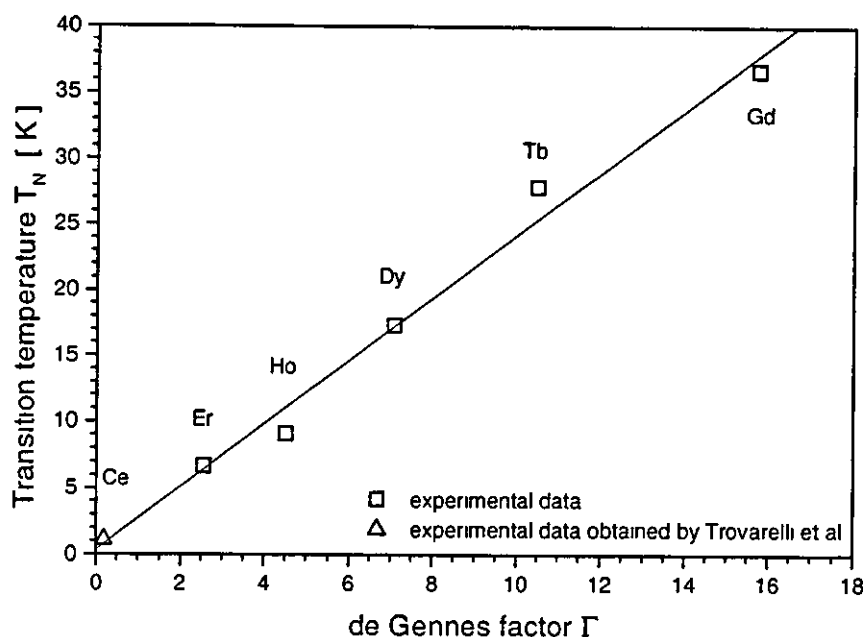
Figure 5 3 2 *Transition temperatures T_N of $RE_{14}Ag_{51}$ (RE = Ce [20], Gd, Tb, Dy, Ho, Er) versus de Gennes factor Γ*

The dependence of the experimentally obtained antiferromagnetic phase transition temperatures on the de Gennes factor are represented well by a straight line as shown in figure 5.3.2. This also includes the value of the phase transition of $Ce_{14}Ag_{51}$ as given by Trovarelli et al., which is in excellent agreement with the linear model. Thus a scaling dependence of T_N has been identified for the $RE_{14}Ag_{51}$ series. This result is in contrast to the results of Ikonomou et al. The transition temperatures of the Au-series do not obey the de Gennes law.

The experimentally obtained transition temperatures together with their "theoretical" value obtained by using the fit to the data points in of figure 5.3.2 are given in table 5.1.3.

Alloy	S	L	J	g	Γ	$T_N^{(cal)}$ [K]	$T_N^{(obs)}$ [K]
La$_{14}$Ag$_{51}$	0	0	0	-	-	-	-
Ce$_{14}$Ag$_{51}$	1/2	3	5/2	6/7	5/28	0 78	1 1[*]
Pr$_{14}$Ag$_{51}$	1	5	4	4/5	4/5	2.26	
Nd$_{14}$Ag$_{51}$	3/2	6	9/2	8/11	81/44	6 90	
Pm$_{14}$Ag$_{51}$	2	6	4	3/5	16/5	7 97	
Sm$_{14}$Ag$_{51}$	5/2	5	5/2	2/7	125/28	10 98	
Eu$_{14}$Ag$_{51}$	3	3	0	-	-	-	
Gd$_{14}$Ag$_{51}$	7/2	0	7/2	2	63/4	37 85	36 7
Tb$_{14}$Ag$_{51}$	3	3	6	3/2	21/2	25 35	27 8
Dy$_{14}$Ag$_{51}$	5/2	5	15/2	4/3	85/12	17 22	17 3
Ho$_{14}$Ag$_{51}$	2	6	8	5/4	9/2	11 07	9 1
Er$_{14}$Ag$_{51}$	3/2	6	15/2	6/5	51/20	6 43	6 7
Tm$_{14}$Ag$_{51}$	1	5	6	7/6	7/6	3 13	
Yb$_{14}$Ag$_{51}$	1/2	3	7/2	8/7	9/28	1 12	
Lu$_{14}$Ag$_{51}$	0	0	0	-	-	-	-

Table 5 1.3   Characteristic values and de Gennes scaling of the transition temperatures of RE$_{14}$Ag$_{51}$ [*] Value of the transition temperature of Ce$_{14}$Ag$_{51}$ reported by Trovarelli et al [20]

For the second magnetic transition temperatures T_1 for Gd$_{14}$Ag$_{51}$, Ho$_{14}$Ag$_{51}$ and Er$_{14}$Ag$_{51}$ an attempt to observe de Gennes scaling was not successful. For these transitions a simple de Gennes scaling is not appropriate.

Appendix

Spin wave dependence to low temperature magnetic specific heat

The total magnetic energy of a system of magnons is obtained by integration over the Brillouin zone in k space

$$W_M = \int_{BZ} E(\mathbf{k}) f(\mathbf{k}) \, d\mathbf{k},$$ [A.1]

where $E(\mathbf{k})$ is the energy of one magnon and $f(\mathbf{k})$ the distribution function. For magnons, which are bosons, the Bose -Einstein distribution function is valid

$$f(\mathbf{k}) = \frac{1}{\exp[\beta E(\mathbf{k})] - 1},$$ [A.2]

where $\beta = (k_B T)^{-1}$.

For the following the interest will be focussed on the low temperature properties. This allows to restrict the magnetic dispersion $E(\mathbf{k})$ to the low temperature part only. In the low temperature range and the dispersion can be described by a power law of the form

$$E(\mathbf{k}) = D k^\alpha,$$ [A.3]

where D the spin wave stiffness constant and α the characteristic parameter which defines the magnetic order. For a simple antiferromagnet $\alpha = 1$ and $\alpha = 2$ for a ferromagnet.

For low temperatures only those k-values are thermally populated which are close to the k-value for which magnetic Bragg reflections occur. Around the Bragg reflections the magnetic dispersions rises to higher energies with a k-dependence as given in [A.3]. Only a small region in reciprocal space centred at

170

the Bragg reflections is relevant for determining the low temperature properties. In this limit it is permissible to extend the Brillouin zone boundary to infinity and to approximate [A.1] by

$$W_M = D \int_0^\infty k^\alpha \frac{1}{\exp[\beta D k^\alpha] - 1} \, dk \qquad\qquad [A 4]$$

Changing to spherical co-ordinates in d dimensions results in

$$\int_0^\infty d\mathbf{k} = \int_0^\infty k^{d-1} dk \int_0^{2\pi} \int_0^\pi \sin \vartheta \, d\varphi \, d\vartheta \qquad\qquad [A.5]$$

which yields the above integral in the form

$$W_M = 4\pi D \int_0^\infty k^\alpha \, k^{d-1} \frac{1}{\exp[\beta D k^\alpha] - 1} \, dk \qquad\qquad [A.6]$$

With the variable substitution

$$x = \beta D k^\alpha \qquad\qquad [A.7]$$

and thus

$$k^\alpha = \frac{x}{\beta D} \qquad\qquad [A.8]$$

$$k^{d-1} = \left(\frac{x}{\beta D} \right)^{\frac{d-1}{\alpha}} \qquad\qquad [A.9]$$

$$dk = \frac{1}{\alpha \beta D k^{\alpha-1}} \, dx = \frac{1}{\alpha \beta D} \left(\frac{x}{\beta D} \right)^{-\frac{\alpha-1}{\alpha}} dx \qquad\qquad [A.10]$$

the integral is changed to

$$W_M = 4\pi D \int_0^\infty \left(\frac{x}{\beta D} \right) \left(\frac{x}{\beta D} \right)^{\frac{d-1}{\alpha}} \frac{1}{\alpha \beta D} \left(\frac{x}{\beta D} \right)^{-\frac{\alpha-1}{\alpha}} \frac{1}{\exp[x] - 1} \, dx \quad [A.11]$$

171

$$W_M = \frac{4\pi}{\alpha\beta}\left(\frac{1}{\beta D}\right)^{\frac{d}{\alpha}} \int_0^{\infty} (x)^{\frac{d}{\alpha}} \frac{1}{\exp[x]-1} \, dx \qquad \text{[A.12]}$$

For the determination of the low temperature properties it is sufficient to discuss the temperature dependence of the internal magnetic energy W_M. The integral and the other constants will determine the scale which, however, is not relevant for our discussion. The temperature dependence of the internal magnetic energy is given as a power law of the form

$$W_M \propto T^{1+\frac{d}{\alpha}} \qquad \text{[A.13]}$$

The magnetic specific heat C_{mag} is obtained by taking the derivative of [A.13] with respect to T resulting in

$$C_{mag} = \frac{dW_M}{dT} \propto T^{\frac{d}{\alpha}} = T^{\beta} \qquad \text{[A.14]}$$

This result is used for the discussion of the low temperature magnetic specific heat result in section 4.3 on page
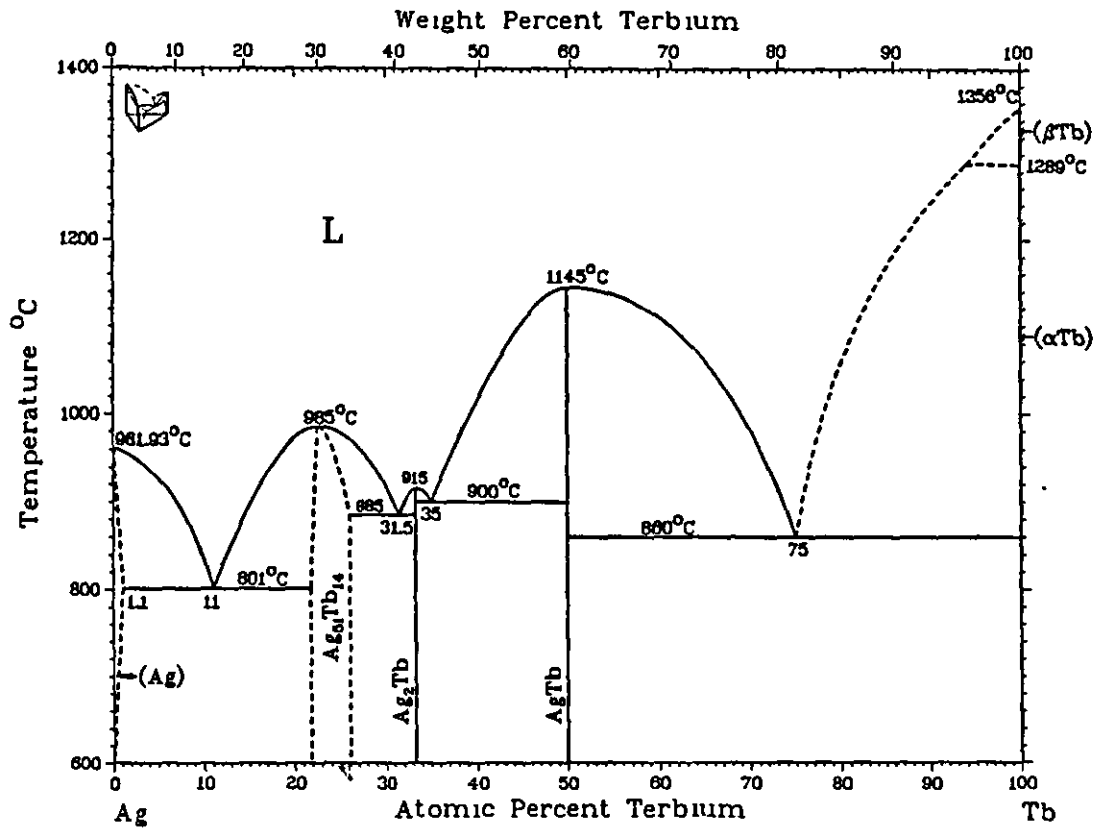
List of constants

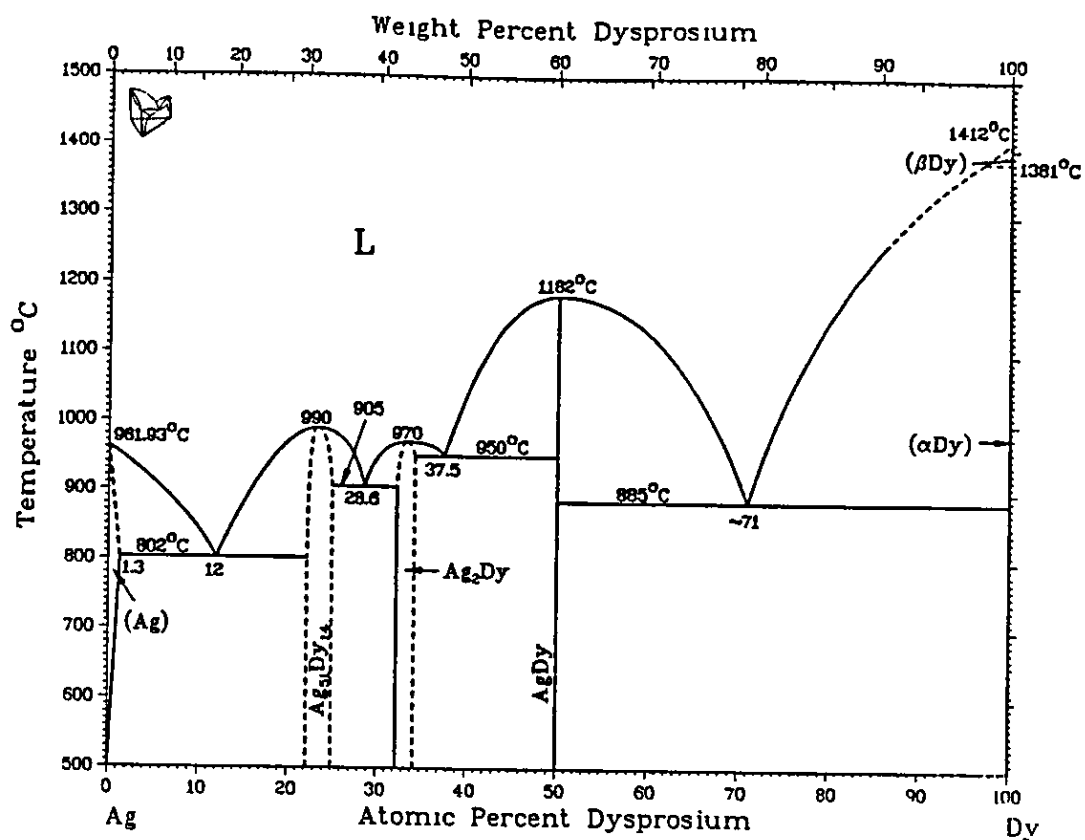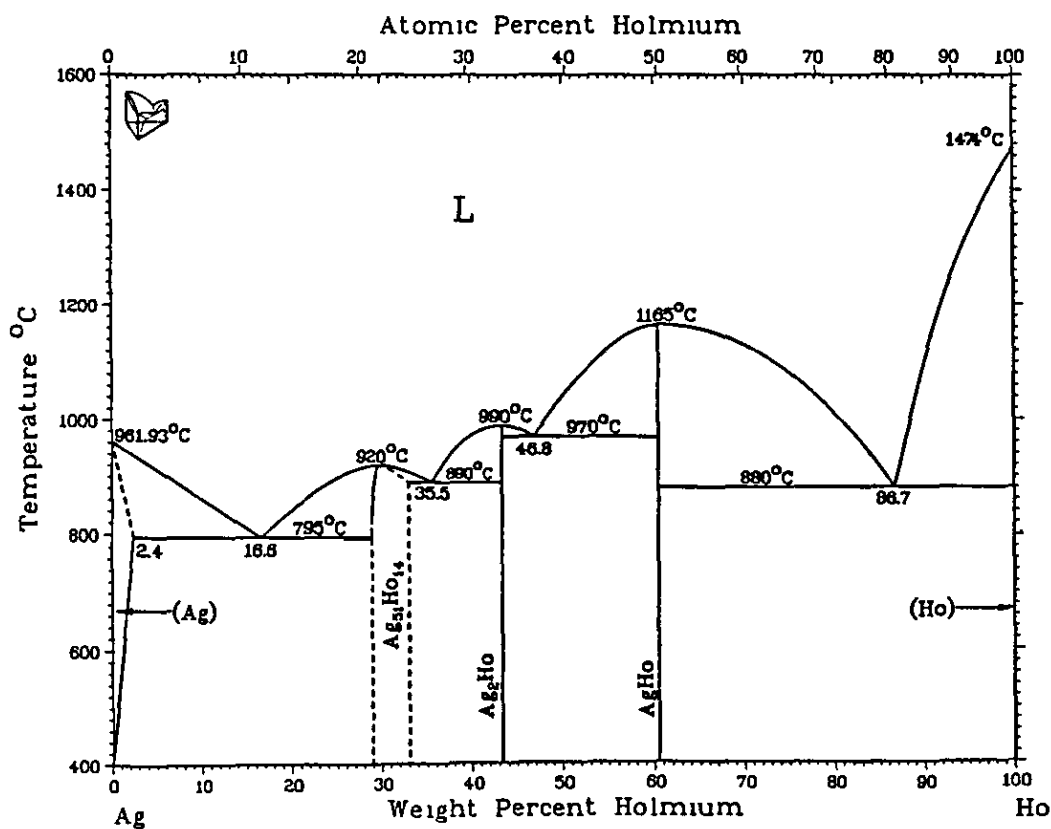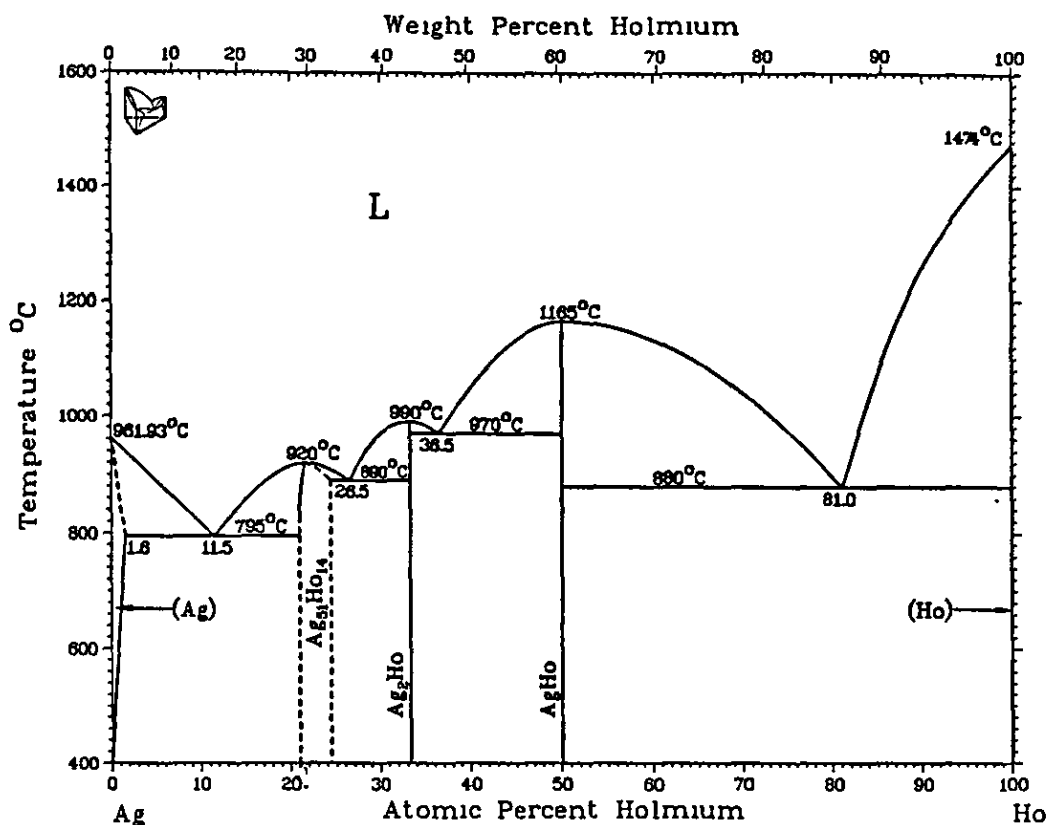|		
Velocity of light	c	$2.998 \cdot 10^8$ m/s
Elementary charge	e	$1.602 \cdot 10^{-19}$ C
Electron mass	m_e	$9.110 \cdot 10^{-31}$ kg
Proton mass	m_p	$1.673 \cdot 10^{-27}$ kg
The ratio m_p/m_e	m_p/m_e	1836.15
Plank's constant	h	$6.626 \cdot 10^{-34}$ Js
	$\hbar = h/2\pi$	$1.055 \cdot 10^{-34}$ Js
Bohr magneton	$\mu_B = e\hbar/2m_e$	$9.273 \cdot 10^{-24}$ J/T
Nuclear magneton	$\mu_n = e\hbar/2m_p$	$5\,051 \cdot 10^{-27}$ J/T
Bolzmann constant	k_B	$1.381 \cdot 10^{-23}$ J/K
Avogadro constant	N_A	$6.022\ 10^{23}$ 1/mol (molecules per mole)
Molar gas constant	$R = k_B N_A$	8.314 J/mol K

Assessed Ag-Gd Phase Diagram

Weight Percent Gadolinium

961.93°C
975°C
1100°C
1313°C
(βGd)
1235°C
L
830°C   35
825°C
805°C
~0.95   11
37
790°C
77.5
(αGd)
(Ag)
Ag₅₁Gd₁₄
Ag₂Gd
AgGd
Ag   24.5%   25%   Atomic Percent Gadolinium   Gd

Atomic Percent Gadolinium

961.93°C
975°C
1100°C
1313°C
(βGd)
1235°C
L
830°C   44
825°C
805°C
~1.4   15.3
46.1
790°C
83 4
(αGd)
(Ag)
Ag₅₁Gd₁₄
Ag₂Gd
AgGd
Ag   Weight Percent Gadolinium   Gd

K.A Gschneidner, Jr and F W. Calderwood, 1985
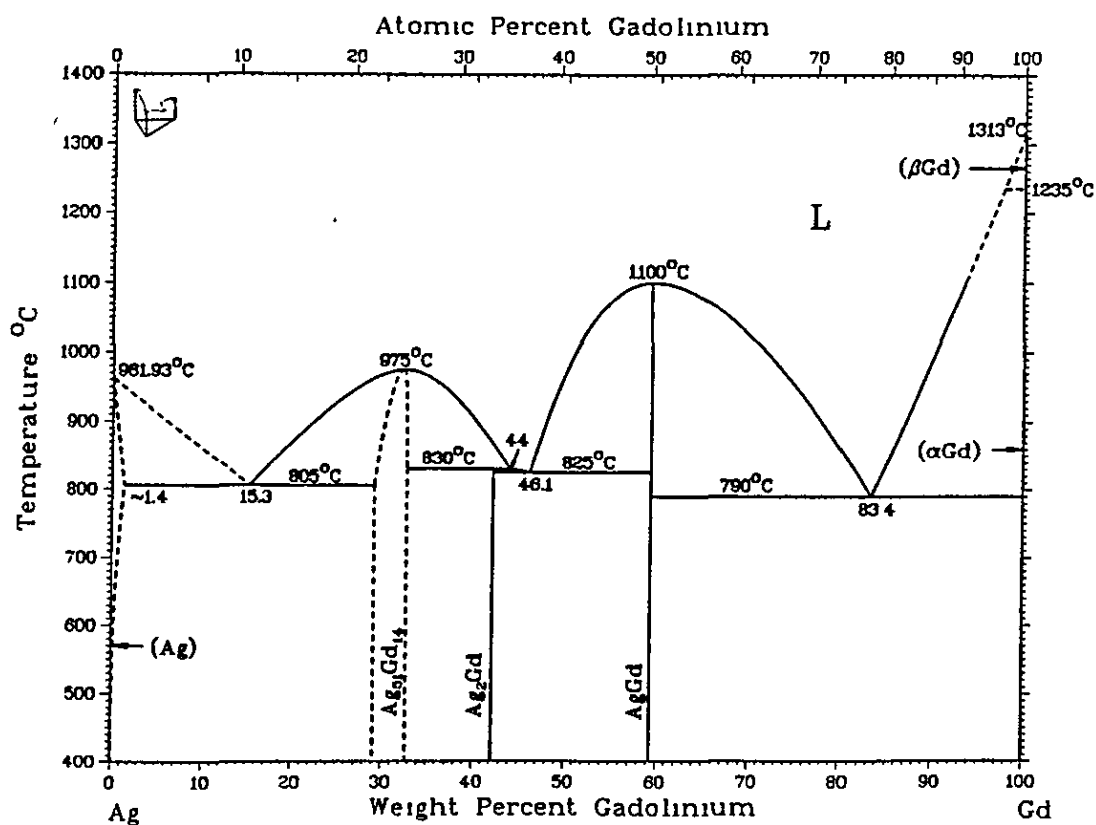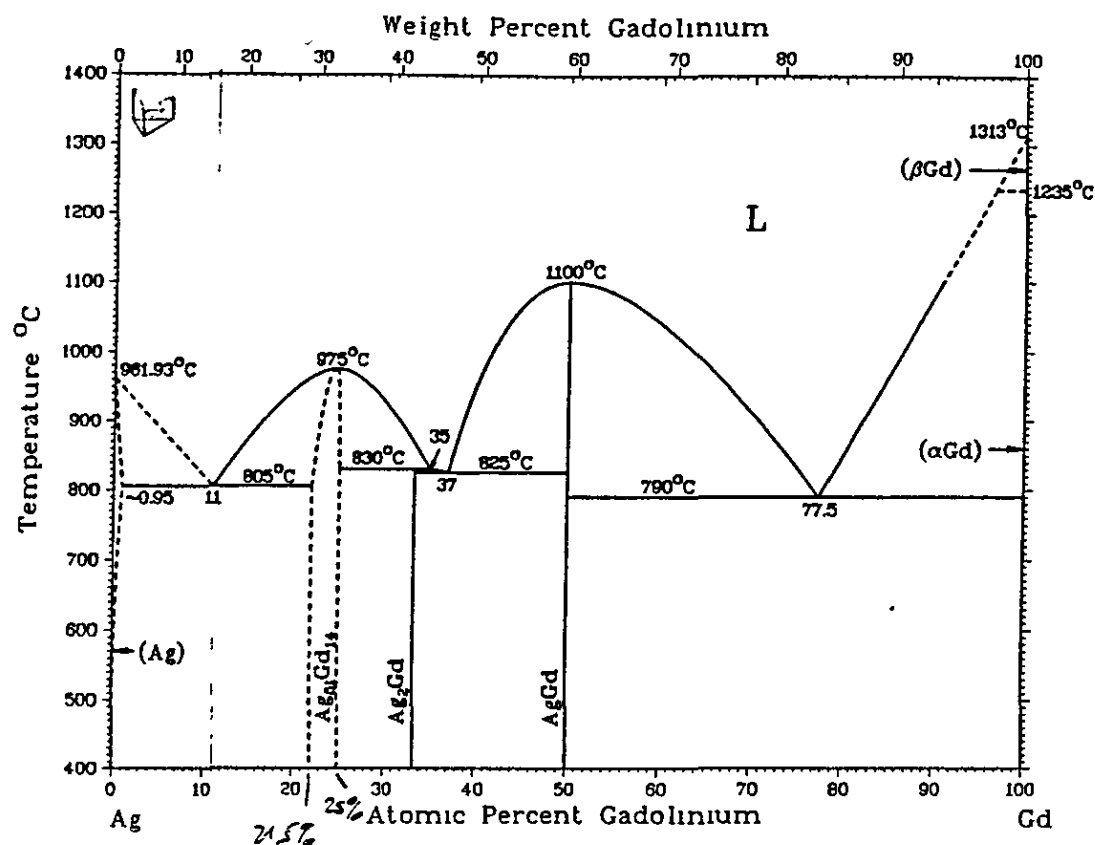
Assessed Ag-Tb Phase Diagram

Weight Percent Terbium

L

961.93°C
965°C
1145°C
915
900°C
885
31.5   35
801°C
L1   11
Ag₅₁Tb₁₄
Ag₂Tb
AgTb
(Ag)
860°C
75
1356°C
(βTb)
1289°C
(αTb)

Temperature °C

Atomic Percent Terbium

Ag   Tb

Atomic Percent Terbium

L

961.93°C
965°C
1145°C
915
900°C
885
40.4 44.2
801°C
1.6   15.4
Ag₅₁Tb₁₄
Ag₂Tb
AgTb
(Ag)
860°C
81.5
1356°C
(βTb)
1289°C
(αTb)

Temperature °C

Weight Percent Terbium

Ag   Tb

K A. Gschneidner, Jr and F.W. Calderwood, 198

Assessed Ag-Dy Phase Diagram
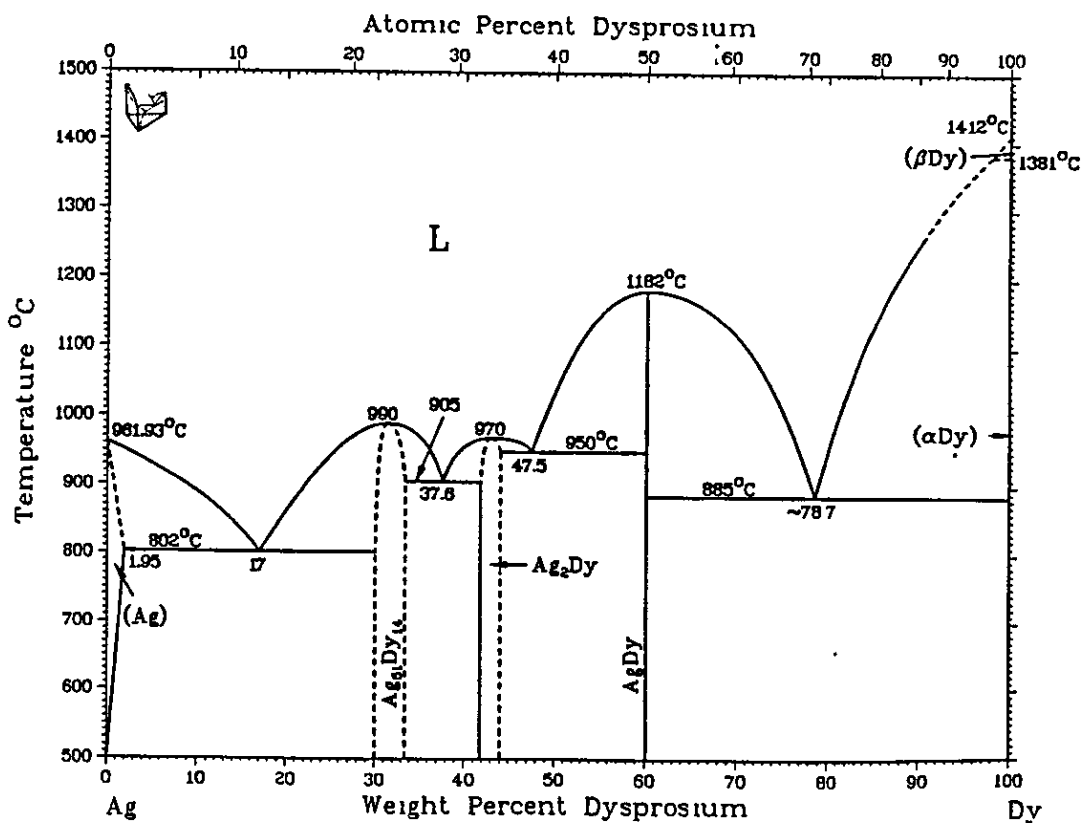
Assessed Ag-Ho Phase Diagram

K.A. Gschneidner, Jr. and F.W. Calderwood, 1985

Assessed Ag-Er Phase Diagram

K.A. Gschneidner, Jr. and F.W. Calderwood, 19
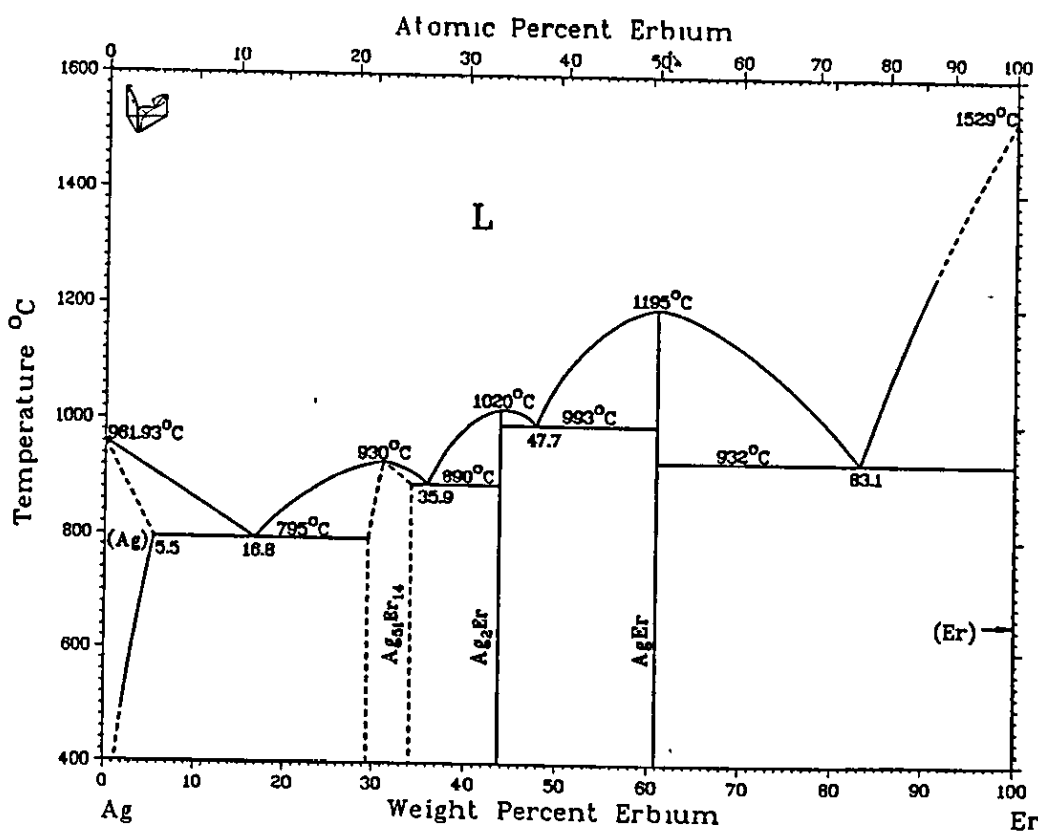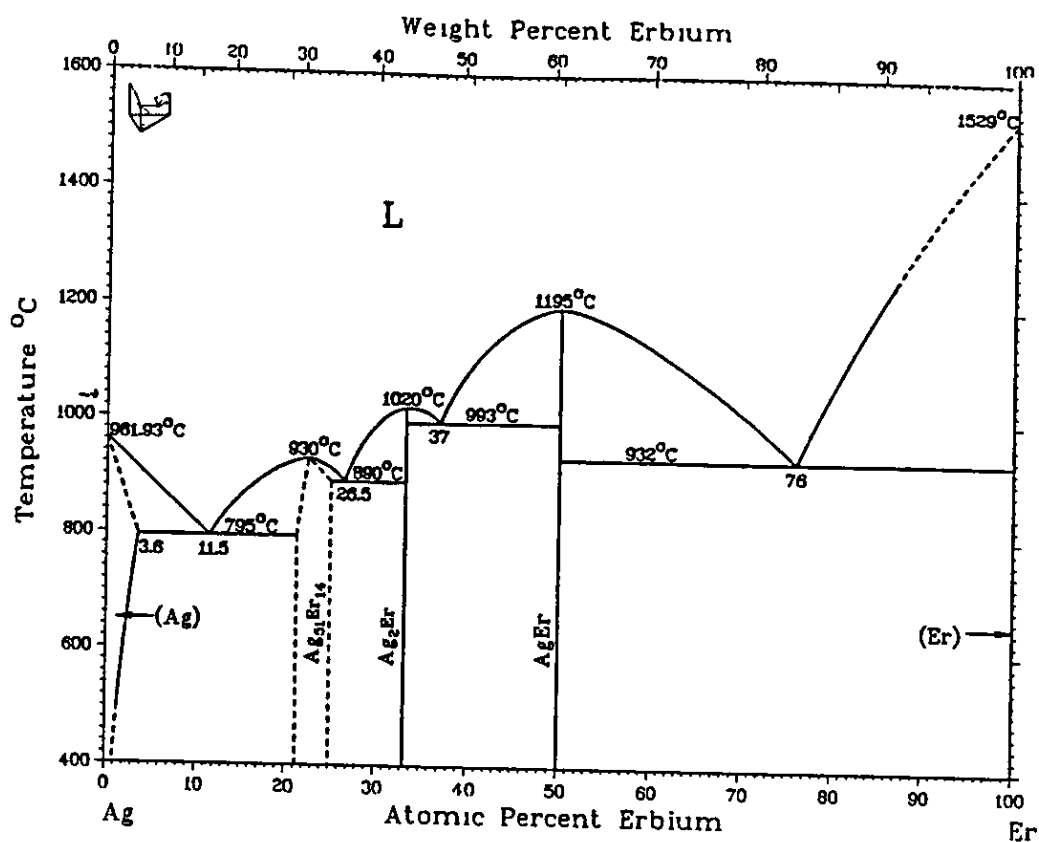
References

[1] McMaster O. D., Gschneidner K. A. (Jr.) and Venteiceher R. F., *Acta Crystallographica*, (1970), **B 26**, pp.1224-1229

[2] McMaster O. D , Gschneidner K. A. (Jr.), Bruzzone G. and Palenzona A , *Journal of the Less-Common Metals*, (1971), **25**, pp.135-160

[3] Bailey D. M. and Kline G. R., *Acta Crystallographica*, 1971, **B27**, pp.650-653

[4] Villars P. & Calvert L. D., Pearson's Handbook of Crystallographic Data for Intermetallic Phases, *American Society for Metals* (1986), ISBN 0-87170-217-7

[5] Steeb S., Godel D. and Löhr C., *Journal of the Less-Common Metals*, 1968, **15**, pp.137-141

[6] Kiessler G , Gebhardt E. and Steeb S., *Journal of the Less-common Metals*, 1972, **26**, pp 293-298

[7] Rodriguez-Caravjal J., Short references guide of the program FullProf (version 3.5 Dez. 97-LIB-GR) (1997)

[8] Brown P. J., Crangle J., Neumann K -U., Smith J. G. and Ziebeck K. R. A., *Journal of Physics: Condensed Matter*, 1997, **9**, pp 4729-4742

[9] Neumann K.-U., Crangle J., Zayer N K., Ziebeck K R.A, "The Analysis of Magnetic Behaviour with the Help of Arrott Plots", *Proceedings of the Eighth International Summer School of Condensed Matter Physics*, Bialowieza, Poland (1994)

[10] MPMS Software System Reference Manual, *Quantum Design* (1990)

W. Nolting

QuantenTheorie des Magnetismus, Teil 2 Modelle

B. G. Teubner Stuttgard (1986) ISBN 3-519-03085-3

Carl Nording and Jonny Ostermann

Physics Hangbook

ChartwelBratt Ltd. (1982), ISBN 0-86238-037-5

Mark J. Parson

An Investigation of the Thermal Properties of some Strongly Correlated Electron
Systems

PhD. Thesis, Loughborough University (1998)

Jacqui G. Smith

The Magnetic Structure and Magnetisation Distribution of the Intermetallic
Compound $U_{14}Au_{51}$

PhD. Thesis, Loughborough University (1997)

B. E. Warren

X-ray Diffraction

Diver Publications (1990), ISBN 0-486-66317-5

Kevin C. Watson

Investigation of the Magnetic and Lattice Properties of REPtIn and RE_2AgIn

PhD. Thesis, Loughborough University (1998)

Ch. Weißmantel and C. Hamann

Grundlagen der Festkorperphysik

Springer-Verlag Berlin Heidelberg New York (1980), ISBN 3-540-09072-X

Acknowledgements

My kind regards to all members of the Physics Department for providing such a pleasant working environment. In particular, I wish to thank Maureen McKenzie, who is the lovely helping angel of the Department.

A particular word of thanks is specially reserved for all the really good friends who made my time in Loughborough so enjoyable. Thanks to Petra Maier, Simone Clayhills, Corina Rieck, Isla Mathession, Daniel Neumann, Thomas C. Kiederich, Dirk Meyer, Betty and Peter Sharman, Alison and John Walker, Janie and Walter Cook, Monique Peron, Joanne and Ian Craig, Anne and Martin Faulks, Alasdair Rodgers, Chris York, Gery Rigby and all the friendly members of the Emmanuel Church at Loughborough. I had a marvellous time which will always be remembered with affection.